



UNIVERSIDAD DE CHILE
FACULTAD DE CIENCIAS FÍSICAS Y MATEMÁTICAS
DEPARTAMENTO DE ASTRONOMÍA

EXPERIMENTAL AND THEORETICAL CHALLENGES IN THE SEARCH FOR
TENSOR B-MODES

TESIS PARA OPTAR AL GRADO DE DOCTORADO EN CIENCIAS, MENCIÓN
ASTRONOMÍA

SRINIVASAN RAGHUNATHAN

PROFESOR GUÍA:
LUIS CAMPUSANO BROWN
PROFESOR GUÍA2:
GONZALO PALMA QUILODRAN
PROFESOR CO-GUÍA:
SUZANNE STAGGS

MIEMBROS DE LA COMISIÓN:
DENIS BARKATS
MARIO HAMUY WACKENHUT

SANTIAGO DE CHILE
2016

RESUMEN DE LA MEMORIA PARA OPTAR
AL TÍTULO DE DOCTORADO EN CIENCIAS, MENCIÓN ASTRONOMÍA
POR: SRINIVASAN RAGHUNATHAN
FECHA: 2016
PROF. GUÍA: LUIS CAMPUSANO BROWN, GONZALO PALMA QUILODRAN, Y SUZANNE STAGGS

EXPERIMENTAL AND THEORETICAL CHALLENGES IN THE SEARCH FOR
TENSOR B-MODES

Esta tesis describe el trabajo que he realizado para analizar los datos del experimento *Atacama B-mode Search* (ABS). Utilizando el telescopio de ABS, cuyos detectores son sensibles a la polarización, durante un período de tres años se observa la radiación en microondas del fondo cósmico (CMB). El telescopio está instalado en el desierto de Atacama, en el norte de Chile, a una altura de 5190 metros. El objetivo del experimento es detectar las ondas gravitacionales primordiales supuestamente generadas durante la fase inicial de expansión exponencial del universo. Estas ondas gravitacionales dejan registros únicas en polarización del CMB llamados *tensor B-modes*. Durante la última década se han realizado varios instrumentos para observar tensor B-modes, pero no se han detectado aún. Si se les detecta, serían una evidencia directa de un proceso llamado *inflación cósmica* que será el período inicial de la expansión exponencial. La detección también proporcionará pistas sobre la física de la inflación como la caracterización de tensor B-modes *vía* el cuociente tensor-a-escalar llamado r , está directamente relacionada con la escala de energía de la inflación $\mathcal{O}(10^{16})$ GeV, comparable a la gran unificación teoría (GUT) escalas de energía.

El experimento ABS fue diseñado y dirigido por el departamento de Física de la Universidad de Princeton. El ABS observó la CMB en la frecuencia de 145 GHz utilizando bolómetros sensibles a la polarización del tipo *transition-edge-sensor* (TES). Posee dos espejos, de 60 cms cada uno y dispuestos en una configuración del tipo *compact crossed-Dragone*. El ABS fue el primer experimento de medición de la CMB, situado en la Tierra, en implementar exitosamente la modulación de polarización rápida mediante una placa de media-onda *half-wave-plate* (*HWP*) mantenida a temperatura ambiente y girando continuamente.

En este reporte, presento la estrategia de observación, adquisición de datos, la calibración del instrumento, y las técnicas de selección de datos utilizados para producir los mapas de la CMB y estimación del Espectro de potencia de la CMB. Por completitud, también describo brevemente el trabajo realizado por otros miembros del proyecto ABS, pero menciono claramente mi contribución al comienzo de cada capítulo. El espectro de potencia final no se ha incluído debido a que tanto las técnicas de selección de datos y el modelado de la absorción debida a nuestra galaxia no están aún finalizadas. Sin embargo, los resultados de la evaluación estadística detallada de los datos utilizando un conjunto exhaustivo de pruebas de sesgo nulo (null tests) indican que nuestras medidas no están afectadas significativamente por efectos sistemáticos. La evaluación de las pruebas de sesgo nulo de las observaciones llevadas a cabo con el telescopio ABS nulos, es el principal resultado de este trabajo. Este resultado posibilita una determinación robusta del Espectro de Potencia de la CMB.

Abstract

This thesis describes the work that I performed to analyse the data from the Atacama B-mode Search (ABS) experiment. The ABS experiment observed the Cosmic Microwave Background (CMB) radiation for three years using polarisation sensitive detectors. The telescope is located at the Atacama desert in the north of Chile at an altitude of 5190 metres. The goal of the experiment is to detect the primordial gravitational waves which were supposed to have been generated during the initial phase of exponential expansion of the universe. These gravitational waves leave unique signatures on the polarised CMB called the *tensor B-modes*. Several experiments have been built over the last decade to observe them but the primordial tensor B-modes still remain undetected. If found, they will be a direct evidence for a process called *Cosmic inflation* which is responsible for the initial period of exponential expansion. The detection will also provide hints about the physics of inflation as the characterisation of tensor B-modes *via* the parameter called *tensor-to-scalar ratio r* is directly related to the energy scale of inflation $\mathcal{O}(10^{16})$ GeV, comparable to the grand-unification-theory (GUT) energy scales.

The ABS experiment was designed and led by the Physics department at Princeton University. The ABS observed the CMB at 145 GHz using polarisation sensitive transition-edge-sensor (TES) bolometers. There are two mirrors, 60 cms each arranged in a compact crossed-Dragone configuration. The ABS was the first ground-based CMB experiment to successfully implement the rapid polarisation modulation using a continuously rotating (warm) half-wave-plate (HWP).

In this article, I present the observation strategy, data acquisition, instrument calibration, and the data selection techniques used to produce the CMB maps and power spectrum estimation. For completeness, I also briefly describe the work done by other members of the ABS project but clearly mention my contribution at the start of every chapter. The final power spectrum is not shown as the data selection techniques and the modelling of the galactic foregrounds are still being finalised. However, the results from detailed statistical assessment of the data using an exhaustive suite of null tests indicate that we are not affected by any significant systematic effects. The assessment of the ABS null tests will be the major result of this work. This result enables a robust estimation of the power spectrum and the *tensor-to-scalar ratio*.

Work dedicated to Appa, Amma, and Aruna

*Work dedicated to
Prof. Albert Einstein, and Prof. Leonard Susskind
for their eternal motivation*

Agradecimientos

This work would not have been possible without the help of several people and I'm grateful to the people listed below:

- Suzanne Staggs is one of the most important people to have helped me to finish this thesis. She gave me the liberty to work on any aspect of data analysis but ensured that I'm going in the right direction.
- I practically learnt all of the CMB science from Gonzalo Palma. He convinced me about how interesting it is to study about the polarisation of the CMB and persuaded me to work on ABS.
- Prof. Luis Campusano has been extremely supportive and provided crucial comments. He also provided opportunity to guide undergraduate students in several research projects, and it was all a great experience.
- Akito Kusaka is one of the crucial members of the ABS team, and jointly led the data analysis along with Suzanne. He helped me in several stages of the data analysis and I also learnt proper computing form him. He is one of the nicest and wisest persons I have ever met.
- I had several useful chats with Denis Barkats that helped me to understand the big picture of the B-mode polarisation experiments.
- Prof. Mario Hamuy, also part of my thesis committee, provided useful comments during every thesis meeting from which I benefitted greatly.
- The ABS team members *viz.* Glen Nixon, John Appel, Jonathan Sievers, Katrina Visnjic, Kevin Crowley, Lucas Parker, Lyman Page, Patty Ho, Sara Simon, Steve Choi, Tom Essinger-Hileman were all very helpful and it was wonderful working with them.
- Prof. Paulina Lira was an outstanding postgraduate coordinator, and my PhD tenure in Chile would not have been possible without her help.
- Dr. Roger Clowes, my MSc advisor, taught me the ways of doing good research and I'm grateful to him.
- I thank the other staff personnels *viz.* Hernan Pulgar, Marta Ojeda, and Patricia Monroy at Calan, Carmen Belmar at DFI, Angela Lewis at Princeton. Thanks to Felipe Rojas, Patricio Gallardo, Masao Uehara, Maria Jose Amaral, and other Astronorte staff at San Pedro for helping with ABS observations.
- I thank Rolando Dünner, and Kam Arnold for extremely helpful discussions.
- I thank my friends Elise Servajean, Daniela Orquera, Paula Lopez, Paula Sanchez, Jose, Maritza, Fransisco, Fefi, Ganesh Babu, Sadish, Claudia for their motivation and

support.

- The other research students at Calan have been wonderful in maintaining a joyous work environment at Calan.
- The interactions with members of Anillo de cosmología was crucial in connecting CMB physics with the large-scale structures of the universe.
- I thank Mr. Tulsidas Mohinani who funded my first travel to Chile, and has been my well wisher always.
- I thank Suzanne, Jason, and their kids for allowing me stay at their home every time I visited Princeton.
- Many of my visits to Princeton, LBNL, and other important meetings would not have been possible without the financial support of Anillo de cosmología, CATA, CONICYT, and Sochias.

I'm indebted to my parents, sister, and her family for their eternal love, support, and guidance. This work is dedicated to them.

Tabla de Contenido

Tabla de Contenido	viii
Índice de Tablas	xi
Índice de Ilustraciones	xiii
1. INTRODUCTION	1
1.1. Our universe in a nutshell	1
1.2. The Microwave background	4
1.3. Cosmic Inflation	6
1.3.1. The theory of accelerated expansion	8
1.3.2. Parameterisation, and models of Inflation	10
1.4. Perturbations, and the Inflation observables	10
1.5. Polarised CMB	12
1.5.1. Perturbations, and the polarisation patterns	14
1.6. Challenges and current status of CMB experiments	16
2. THE ATACAMA B-MODE SEARCH	19
2.1. The Instrument	19
2.2. The site	21
2.3. Observations	26
2.3.1. ABS scan fields	28
2.3.2. Observing strategy and CMB observations	28
2.3.3. Point source observations	29
2.4. Data Acquisition and storage	30
2.5. HWP modulation and demodulation	32
3. CALIBRATING ABS TELESCOPE	36
3.1. Telescope pointing	36
3.1.1. ABS boresight pointing - Method	37
3.1.2. Pointing model v0 and v1	39
3.1.3. Pointing model v2 - The Euler rotation pointing model	39
3.1.4. RCW38 observations and ABS pointing in the west	42
3.2. ABS focal-plane pointing	44
3.2.1. Method	44
3.2.2. Wide Moon scans	47
3.2.3. Mapping, and detector pointing	47

3.3.	Beam characterisation	49
3.3.1.	Beam window function	49
3.3.2.	Beam profiles	51
3.4.	Crab Nebula observations and maps	53
3.4.1.	Absolute polarisation angle	53
3.4.2.	Accurate real-time pointing for <code>bolivar</code> and tight TauA scans	55
3.5.	Other calibrations	57
3.5.1.	Jupiter temperature and detector responsivities	57
3.5.2.	Polarisation angle of detectors	60
3.5.3.	Detector bandpass, and time constants	61
4.	DATA PROCESSING AND CUTS	62
4.1.	Data corrections	62
4.1.1.	Data selection	64
4.2.	Encoder slips	66
4.2.1.	Details about the unknown encoder slips	66
4.2.2.	Other events	66
4.2.3.	Faulty GPS	68
4.3.	“Ghost” images of bright sources	73
4.4.	Correlated noise	76
4.4.1.	Decomposition technique and mode finding	76
4.4.2.	Affected CES data sets	79
4.4.3.	Bad TES detectors that escaped data cuts	82
4.5.	Far-side lobe study	83
5.	CMB MAP MAKING	86
5.1.	CMB maps	86
5.2.	Masking point sources	88
5.2.1.	External point source catalogues	88
5.2.2.	PicA galaxy	90
5.2.3.	Apodization algorithm, and the source mask	91
6.	RESULTS	94
6.1.	Power spectrum using Pseudo- C_ℓ estimator	94
6.2.	Validation of the power spectrum	96
6.2.1.	Null test fundamentals	96
6.2.2.	ABS null suite	98
6.2.3.	Correlations between data points	103
6.2.4.	Null test results	105
6.3.	Current status of ABS	109
Bibliografía		111
A. Saran wrap to prevent dust over the HWP		117
B. Correlated noise detection		120
B.1.	Mode removal	120
B.2.	Automatic detection algorithm	120

B.3. Source of the noise	123
------------------------------------	-----

Índice de Tablas

2.1. Atacama B-mode Search - Information about the telescope location, and observation seasons.	23
2.2. Detail about the observation fields of the ABS experiment. The columns correspond to field name; field centre (RA, Dec.) in degrees; field widths in degrees; coverage area in square degrees; total observation hours; remarks about the field.	28
3.1. Different mapping algorithms for ABS point source observations. The instrument coordinates refer to $(\phi_{tel} - \phi_{obj}) \cos(\theta_{tel})$, $\theta_{tel} - \theta_{obj}$, ML refers to Maximum-Likelihood approach and was adopted to map faint sources namely RCW38, and Venus. The maps M1, M3, and M4 are simple projections of the TOD onto the map space using flat sky approximation.	37
3.2. ABS six parameter pointing model derived using Moon, Jupiter, and Venus observations from the first, and second seasons as shown in FIG. 3.1.	39
3.3. Euler pointing model v2 derived using Moon, Jupiter, and Venus observations.	40
4.1. A timeline of ABS azimuth encoder slips, and faulty GPS issues during the three seasons of observations. The title of the columns give the obvious description about the columns. The entires in red colour correspond to the smaller shifts which are guessed from the pointing model. For these observations, the analysis pipeline will be run twice with, and without introducing the shifts.	72
5.1. The brightness of PicA galaxy measured at different frequencies by different experiments. The numbers in red correspond to the extrapolated values from the previous frequency on the table (i.e:) QUIET-Q's extrapolated value is using AT20G, QUIET-W from QUIET-Q, and ABS from QUIET-W. The subscripts Q, U, P correspond to Stokes parameters, and the polarisation intensity $\sqrt{Q^2 + U^2}$. The extrapolation was done using $\beta = 0.85$ and matches very well to the actual observed value. The PicA galaxy is not seen by ABS as its temperature level at 145 GHz $\sim 1\mu\text{K}$ is comparable to the rms of our maps.	92
5.2. The antenna T_A , and thermodynamic T_{thermo} temperatures of PicA for QUIET, and ABS calculated using EQ. 5.11, 5.12. Red colour for ABS indicates that the flux value used for calculation is the extrapolated value using $\beta = 0.85$ from QUIET-W band.	92
6.1. The systematic biases probed by the 21 null tests in the ABS null test suite.	96

Índice de Ilustraciones

1.1.	A graphical representation of the overview of the tensor B-mode experiments. The currently active and future experiments based in Chile are mentioned. The ABS experiment, the major player in this thesis, is highlighted in red.	2
1.2.	A highly precise measurement of the CMB temperature anisotropies by the Planck satellite. The level of the anisotropies are extremely small $\Delta T/T \sim 10^{-5}$. The data from various frequency channels of the Planck satellite have been combined to remove the galactic foreground emission. Image obtained from ESA archives.	5
1.3.	CMB angular power spectrum measured by the experiments COBE, Toco, BOOMERanG, MAXIMA, WMAP, SPT, ACT, and Planck experiments. The colour scale (not linear) represents the data release year starting from COBE (1996) to Planck (2015). The error bars in the Planck data also include the <i>cosmic variance</i> and I have removed them for clarity. No best fit Λ CDM curve is fit to the power spectrum as it is quite easy to guess just form the data points. The curve generated using the tool Code for Anisotropies in the Microwave Background (CAMB) [11] for Λ CDM is shown as black curve along with data points from ACT, Planck, and SPT are shown in the inset plot for reference. The mismatch between the Λ CDM curve and the data points at small scales (higher multipoles) arise due to the power from secondary anisotropies <i>viz.</i> SZ effect, dwarf galaxies.	7
1.4.	A toy model of SFSR inflation showing the slow roll of the scalar field ϕ down the potential well. The kinetic energy of the field is low compared to the potential energy when ϕ is small maintaining an almost constant potential $V(\phi)$ and the universe expands exponentially during this period. The quantum fluctuations $\delta\phi$ forms the sees of the current structures in the universe. Image obtained from [14].	8
1.5.	Three different cases experienced by an electron at the surface of last scattering. The colours represent the temperature of the CMB photons - cold = blue; hot = red; average = green. The figure on the top left (right) shows that no net polarisation would be produced if the electron only sees monopole (dipole) component of the temperature anisotropy. The bottom figure shows the (partial) linear outgoing polarisation due to the quadrupole anisotropy of the surrounding photons during the period of recombination. The figures were generated based on the materials by Hu & White [22], and Dodelson [2]. . .	13

1.6. Temperature, E, and B-mode polarisation power spectrum. Black and red solid curves represent the temperature, and gravitational weak lensing power spectrum. The scalar E-mode spectrum is shown in blue. The green curves show the tensor B-mode power for different tensor to scalar ratios $r=0.2$ (dashed), $r=0.05$ (solid), and $r=0.01$ (dotted). All the curves are generated using the CAMB tool [11] for the standard Planck Λ CDM model. The data points from BICEP2 [26], and POLARBEAR [25] for the reported measurements of primordial, and lensing B-modes are shown as magenta and cyan points. The white band is the multipole range $40 \leq \ell \leq 400$ is the region to which the ABS telescope is highly sensitive. The errors due to sample variance and the instrumental noise (yellow band) was calculated as described in the text are also shown for $r = 0.05$	17
2.1. A schematic diagram showing the observation of the CMB sky using ABS. The CMB photon goes through the telescope <i>baffle</i> which blocks other undesired signals; crosses the <i>HWP</i> (the first optical element of ABS) and will be modulated; hits the <i>two mirrors</i> and captured by the detectors on the <i>focal-plane</i> . The <i>TES detectors</i> are placed behind the <i>corrugated feed-horns</i> which are planted onto the ABS <i>focal-plane</i> . The <i>ground screen</i> was installed after a month of the telescope deployment to prevent signals from far side-lobe of the telescope.	20
2.2. The left panel shows the ABS receiver demonstrating all the key components of the telescope <i>viz.</i> baffle, focal-plane, Helium fridge, HWP, mirrors, and the pulse tube cooler. Figure courtesy of Thomas Essinger-Hileman. The right panel shows the ABS telescope observing at Cerro Toco. The receiver in the left panel can be seen in white colour inside the giant blue ground screen. The telescope was mounted on top of a shipping container.	22
2.3. The atmospheric transmission at the ABS observing frequencies calculated using the APEX telescope atmosphere model [38] for different PWV levels at an elevation of 5100 metres at the <i>Llano de Chajnantor</i> in Chile.	24
2.4. The values of the NET_{ABS} of the ABS detectors during the first, and second season of observations. The top panel shows the values for each observation day with the colour scale representing the average PWV level on the respective day. The observation day number ranges between 13 September, 2012 to 21 December, 2013. The bottom panel shows the NET_{ABS} as a function of the PWV level (bin-width = 0.05 mm). The black curve is a quadratic fit to the square of NET to account for the shot noise, and Dicke noise terms. The error bars in both panels correspond to the standard deviation in the particular bin.	25
2.5. ABS observation fields (white) along with other CMB experiments (ACTpol, BICEP2, QUIET, POLARBEAR, SPIDER, and SPTpol) overlaid on the polarisation intensity map produced by the Planck HFI (143 GHz) instrument. The inset plot shows the weight map for ABS field-A. See table 2.3.1 and text for more details.	27
2.6. The number of targeted point source observations on detectors from different detector columns on the ABS focal-plane. The reference column <i>c23rxx</i> contains more targeted observations as compared to others.	30

2.7. The original (top left), and the demodulated streams (bottom left) along with their power spectrum in the right panels. The black, green, and magenta lines correspond to original timestream, and Q, U Stokes parameters. The 1/f noise is evident in the original timestream - note the $f_{k\text{nee}}$ around 2 Hz in the top right panel. The HWP demodulation eliminates much of the unpolarised atmospheric signal and shifts the $f_{k\text{nee}}$ towards lower frequencies for the demodulated timestreams (bottom right panel). Also present in the power spectrum are the bump near the scan frequency $f_{\text{scan}} = 0.04$ Hz, and near the HWP 1f, 2f = 2.55, and 5.1 Hz. The demodulated timestreams are low-pass filtered with $f_{\text{cut-off}} = 2$ Hz.	35
3.1. ABS original encoder offsets showing the systematics errors. Top panel shows the elevation encoder offsets $\Delta\theta$ as a function of azimuth (left) and elevation(right). Bottom panel shows the how the azimuth encoder offsets $\Delta\phi \cos(\theta)$ are affected at different azimuth (left) and elevation (right) positions. Circles are Moon, stars are Jupiter, and diamonds are Venus observations respectively. The spectral colours on the plot serve as a proxy for the observation date (although not in a linear scale) with red being the most recent observation.	38
3.2. Stacked RCW38 maps observed in the azimuth west during the second observation season. The three panels correspond to the stacked maps before applying the pointing model (left panel), after applying pointing model v0 (middle panel), and the Euler rotation pointing model v2 (right panel). The pointing models does not correct the $\sim 0.13^\circ$ azimuth shift.	43
3.3. The final pointing residuals after performing the pointing offsets modelling using Euler rotations v2. The top, and bottom panels correspond to the azimuthal, and elevation residuals respectively.	45
3.4. Moon maps from various detectors on the ABS focal-plane using a single wide Moon observation performed on August 1, 2012. The maps were originally made in equatorial coordinates using HEALPix Pixelization, and then shifted by 3x the detector positions for visualising the maps of on detectors on a single image. The scan centre ($\alpha, \delta = 308.1, -9.5$) degrees is marked with white plus symbol for reference.	46
3.5. The offsets $\Delta\phi\cos(\theta)$ (left), and $\Delta\theta$ (right) in degrees for all the detectors on the ABS focal-plane for the Moon observation on 1 August, 2012. The coverage was exceptional and the gaps in the plot are because of the dark (or) bad detectors. The reference detector c23r00 near the centre of the focal-plane is marked with a black outline. An extremely small gradient can be seen in the $\Delta\phi\cos(\theta)$ offsets in the left panel. We decided to ignore the gradients after verifying the gradient levels of several observations. The gradients does not correspond to systematic effects due to the motion of Moon during the scan, and detector response time.	48

3.6. The distribution of the residuals $\Delta\phi\cos(\theta)$ (left), and $\Delta\theta$ (right) of every wide Moon observation used for the focal-plane pointing modelling. The residuals correspond to the values after six iterations where every iteration corresponds to 1. deriving the shifts in the detector positions using the offsets from the previous iteration; 2. map making with this shifts added; 3. deriving the new offsets for each detector from every observations; 4. use the average value of the offset for each detector from seven different observations.	49
3.7. The distribution of the final residuals $\Delta\phi\cos(\theta)$ (top), and $\Delta\theta$ (bottom) after six iterations of the focal-plane pointing procedure described in the text. The rms value of the offsets are also mentioned in each panel. The data points were obtained using seven wide Moon observations from the first season.	50
3.8. ABS beam window functions calculated using EQ. 3.23, 3.25. Three curves are shown. The black curve correspond to current ABS beam window function based on a sophisticated beam modelling along with the pointing residuals by Glen Nixon. The red, and green curves assume Gaussian beam EQ. 3.25 and correspond to ABS main beam, and mean beam with the pointing residuals included. The inset plot is the multipole region around the multipoles where the peak of the B-mode power spectrum is expected. The curves have been normalised using the power at $\ell = 55$ corresponding to the first power spectral bin for ABS.	52
3.9. Sample Jupiter observations from season 1 data targeted on pod 23. Plot titles show the date and time (YYYYMMDD_HHMM) of observation given in UTC format. Colour bars represent the Jupiter power in aW.	54
3.10. Stacked Jupiter scans captured using detectors on c23rxx during the first season. The left panel shows the staked map, and right panel shows the radial profile of the stacked map. The green solid line correspond to the Gaussian main-beam with $\sigma_{\text{ABS}} = 32.4 \pm 1$ arcmins.	54
3.11. Stacked polarisation intensity map of several TauA observations using detectors close to the telescope boresight. The observed mean polarisation angle is $\gamma = 150 \pm 1.7$ degrees. Figure courtesy of Thomas Essinger-Hileman.	55
3.12. A test tight TauA type scan of field-B1 scan on 23 April, 2014 using the edge detector c03r18. Red star indicates the desired point to be scanned which has been missed by the scan (green) because of the flat sky approximation used by bolivar . The original boresight location is shown in black. The <i>bore-sight ->detector ->bore-sight</i> reconstruction using the exact pointing equations correctly places the reconstructed yellow region over the original black region.	56
3.13. The hit map of two test tight TauA scans using two edge detectors. The exact Euler pointing calculation was used by bolivar for these scans. The coverage looks good. The colour scale represents the number of time samples with a sampling frequency of 200 Hz. The total time span of test scan was ~ 5 minutes.	57
3.14. Responsivities of individual detectors in ABS using Jupiter observations from season 1 data. The horizontal axis of the plot show the day number starting from 28 th February, 2012 when ABS saw the first light.	59

- 4.1. The contribution of each TES detector to the final map making stage based on the data selection techniques described in section 4.1.1 for all the ABS scan fields. Note that the data selection techniques were only based on the CMB field-A, and the other fields are just shown for the entirety. The colour bar represents the total observation hours based on the passed CESes. 67
- 4.2. The azimuth offsets of point source observations as a function of the observation date during the first two seasons. Stars, and circles correspond to Jupiter, and Moon observations. The colour of the data points represent the distance of the detector that captured the source from the boresight (blue = near; red = far). The yellow bands correspond to dates when no observations were made due to weather (or) instrument related issues. The red, and blue vertical lines enclose the season 1, and 2 respectively. The dashed magenta lines show the date of the azimuth encoder slips. The magnitude, and the direction of all the shifts are marked. The three stars at the bottom enclosed by black circle of the plot correspond to Jupiter observations made during the faulty GPS period. The data points in the far right in the top panel correspond to observations in September 2013, where there is an additional 0.1° shift. These were handled by two different version of the pointing model as mentioned in the text and the result is shown in the bottom panel. 69
- 4.3. Similar to FIG. 4.2 but the vertical axis correspond to elevation offsets during the first two observation seasons. The increase in the elevation offset ($\sim 0.1^\circ$) during the second season is evident here. I emphasise that the colour of the data points in this plot only correspond to observation date (same as the horizontal axis) unlike the detector location on the focal-plane in FIG. 4.2, and not to be considered. 70
- 4.4. Maps in boresight coordinates of two Jupiter observations 20131011_1115 (left), and 20131012_1119 (right) with different mapping algorithms M2 (top), and M4 (bottom). Both the mapping algorithms return significant pointing offsets. The large pointing offsets are because of the issue with the ABS GPS. 71
- 4.5. Detector offsets in degrees in the azimuthal ($\delta\phi \cos(\theta)$), and elevation ($\delta\theta$) shown in the left, and right panels for a wide Moon observation performed on 12 October, 2013. The offsets show a systematic error (gradient across the focal-plane) due to the faulty GPS. 72
- 4.6. The ghost image of Moon enclosed by the white dashed circle from a wide Moon scan performed on July 28, 2012. The colour scale has been normalised to unity to show that the amplitude of the ghost is ≤ 5 per cent of that of the Moon. The map is shown in equatorial coordinates. 73
- 4.7. The location of the ghost images on the ABS focal-plane for selected detector columns (1,2,4,6,23) from a single wide Moon observation. The circles show the location of the detector α, β , and the bigger squares show the location of the ghost of the same columns (but at $-x\alpha, -y\beta$) which are reflections of the Moon from different detector columns. The exact value of x, y will depend on the region of the sky scanned, and the motion of the Moon during the observation time. It is clear from the plot that the ghost images are reflections of the source by the (rim of the) feed-horns. The colours just show different columns that are plotted. 74

4.8. The ratio of the amplitude of ghost image to the Moon using three wide Moon observations from the first season. Only the detectors shown in the plot have a satisfactory Gaussian fits. The amplitudes of the ghost images are extremely low and does not exceed more than three per cent of the amplitude of the Moon. No ghost images were seen in the CMB scans, and other point source observations.	75
4.9. Correlation matrices of the Q , and U Stokes parameters for the 2082.0 (left), and 2176.2 (right) CESes from the first season of CMB field-A observations. The correlation matrix of CES 2086.0 (left) looks normal while the 2176.2 (right) reveals the presence of a strong correlated noise component.	77
4.10. Q , and U eigenvectors of the first two dominant modes for the 2082.0 (left), and 2176.2 (right) CESes obtained using the SVD.	78
4.11. The first six dominant modes for the 2082.0 (left), and 2176.2 (right) CESes calculated using EQ. 4.3. The units are aW . The TODs have been down sampled to 1 Hz, and the horizontal axis correspond to the data values at each second. The first few modes of both the CESes show the presence of structure of $1/f$ noise although only the 2176.2 CES contain the correlated noise component. See text for more details.	79
4.12. The distribution of f_{knee} of the detector TODs for the 30 affected CESes in the top panel, and the normal CESes in the bottom panel. Clearly, the bad detectors in the affected CES have a higher f_{knee}	80
4.13. Same as FIG. 4.12 but for all the CESes from the first season. The affected CESes were identified using the automatic detection algorithm described in Appendix B.	81
4.14. The number of CESes in which a particular detector behaves badly after all the data cuts. See EQ. 4.4 for more details.	82
4.15. The total observation time in minutes of the ABS scans in the Sun relative coordinate system. Only the CESes when the Sun was above the horizon have been used here.	84
4.16. The total observation time in minutes of the ABS scans from the each field individually in the Sun relative coordinate system. Only the CESes when the Sun was above the horizon have been used here.	85
5.1. The flux distribution of sources from Planck $P_{143}, P_{353}, P_{\text{GCC}}$, and WMAP point sources catalogues that lie on the ABS field-A. A flux threshold of 500 mJy has been applied. There are 208 sources in total.	89
5.2. The region (50 sq.deg) around PicA galaxy from ABS Q, U maps (in equatorial coordinates) in the top panel. The bottom panel shows the region (in galactic coordinates) from the Planck 143 GHz channel. The presence of PicA in the maps is not obvious. The temperature of PicA should be $\sim 1.2 \mu\text{K}$ (EQ. 5.11,5.12).	91
5.3. The ABS maps of Stokes parameters Q (left), U (right) is shown in the top panel in μK_{CMB} . The corresponding covariance (weights) QQ, UU are in the bottom panel. The maps have been convolved with the point source mask using the sources from Planck, and WMAP catalogues. A flux threshold of 500 mJy has been applied to select the sources. All the maps, originally in equatorial coordinates have been projected to cartesian basis.	93

6.1. The $C_{\ell_{\text{null}}}$ EE (green), and BB (red) spectra for six null tests based on the instrument performance (detector locations on the focal-plane, detector angles, batch A and B, squid polarity, and the white noise level) from the ABS null suite.	98
6.2. The absolute value of the correlation coefficient calculated using (Eq. 6.6) between different null tests in the ABS null suite. Only the off diagonal elements are shown for clarity. The correlation values are explicitly mentioned in the lower triangle of the matrix.	104
6.3. The distribution of $\chi^2_{\text{null,data}}$ values of the 13 power spectral bins from the ABS null suite are shown as the black histogram. The top panel shows the combined χ^2 values for EE, and BB power spectra. The bottom left (right) panel show the EE (BB) χ^2 values separately. The counts lie well between the (1σ , 2σ , and 3σ) errors obtained from MC simulations which are shown as different shades of orange around the black histogram. The inset plot shows the “uniform” distribution of the PTE values declaring the success of the null tests. The overall χ^2 , and PTE values are also listed for each panel and look normal.	106
6.4. Worst χ^2 values in each of the 80 simulations for all null tests in the first power spectral bin is shown as the black histogram. The green (red) vertical represents the χ^2 of the data in the same bin for the passed (failed) null tests.	108
6.5. Same as FIG. 6.3 but only for the first power spectral bin. Left panel is for EE, and right panel is for BB spectra.	108
6.6. Distribution of the χ_{null} of the data (red) and the MC simulations (black histogram) of the ABS null suite. We have used the cross correlation between different datasets while calculating the null spectra. The error bars correspond to the standard deviation of the data points in the respective bin. The data nicely follows the simulations and does not show any bias (with a zero mean) in our results. The mean $\chi_{\text{null}}^{\text{data}}$ value is mentioned in the figure.	109
A.1. Power spectrum of the detectors from randomly picked detectors with the wrap on (red) top of the baffle compared to the test without the wrap (green). The test was performed on wrap test performed on April 2, 2012. The data using the wrap seems to be bad. The tests were performed before the introduction of the ground scree. The data files used are mentioned on top of the plot and are labeled as F1 through F4.	118
A.2. Saran wrap test performed after the deployment of the ground screen. The left (right) shows the data taken when the wrap was at the top (bottom) of the baffle. No significant improvements can be seen between green (no wrap), and red (wrap) lines. But the usage of the wrap did not introduce additional noise unlike in FIG. A where the additional noise was likely due to the absence of ground shield. Also, no significant changes between the left and the right panel.	119
B.1. Distribution of knee frequencies before (red) and after (green) mode removal for the affected CES 2176.2. Top (bottom) panel shows the distribution of $f_{k_{\text{knee}}}$ of the Q (U) Stokes parameter. Dashed lines show the median $f_{k_{\text{knee}}}$	121

B.2. The median values (vertical axis) of the correlation coefficients for QQ (yellow), QU (green), and UU (cyan) after rotating the correlation matrix by various rotation angles (horizontal axis) of all detectors for 16 randomly picked CES. The black solid curve is the best fit sine curve. At a phase angle of $\sim 49.7^\circ$, the median values of QQ, QU tend towards zero for most of the CES. We picked the respective angle for CES and rotated the UU correlation matrix to use it for the automatic detection algorithm.	122
B.3. Correlation between the observing condition (from housekeeping data) and the width of the distribution of the correlation matrices. The red points are bad CES, and green are normal. No unique strong correlation can be seen between the affected CES (red points) and any of the housekeeping data.	124
B.4. Correlation between the observing condition (from housekeeping data) and the width of the distribution of the correlation matrices. The red points are bad CES, and green are normal. No unique strong correlation can be seen between the affected CES (red points) and any of the housekeeping data.	124

Capítulo 1

INTRODUCTION

Overview:

The Atacama B-mode Search (ABS) experiment located in the north of Chile is a dedicated experiment looking to detect the primordial gravitational waves (PGW) via their unique signatures – *tensor B-modes* – on the polarised Cosmic Microwave Background (CMB) radiation. The PGW were generated during the initial moments of the universe when the universe expanded exponentially by a process called *Cosmic inflation*. An overview of all the CMB B-mode experiments is shown as a flowchart in FIG. 1.1. A number of experiments have been aiming to observe the tensor B-modes and the flowchart lists the ones that are based in Chile (ACT, CLASS, QUIET, and POLARBEAR). Some other similar experiments include BICEP, KECK array, and SPT at the south-pole, and QUIJOTE at the Teide Observatory in Islas de Canarias, Spain.

The prime focus of my thesis work is the data analysis of the ABS experiment.

I start this chapter with a minimal review of the Λ CDM model followed by the cosmic microwave background (CMB), an example and parametrisation of inflation, polarisation of the CMB, tensor B-modes, and the status of current cosmological experiments.

1.1. Our universe in a nutshell

The Lambda Cold Dark Matter (Λ CDM) model is the prevailing standard cosmological model of our universe as it successfully describes several observational features of our universe. According to the Λ CDM model, our universe was created \sim 14 billion years ago from a singular event called the Big-Bang. The universe was extremely hot and dense initially during the Big-Bang after which it started expanding and subsequently cooled. To resolve some of the issues faced by the Big-Bang model (see section 1.3), a theory of exponential expansion of the universe during the initial moments was proposed. This is called *cosmic inflation* and it also provides the seeds for the structures that we see in the universe *via* tiny primordial fluctuations. It is beyond the scope of this work to explain the Λ CDM model in detail and

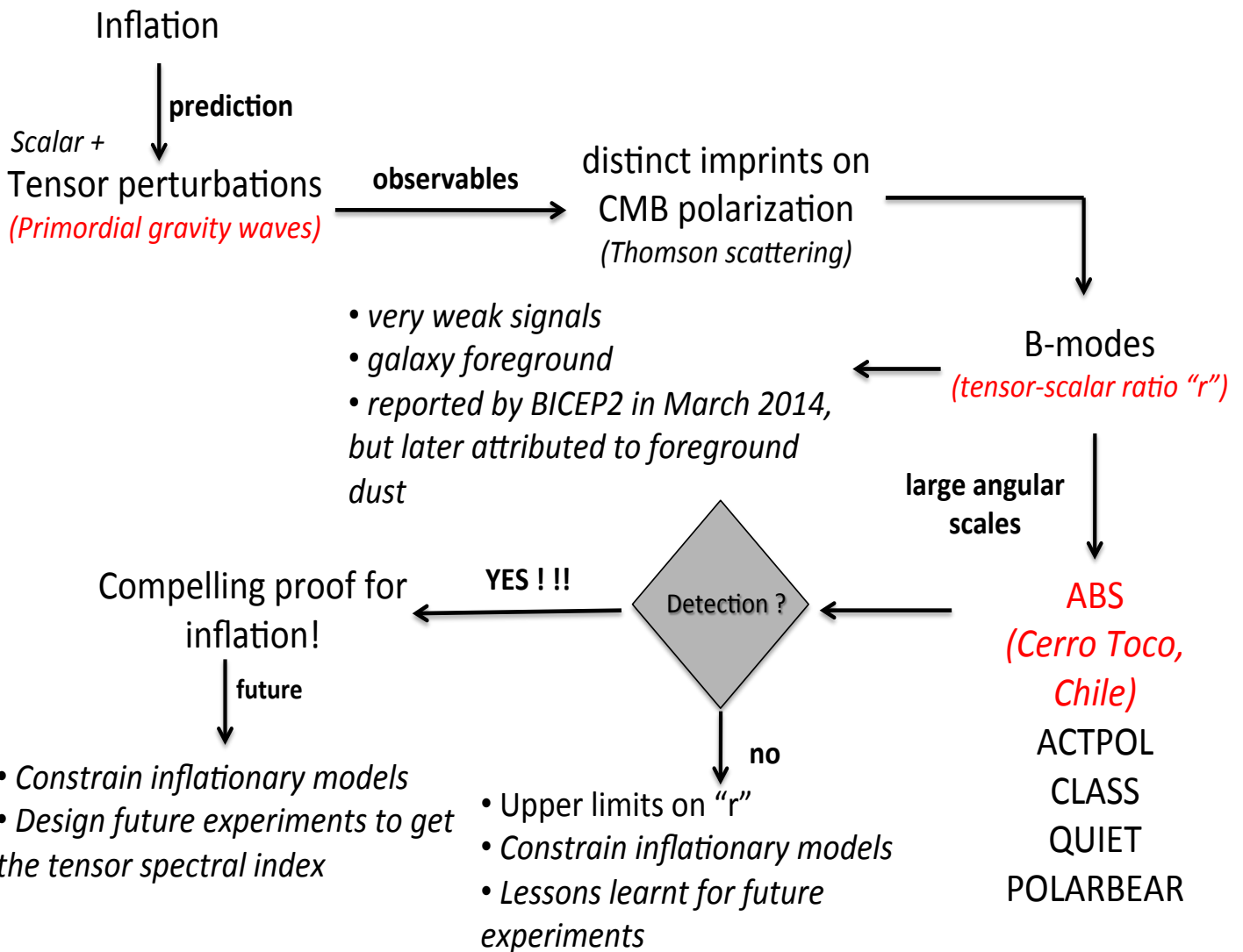


Figura 1.1: A graphical representation of the overview of the tensor B-mode experiments. The currently active and future experiments based in Chile are mentioned. The ABS experiment, the major player in this thesis, is highlighted in red.

I refer the reader to look into the standard books for cosmology [1, 2]. Here I give a brief summary of the Λ CDM model.

The equations of motion of a test particle in the Λ CDM universe are described by the Einstein's General Theory of relativity (GR)

$$G_{\mu\nu} \equiv R_{\mu\nu} - \frac{1}{2}g_{\mu\nu}R = \frac{8\pi GT_{\mu\nu}}{c^4} \quad (1.1)$$

where $G_{\mu\nu}$ is the Einstein tensor, $R_{\mu\nu}$ and R are Ricci tensor and scalar, $g_{\mu\nu}$ is the GR metric, G is the Newton's gravitation constant, $T_{\mu\nu}$ is the Energy-Momentum tensor, and c is the velocity of light. The metric $g_{\mu\nu}$ ¹ for an expanding flat universe is called the Friedmann-Lemaitre-Robertson-Walker (FLRW) metric and is defined as

$$g_{\mu\nu} = \begin{pmatrix} +1 & 0 & 0 & 0 \\ 0 & -a^2(t) & 0 & 0 \\ 0 & 0 & -a^2(t) & 0 \\ 0 & 0 & 0 & -a^2(t) \end{pmatrix} \quad (1.2)$$

where the *scale factor* $a(t)$ gives the relative expansion rate of universe. The evolution of the scale factor in an homogenous and isotropically² expanding universe is given by the Friedmann equation.

$$H(t)^2 = \left[\frac{\dot{a}(t)}{a(t)} \right]^2 = \frac{8\pi G\rho}{3c^2} - \frac{kc^2}{a^2(t)} \quad (1.3)$$

where $H(t)$ is called Hubble parameter which gives the expansion rate of the universe. The Hubble constant H_0 (Hubble parameter at the current epoch) is $H_0 = 67.8 \pm 0.9 \text{ km s}^{-1} \text{ Mpc}^{-1}$ [19]. The Hubble constant is frequently written as $100 * h \text{ km s}^{-1} \text{ Mpc}^{-1}$ and the parameter $h = 0.67$. From EQ. 1.3 we can define the critical density of the universe ρ_c which is the density required for the universe to be spatially flat with $k = 0$ (and the velocity of light c set to unity)

$$\rho_c = \frac{3H^2}{8\pi G} \quad (1.4)$$

and the observations suggest that we indeed live in a flat universe with the density equal to the current value of critical density $\mathcal{O}(10^{-27}) \text{ kg m}^{-3}$. It is customary to define the energy density of the universe with respect to the ρ_c as $\Omega = \rho/\rho_c$. We can also note that the expansion rate of the universe at a given time depends on the energy contents ($\rho = \rho_r + \rho_m + \rho_k + \rho_\Lambda$) of the universe at that time where the subscripts stand for radiation, matter (baryon and dark matter), curvature, and dark energy. Expressing the densities using Ω it follows that H is

$$H = H_0 \sqrt{\Omega_r a(t)^{-4} + (\Omega_c + \Omega_b)a(t)^{-3} + \Omega_\Lambda} \quad (1.5)$$

where Ω_c, Ω_b are the densities of the cold-dark matter, and baryons written separately and $\Omega_k = 0$. The inflationary Λ CDM model explains the universe based on just six free parameters *viz.* the energy densities of cold-dark matter $\Omega_c h^2$ and baryons $\Omega_b h^2$, the spectral index

¹The metric helps us to define the *proper time* $ds^2 = \sum g_{\mu\nu} dx^\mu dy^\nu$. In a 2d-Euclidean geometry this reduces to the distance between two points $ds^2 = dx^2 + dy^2$.

²The assumption that the universe is homogenous and isotropic on large-scales is called the *cosmological principle*.

n_s and the amplitude A_s of the primordial Gaussian random fluctuations, the optical depth at the time of reionisation τ , and the size of the sound horizon at the time of recombination θ^* . Refer to the results of Planck satellite [19] and the reference therein for the measured values of the parameters by various experiments.

1.2. The Microwave background

The Cosmic Microwave Background radiation commonly called the CMB is the remnant radiation from the Big-Bang. It is one of the most important observational evidence reinforcing the Big-Bang hypothesis, which asserts that the universe emerged from a singular event about 14 billion years ago. It was discovered by Arno Penzias, and Robert Wilson [3] at Bell Labs in Holmdel, New Jersey using a large horn antenna. The CMB is an extremely homogeneous and isotropic radiation filling the entire universe visible to us from $\sim 400,000$ years after the Big-bang. The universe was hot and highly ionised, consequently opaque before this period with the free electrons continuously scattering the CMB photons reducing their mean free path. It was only after 400,000 years that the universe started to cool down (because of expansion) enough to allow the free electrons to combine with protons forming neutral atoms. This period, commonly referred to as the epoch of recombination (or the surface of last scattering) marks the epoch when the CMB photons began to stream freely towards us as the universe started to become transparent.

Since its discovery, numerous experiments have been designed to study the universe using the CMB. One of the prominent breakthroughs came from the Cosmic Microwave Background Explorer (COBE) satellite in the early 1990's which first observed the CMB anisotropies with an angular resolution of $\sim 7^\circ$ using the Differential Microwave Radiometer (DMR) instrument [4]. The Far-Infrared Absolute Spectrophotometer (FIRAS) instrument on the COBE satellite showed that the CMB spectrum follows a perfect black body spectrum corresponding to a temperature of $T = 2.726\text{K}$. The advances in the field came rapidly after COBE. The first peak (recombination) on the angular power spectrum (see below) of the CMB was first measured in the late 1990's by the Mobile Anisotropy Telescope (MAT)³ experiment on Cerro Toco in the north of Chile [5]. The result was later confirmed by the balloon-borne BOOMERanG [7] and MAXIMA-1 [8] experiments.

The telescopes after the above pioneering experiments had high angular resolution to measure the CMB anisotropies to a great degree of accuracy. FIG. 1.2 shows a high resolution measurement of the CMB anisotropies measured by the Planck satellite. The data from various frequency channels have been combined to remove the galactic foreground emission. The figure was obtained from the ESA archives⁴. We now know that these temperature anisotropies are extremely small of order $\frac{\Delta T}{T} \sim 10^{-5}$.

The CMB angular power spectrum is the angular two-point correlation function and describes the variation in the temperature between two points on the sky as a function of their

³It is commonly known as Toco experiment.

⁴http://www.esa.int/Our_Activities/Space_Science/Planck/Planck_and_the_cosmic_microwave_background

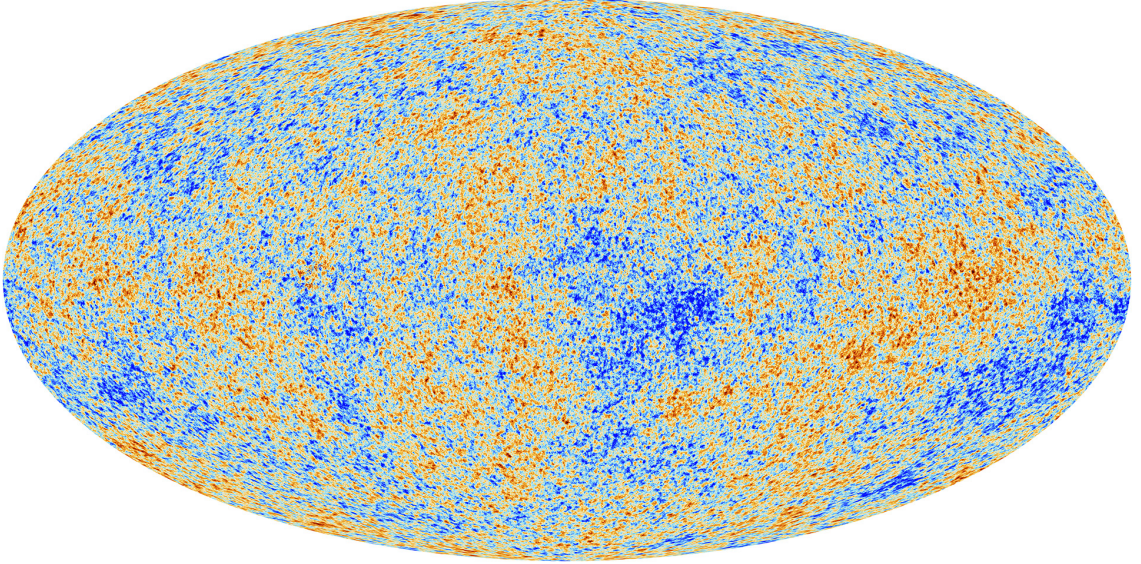


Figura 1.2: A highly precise measurement of the CMB temperature anisotropies by the Planck satellite. The level of the anisotropies are extremely small $\Delta T/T \sim 10^{-5}$. The data from various frequency channels of the Planck satellite have been combined to remove the galactic foreground emission. Image obtained from ESA archives.

angular separation on the sky. It is averaged over the multipole moments (or angular frequency) ℓ and are normally plotted as a function of ℓ . The power spectrum for a small region of the sky can be computed by taking the Fourier transform of the sky map. However, to compute the power spectrum from the map of the entire sky (on a sphere) like shown in FIG. 1.2, the Spherical Harmonic transformation (SHT) must be used as there is angular dependance. On a sphere, a function $f(\phi, \theta) = f(\hat{n})$ can be written in terms of SH as

$$f(\hat{n}) = \sum_{\ell,m} a_{\ell m} Y_{\ell m}(\hat{n}) \quad (1.6)$$

where $a_{\ell m}$ represent the coefficients of the SH $Y_{\ell m}$ for $\ell = 0, 1, 2, \dots$ and $-\ell \leq m \leq \ell$. The moments $\ell = 0, 1, 2$ represent monopole, dipole, quadrupole moments respectively. Thus the temperature field at direction $T(\phi, \theta) = T(\hat{n})$ is be defined as,

$$T(\hat{n}) = \sum_{\ell,m} a_{T,\ell m} Y_{\ell m}(\hat{n}) \quad (1.7)$$

The CMB power spectrum is normally represented as C_ℓ which is actually the variance of the $a_{\ell m}$. The mean value of $a_{\ell m} = 0$.

$$C_\ell \delta_{ll'} \delta_{mm'} = \langle a_{T,\ell m}^* a_{T,\ell m} \rangle \quad (1.8)$$

We noted above that for a given multipole, we average over $-\ell \leq m \leq \ell$ (i.e:) $2\ell + 1$ measurements and we sample C_ℓ as

$$C_\ell = \frac{1}{2\ell + 1} \sum_{m=-\ell}^{\ell} |a_{\ell m}|^2 \quad (1.9)$$

For the same reason, as ℓ decreases the uncertainty in the measurement of C_ℓ increases as we have lesser number of measurements. Assuming we have measurements at all multipoles ℓ (without binning), this uncertainty is given as

$$\Delta C_{\ell_{\text{cosmic}}} = C_\ell \sqrt{\frac{2}{(2\ell + 1)}} \quad (1.10)$$

This is called the *cosmic variance*. Later we will note for ground based experiments which have limited sky coverage, EQ. 1.10 will be modified as EQ. 1.11⁵ which is called *sample variance*

$$\Delta C_{\ell_{\text{sample}}} = C_\ell \sqrt{\frac{2}{(2\ell + 1) \Delta \ell f_{\text{sky}}}} \quad (1.11)$$

where $\Delta \ell$ is the bin-width and f_{sky} is the region of the sky observed (or unmasked). For ABS, the main CMB patch is ~ 2400 sq.deg. corresponding to $f_{\text{sky}}^{\text{ABS}} = \frac{2400}{4\pi} \times \left(\frac{\pi}{180}\right)^2 \sim 0.05$ ⁶. Thus, the satellite experiments which can cover the whole sky are limited by *cosmic variance* and the ground-based experiments with limited sky coverage are limited by *sample variance* in extracting information about very low multipoles. Low multipoles correspond to large angular scales on the sky $\ell \sim \frac{1}{\theta}$ and the recombination peak corresponds to $\sim 1^\circ$ on the sky appears around $\ell \sim 200$. At small angular scales the experiments are limited by their angular resolution.

Most of the above arguments hold good also for polarisation. The only difference is that the simple SHT is not valid for the polarisation field measured using Stokes parameters Q and U . As polarisation is a spin-2 field, a weighting based on the spin must be applied to the SHT. This is discussed later in EQ. 1.31.

The CMB angular power spectrum measured by several experiments is shown in FIG. 1.3. The data points come from COBE, Toco, BOOMERanG, MAXIMA, WMAP, SPT, ACT, and Planck experiments. All the data are extracted from *NASA LAMBDA*⁷ website. The error bars in the measurement correspond to the instrumental errors of the experiment. The error bars in the original Planck data also include the *cosmic variance* and I have removed them for clarity.

1.3. Cosmic Inflation

With the discovery of the CMB, and the successful prediction of the abundances of light elements *via* Big-Bang nucleosynthesis (BBN), the Big-Bang model of cosmology prevailed over its competitor, the Steady State theory for the evolution of the universe. *viz.*

⁵This equation also holds for all sky measurements when masking is applied to remove potential contaminants that affect the measurements. For example, masking the galactic plane.

⁶The f_{sky} will be slightly lower after applying the masking to remove contaminations from foreground, and point sources.

⁷<http://lambda.gsfc.nasa.gov/product/>

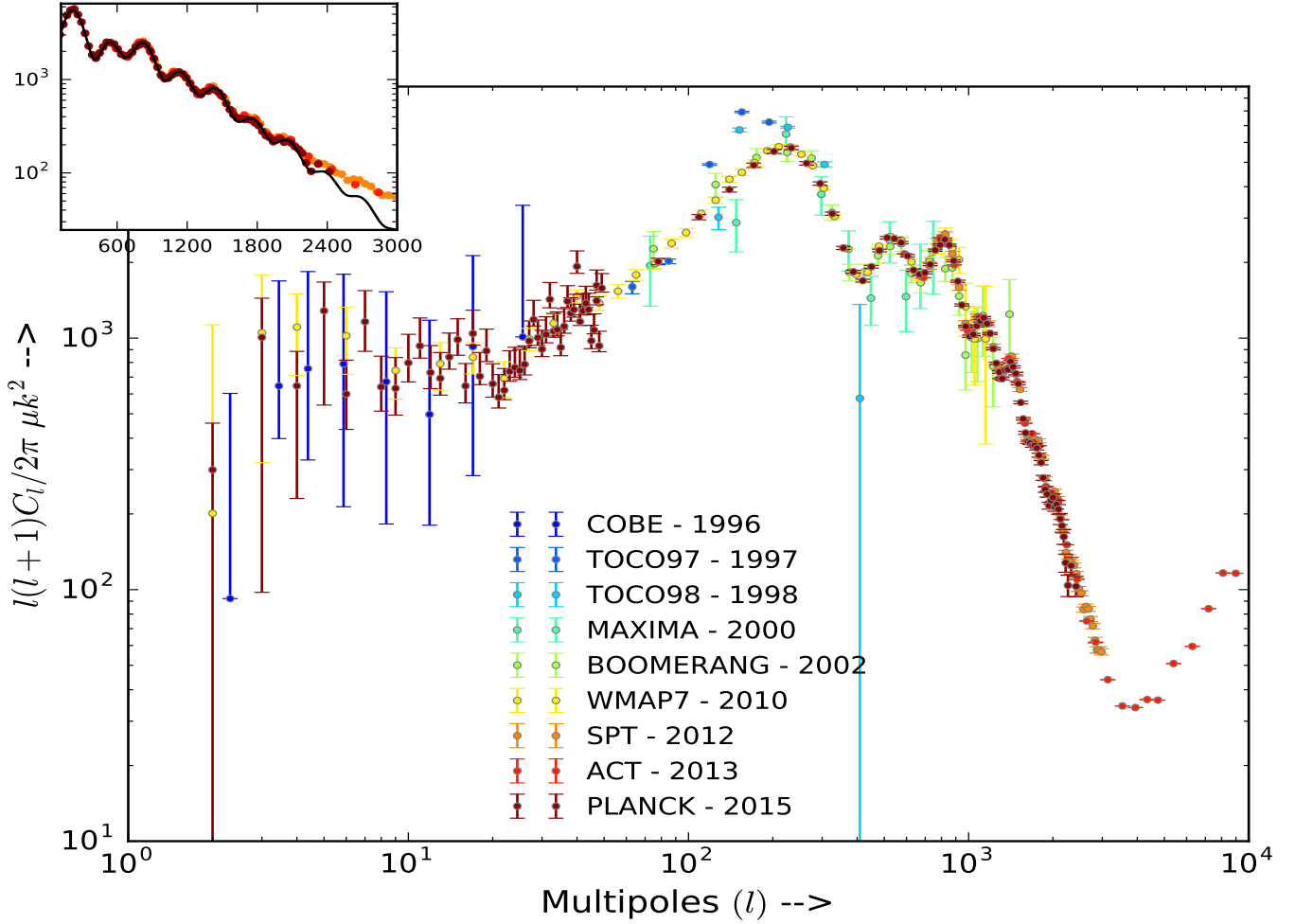


Figura 1.3: CMB angular power spectrum measured by the experiments COBE, Toco, BOOMERanG, MAXIMA, WMAP, SPT, ACT, and Planck experiments. The colour scale (not linear) represents the data release year starting from COBE (1996) to Planck (2015). The error bars in the Planck data also include the *cosmic variance* and I have removed them for clarity. No best fit Λ CDM curve is fit to the power spectrum as it is quite easy to guess just form the data points. The curve generated using the tool Code for Anisotropies in the Microwave Background (CAMB) [11] for Λ CDM is shown as black curve along with data points from ACT, Planck, and SPT are shown in the inset plot for reference. The mismatch between the Λ CDM curve and the data points at small scales (higher multipoles) arise due to the power from secondary anisotropies *viz.* SZ effect, dwarf galaxies.

- flatness problem - The flatness of the geometry of the universe with $\Omega_{\text{total}} = 1$ which is actually an unstable solution in the Big-Bang cosmological model.
- horizon problem - The correlations in temperate between two points (on CMB maps) at distances that are outside the size of the horizon during the time of recombination.
- monopole problem - The symmetry breaking at ultra high energies during the Big-Bang leads to the production of magnetic monopoles which have never been observed.

The cosmic inflation is a theory of accelerated expansion of the universe and was proposed

to solve the problems faced by the Big-Bang cosmology. The two points that are causally disconnected during recombination were in fact inside the horizon before inflation stretched them to super horizon scales. The exponential increase of the scale factor during the 60 e-folds of inflation flattens the spatial curvature of the universe and drives Ω_{total} to unity. The exponential expansion also dilutes the magnetic monopoles leading to their non-existence at the present day [14].

1.3.1. The theory of accelerated expansion

The inflationary cosmology was proposed in the 1980's independently by [15],[16],[17] and has undergone several revisions since then. The currently accepted model of the cosmic inflation is called the *single-field slow-roll* (SFSR) inflation in which a hypothetical scalar field called *inflaton* rolls slowly down a potential well resulting in an exponential expansion of the universe [13]. To understand this process better, we will use the Friedmann equation EQ. (1.3) and consider a simple model using a scalar field with an almost unchanging potential $V(\phi)$ as in the FIG. 1.4). The Friedmann equation is

$$\left[\frac{\dot{a}(t)}{a(t)} \right]^2 = \frac{8\pi G\rho}{3c^2} - \frac{k c^2}{a^2(t)} \quad (1.12)$$

where the second term on the right hand side is zero for a flat universe with curvature $k = 0$. Further, we will work in the units where the velocity of light $c = 1$ as it is common in cosmology.

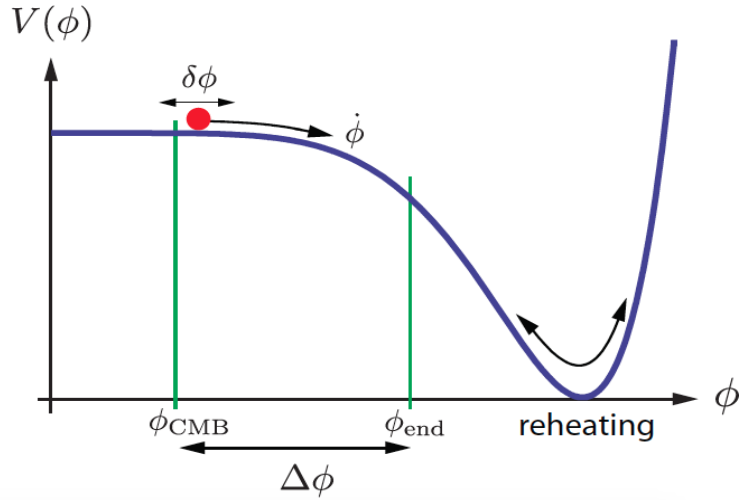


Figura 1.4: A toy model of SFSR inflation showing the slow roll of the scalar field ϕ down the potential well. The kinetic energy of the field is low compared to the potential energy when ϕ is small maintaining an almost constant potential $V(\phi)$ and the universe expands exponentially during this period. The quantum fluctuations $\delta\phi$ forms the seeds of the current structures in the universe. Image obtained from [14].

For a particular field value ϕ , the energy density will be $\rho = \frac{\dot{\phi}^2}{2} + V(\phi)$ corresponding to the kinetic (K.E), and potential (P.E) energy terms. During inflation when the scalar field filled

the entire universe, and hence ρ corresponds to the energy density of the universe.

$$\left[\frac{\dot{a}(t)}{a(t)} \right]^2 = \frac{8\pi G}{3} \left[\frac{\dot{\phi}^2}{2} + V(\phi) \right] = \text{constant} \quad (1.13)$$

$$H^2 = \left[\frac{\dot{a}(t)}{a(t)} \right]^2 = \text{constant} \quad (1.14)$$

The K.E term is set to zero as the scalar field rolls slowly, and the energy density is dominated by the P.E term $V(\phi)$ which is almost constant. So,

$$\frac{\dot{a}(t)}{a(t)} = H \quad (1.15)$$

resulting in an exponential expansion $a(t) = e^{Ht}$, and the Hubble parameter H is

$$H = \sqrt{\left(\frac{8\pi G V(\phi)}{3} \right)} \quad (1.16)$$

Let us now look at the field ϕ closely to understand the reason for the “almost” constant energy density. Given the above energy density ρ , the total energy E , and the Lagrangian \mathcal{L} of the field in an expanding universe are given by

$$E = \left[\frac{\dot{\phi}^2}{2} + V(\phi) \right] a^3(t) \quad (1.17)$$

$$\mathcal{L} = \left[\frac{\dot{\phi}^2}{2} - V(\phi) \right] a^3(t) \quad (1.18)$$

where $a^3(t)$ corresponds to the volume of the universe. The equations of motion of ϕ is

$$\frac{d}{dt} \frac{\partial \mathcal{L}}{\partial \dot{\phi}} = \frac{\partial \mathcal{L}}{\partial \phi} \quad (1.19)$$

$$\frac{d}{dt} \dot{\phi} a^3(t) = - \frac{\partial V(\phi)}{\partial \phi} a^3(t) \quad (1.20)$$

$$\ddot{\phi} + 3 \frac{\dot{a}}{a} \dot{\phi} = - \frac{\partial V(\phi)}{\partial \phi} \quad (1.21)$$

$$\ddot{\phi} + 3H\dot{\phi} = - \frac{\partial V(\phi)}{\partial \phi} (= F) \quad (1.22)$$

where the last equality takes into account of the fact that the force F is the negative gradient of the potential. The last equation represents the equation of the damped harmonic oscillator (DHO). Thus, the universe behaves as a DHO with the expansion of the universe acting as the friction term to slow down the acceleration of the field maintaining it at an almost constant potential. A constant potential means a constant energy density which results in the exponential expansion $a(t) = e^{Ht}$.

1.3.2. Parameterisation, and models of Inflation

The equations above show the simplest method of producing an exponential acceleration of the universe using a single scalar field. However, there are several other, close to 200 models of SFSR inflations [18]. There are also models with multiple scalar fields. There is also a possibility that the minimum that the scalar field lands into in the SFSR models is not the *true global minimum* but the *false local minima*. This is the case of *eternal inflation*⁸ in which the inflation occurs as the scalar field moves from the *local minima* to the *global minimum* via quantum tunnelling effects. The observation of *tensor B-modes* (see section 1.4) will help to constrain various inflation models. Refer to lecture by Daniel Baumann [14] for more details about inflation.

The slow-roll inflationary models are parametrised by two slow-roll parameters

$$\epsilon = -\frac{\dot{H}}{H^2} = -\frac{d \ln H}{dN} \quad (1.23)$$

$$\eta = -\frac{\ddot{\phi}}{H\dot{\phi}} = \epsilon - \frac{1}{2\epsilon} \frac{d\epsilon}{dN} \quad (1.24)$$

The exponential acceleration occurs when $\epsilon \ll 1$, and continues until $|\eta| > 1$. In the DHO equation above (EQ. 1.22), the inflation continues until the friction term balances the force that causes the exponential expansion

$$\dot{\phi} = -\frac{dV(\phi)}{d\phi} \frac{1}{3H} \quad (1.25)$$

1.4. Perturbations, and the Inflation observables

Perturbations

The inflationary model of cosmology not only solves the *flatness, horizon, and monopole* problems of the Big-Bang cosmology, but also explains the origin of the small anisotropies that exist in the CMB that was described earlier in section 1.2. The anisotropies are generated due to the quantum fluctuations $\delta\phi$ when the scalar field rolls down the potential well like in FIG. 1.4. The tiny uncertainty in the field value results in a slightly different evolution of

⁸This model was favoured when BICEP2 [26] released the first detection of tensor B-modes with $r = 0.2$.

different regions of the universe sourcing the primordial perturbations on a smooth isotropic background FRW metric (universe). The perturbations were linear, and evolution of the perturbations depend on their scale.

Using *scalar-vector-tensor (SVT) decomposition*, the linear perturbations can be decomposed into their independently evolving scalar, vector, and tensor components. The *scalar perturbations* are the fluctuations in the energy density and are the observed temperature anisotropies on the CMB. They form the seeds of the structures like galaxies, and the galaxy clusters that we see in the local universe. The *tensor perturbations* are the perturbations to the metric and *will be observed as gravitational waves*. These are the *primordial gravitational waves (PGW)* from inflation. But the amplitude of the PGW is so low, and it is impossible to observe them directly unlike the attempts to observe gravitational waves generated due to astrophysical sources. However, the *PGW leave distinct imprints on the polarised CMB* which can be detected using state of the art instruments. Both the scalar (density), and tensor (PGW) perturbations are predicted by many models of inflation. The *vector perturbations* are often considered unimportant primarily because they tend to dilute in an expanding universe, and secondly because many inflation models do not predict them.

Parameterisation

The primordial scalar, and tensor perturbations are both characterised using their amplitude, and scale dependance in a simple power law form.

$$P_s(k) = A_s(k_{\text{pivot}}) \left(\frac{k}{k_{\text{pivot}}} \right)^{n_s - 1} \quad (1.26)$$

$$P_t(k) = A_t(k_{\text{pivot}}) \left(\frac{k}{k_{\text{pivot}}} \right)^{n_t} \quad (1.27)$$

where k_{pivot} is an arbitrary reference scale of measurement. Inflation predicts a scale invariant spectrum with $n_s = 1, n_t = 0$. Some models of SFSR, however, predict a slight scale dependance of the $P_s(k)$ with n_s slightly less than one. There is also a scale dependance of n_s commonly denoted as $\alpha_s = \frac{dn_s}{d\ln k}$. A subtle point to be noted here is that, if α_s is non-zero, then the choice of the pivot scale cannot be set arbitrarily.

The ratio between $P_t(k)$, and $P_s(k)$ is also an interesting quantity called the *tensor-to-scalar ratio* $r = \frac{P_t(k)}{P_s(k)}$, and is often used to characterise the amplitude of tensor perturbations A_t with respect to the scalar $A_s = 2.44 \times 10^{-9}$ [19]. Since A_s , and n_s has been measured precisely using the CMB temperature anisotropies, the measurement of r will give us the energy $V(\phi)$ of inflation as in EQ. 1.28.

$$V(\phi)^{1/4} = \left(\frac{r}{0.01} \right)^{1/4} 10^{16} \text{ GeV} \quad (1.28)$$

It is because of this, that the observations of tensor perturbations are often referred to as the *smoking gun* of inflation. The tensor perturbations are predicted to be an order of magnitude lesser than the scalar perturbations, and hence it has been a challenge to observe them. FIG. 1.6 show the tensor power C_l^{BB} spectrum for different values of r in green colour. We will

come back to this figure in the next section, but it is clear that the tensor power spectrum C_l^{BB} is extremely small as compared to the temperature power spectrum C_l^{TT} (black). The current upper limits on the value of $r_{pivot=0.002} < 0.11$ comes from the recent Planck results [21].

Observables

Thus the (angular) power spectrum of the CMB, and the galaxy power spectra form the main *observables of inflation*. The power spectrum, as already discussed, is the two-point (angular in case of CMB) correlation function from the CMB maps and holds all the information about the primordial fluctuations only if they are Gaussian random fluctuations. Otherwise, we will require three-point correlation function to fully quantify the primordial non-Gaussian fluctuations. Most of the observables predicted by inflation have been confirmed by current cosmological observations *viz.*

- the (nearly) scale invariant nature of the primordial power spectrum (PPS) over large scales necessary for the origin of the LSS of the universe. Many models of inflation predict a very small scale dependence of the PPS and it has been confirmed by the CMB experiments with $n_s = 0.968 \pm 0.006$ [19].
- absence of primordial non-Gaussianity with $f_{NL}^{\text{local}} = 2.5 \pm 5.7$ [20] in accordance with the simplest models of inflation.
- And of course, the absence of curvature, the initial causal connection of scales that cannot be causally connected now, and the absence of magnetic monopoles.

The yet unobserved quantities *viz.* the tensor-to-scalar ratio r , running of the scalar spectral index α_s , the scale dependance of the tensor perturbations n_t , and the primordial non-Gaussianity f_{NL} will allow us to understand the physics of inflation and constrain different models of inflation.

1.5. Polarised CMB

The CMB by itself is unpolarised. But, the CMB that we see are (partially) linearly polarised because of the Thomson scattering of the CMB photons (quadrupole component of the temperature anisotropies to be exact) by the free electrons at the surface of last scattering. Before recombination the photons were tightly coupled to the free electrons, and hence there would not be any quadrupole anisotropy. The isotropic scattering of the photons when they were tightly coupled to electrons cannot produce polarisation. It is only during the period of recombination, the photons decoupled from the free electrons generating small quadrupole anisotropies. As a result, the amount of the polarisation of the CMB is expected to be only a fraction of the temperature anisotropies and depends on the length of the period of recombination. This is the reason that the polarisation power spectrum of CMB is much harder to measure as compared to the temperature power spectrum. Since no circular polarisation can be produced by scattering, the CMB is not expected to be circularly polarised. The presence

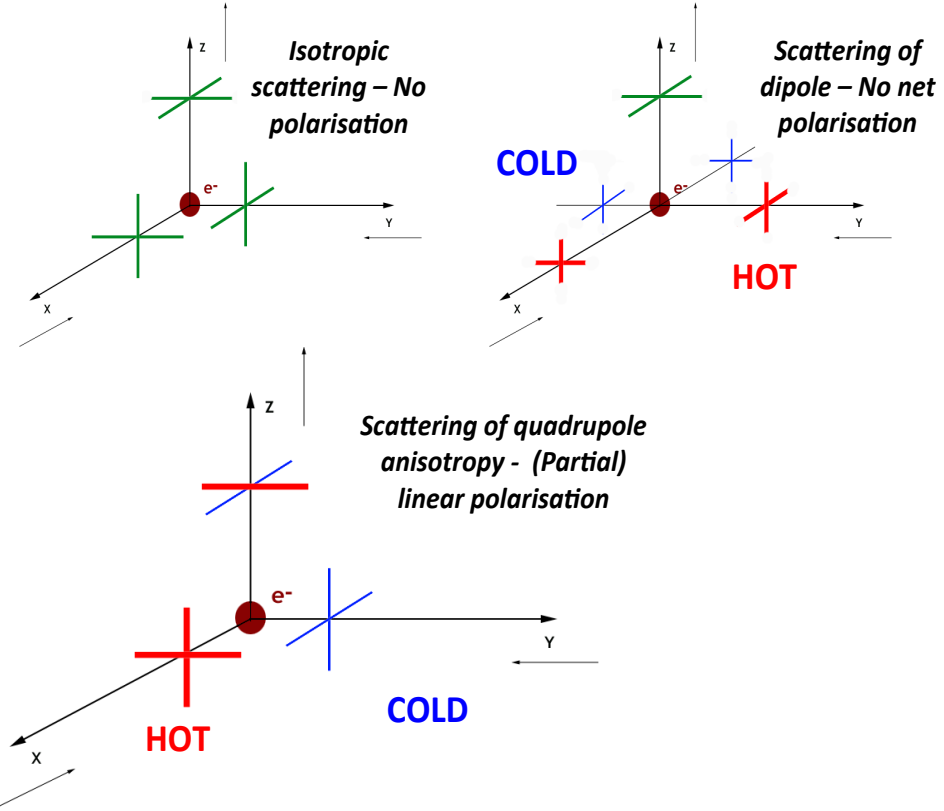


Figura 1.5: Three different cases experienced by an electron at the surface of last scattering. The colours represent the temperature of the CMB photons - cold = blue; hot = red; average = green. The figure on the top left (right) shows that no net polarisation would be produced if the electron only sees monopole (dipole) component of the temperature anisotropy. The bottom figure shows the (partial) linear outgoing polarisation due to the quadrupole anisotropy of the surrounding photons during the period of recombination. The figures were generated based on the materials by Hu & White [22], and Dodelson [2].

of anisotropies in the polarisation apart from the temperature anisotropies is an exceptional feature of CMB facilitating the observation of the imprints of the PGW as *tensor B-modes* on the polarisation power spectrum.

The process of producing CMB polarisation *via* Thomson scattering is shown in FIG. 1.5. The three figures correspond to the three different cases that an electron at the surface of last scattering can experience because of the surrounding CMB photons. The colours represent the temperature of the CMB photon - cold = blue; hot = red; average = green. The figure on the top left shows that no net polarisation would be produced by the electron scattering if the temperature of the CMB photons arriving from orthogonal directions are the same. This is mostly the case before recombination. The figure on the top right shows the scattering of a dipole radiation by an electron. Again, the net polarisation is zero as the temperature of the CMB photons that the electron see in the orthogonal directions are the same. Finally during the period of recombination the decoupling allows the electron to see the quadrupole anisotropy of the surrounding photons like in the bottom figure and this results in a (partial) linear outgoing polarisation.

1.5.1. Perturbations, and the polarisation patterns

The Thomson scattering of (quadrupole) temperature anisotropies is the reason for the generation of the polarisation. The temperature anisotropies were indeed because of the primordial scalar and tensor perturbations from inflation as described in the previous section 1.4. We ignore the vector perturbations as they vanish in an expanding universe. So observing the polarisation of the CMB allow us to study the primordial perturbations. Moreover, the scalar (energy density), and the tensor (gravitational wave) perturbations (at the surface of last scattering) leave different signatures on the polarised CMB. Hence the CMB polarisation can be used to extract information about the tensor perturbations, and eventually allow to study about the physics of inflation.

The polarisation pattern on the CMB sky can be decomposed into *curl-free E-modes*, and *divergence-free B-modes*. This is similar to Maxwell's equation where the curl of the electrostatic field, and the divergence of the magnetic field are zero. The reason the polarisation patterns are called E, B modes is because of this similarity to electromagnetism.

$$\vec{\nabla} \times \vec{E} = 0 \quad (1.29)$$

$$\vec{\nabla} \cdot \vec{B} = 0 \quad (1.30)$$

The most important reason for this decomposition is that the scalar perturbations only generate E-modes but does not generate B-modes, and the tensor perturbations generate both E, and B-modes in equal amounts. The E, and B-modes form particular patterns around hot, and cold spots. The E-modes appear radial (tangential) around cold (hot) spots because of the divergence. The B-modes exhibit vorticity because of the non vanishing curl. If seen through the line going through their centres, the reflection of the E-modes remain unchanged while the pattern of the B-modes are reversed. On the polarised (CMB) field, using the explanation from Hu & White [22], the direction between *the local polarisation and the direction of the greatest change in polarisation* are either oriented parallel or perpendicular for E-modes, and at 45 degrees for B-modes. The E, and B-modes are coordinate independent entities and a global phenomena. Refer to Hu & White [22] for more details about the E, and B-modes.

But the detectors on the CMB experiments measure the polarisation which are characterised by the coordinate dependent Stokes parameters Q, and U. However, there is a linear transformation between the Q, U Stokes parameters and the E, and B-modes (see EQ .1.31, 1.34). The four Stokes parameters are I denoting intensity, Q, U describing the amount of linear polarisation, and V denoting the circular polarisation. Since the circular polarisation is absent for CMB, the detectors used in most of the CMB experiments are insensitive to circular polarisation⁹. The CMB polarisation experiments normally make maps of the Q, U Stokes parameters from their measurements. While it is possible to produce E, B maps using the transformation from Stokes parameters it is normally not preferred because of the mixing between E and B due to partial sky coverage and masking. As will be seen in section 6.1 this mixing is handled at the power spectrum estimation stage.

⁹CLASS telescope currently being deployed in the north of Chile can also detect circular polarisation. For example, the Faraday rotation due to the 1. primordial magnetic fields can affect the CMB polarisation, 2. magnetic field in our galaxy can rotate E-modes to B-modes.

Since polarisation is a spin-2 field unlike temperature which are scalars, the simple SH transformation is not valid for Q and U. A weighting term that accounts for their spins must be added like in EQ. 1.31

$$\begin{aligned}(Q + iU)(\hat{n}) &= \sum_{l,m} a_{2,lm} {}_2Y_{lm}(\hat{n}) \\(Q - iU)(\hat{n}) &= \sum_{l,m} a_{-2,lm} {}_{-2}Y_{lm}(\hat{n})\end{aligned}\quad (1.31)$$

where a_{lm} are the coefficients of the SH Y_{lm} . From EQ. 1.31, and 1.34, the E, and B-modes can be obtained as

$$\begin{aligned}a_{E,lm} &= -\frac{a_{2,lm} + a_{-2,lm}}{2} \\a_{B,lm} &= -\frac{a_{2,lm} - a_{-2,lm}}{2i}\end{aligned}\quad (1.32)$$

yielding the fields

$$\begin{aligned}E(\hat{n}) &= \sum_{l,m} a_{E,lm} Y_{lm}(\hat{n}) \\B(\hat{n}) &= \sum_{l,m} a_{B,lm} Y_{lm}(\hat{n})\end{aligned}\quad (1.33)$$

From 1.9, 1.34 we have 3 equations that completely describe the temperature, and polarisation fields of the CMB. From these fields, we can compute the two-point correlation functions (power spectra) between “almost” all these fields (i.e:) auto, and cross correlation between the fields. There is no (cross) correlation between $X_{\text{corr}}(T, B)$, $X_{\text{corr}}(E, B)$. Accordingly the three auto correlations are

$$C_l^{TT} = \frac{1}{2\ell+1} \sum_m \langle a_{T,lm} a_{T,lm}^* \rangle \quad (1.34)$$

$$C_l^{EE} = \frac{1}{2\ell+1} \sum_m \langle a_{E,lm} a_{E,lm}^* \rangle \quad (1.35)$$

$$C_l^{BB} = \frac{1}{2\ell+1} \sum_m \langle a_{B,lm} a_{B,lm}^* \rangle \quad (1.36)$$

and the only cross correlation entity

$$C_l^{TE} = \frac{1}{2\ell+1} \sum_m \langle a_{T,lm} a_{E,lm}^* \rangle \quad (1.37)$$

$$(1.38)$$

Measuring the quantity C_l^{BB} is the goal of experiments listed in FIG. 1.1 *via* the unique B-mode signature of the tensor perturbations. The primordial C_l^{BB} power spectrum is shown for different values of tensor-to-scalar ratio r in FIG. 1.6 as different green lines. The other curves correspond to the following. The red line corresponds also to B-mode power spectrum but they are from the *weak gravitational lensing* of galaxy clusters and not due to the PGW from inflation. The lensing B-modes have been discovered by SPTPol [24], and POLARBEAR [25] shown as cyan points. For comparison, the temperature auto correlation C_l^{TT} is also shown in black. The B-modes are several orders of magnitude smaller than TT power spectrum.

The C_l^{EE} due to scalar E-modes (blue) was first observed by DASI experiment based on the south-pole [23]. The $X_{\text{corr}}(T, E)$ have also been studied extensively by several experiments. The TE power spectrum is not shown in FIG. 1.6 to avoid too many curves in the figure. Only the primordial tensor B-modes remain undiscovered till date. On 17th March 2014, BICEP2 experiment reported the first detection of the tensor B-modes [26] (shown as magenta points) but the result was later attributed to the dust from the foreground [27]. All the curves have been computed using the CAMB tool [11].

The white band is the multipole range $40 \leq \ell \leq 400$ is the region to which the ABS telescope is highly sensitive. The probable errors in the ΔC_ℓ^{BB} measurements for $r = 0.05$ are also shown. The errors have been decomposed into two components *viz.* the sample variance (black) (EQ. 1.11), and instrumental errors (yellow band). The errors C_ℓ^{noise} have been calculated using the *Knox formalism* [28, 29] for realistic ABS parameters (see later sections) and added to the power spectrum just like in the EQ. 1.11

$$C_\ell^{\text{noise}} = \frac{\Omega_{\text{ABS}} s^2}{t_{\text{obs}} B_\ell^2} \quad (1.39)$$

where $s = 40 \text{ uK } \sqrt{\text{sec}}$ is the ABS array sensitivity (FIG. 2.4), bin-width $\Delta\ell = 30$, $\Omega_{\text{ABS}} = 2\pi \left(\frac{\sigma_{\text{ABS}}}{\sqrt{8\log(2)}} \right)^2 \sim 100.5 \text{ } \mu\text{sr}$ is the main-beam solid angle, $\sigma_{\text{ABS}} = 32.4 \pm 1 \text{ arcmins}$ is the FWHM of the ABS Gaussian main-beam (FIG. 3.10), B_ℓ is the beam window function calculated for a Gaussian beam (EQ. 3.25, FIG. 3.8), and $t_{\text{obs}} = 1920 \text{ hours}$ (in seconds) corresponds to the number of observation hours after data selection used for map making (FIG. 4.1).

1.6. Challenges and current status of CMB experiments

At large scales, the presence of correlated $1/f$ noise can present serious challenges to the data. However, the rapid polarisation modulation using a warm Half Wave Plate (HWP) (section 2.5) reduces the unpolarised atmospheric noise for ABS. At small angular scales (large ℓ s) the ABS is limited by the beam resolution. The effects of weak gravitational lensing further worsens the primordial B-mode measurements at small angular scales by converting scalar E-modes to tensor B-modes due to shear. The other serious contaminant is the foreground from the Milky Way. For ABS, the foreground is being modelled using the data all frequency channels of the WMAP experiment for *synchrotron* [30], and the Planck HFI 353 GHz channel for the *dust* [44]. We use the maps of the Stokes parameters Q and U in both cases.

The next generation of CMB experiments are dedicated to explore the polarisation properties of the CMB. Many of them are looking to detect and characterise the primordial B-mode spectrum as it is the only realistic cosmological probe to study the physics of inflation. The current best upper bound on the *tensor-to-scalar* ratio of $r < 0.09$ using only the polarisation data comes from the combined datasets of BICEP2 (150 GHz) and Keck Array (95 GHz) [31]. The previous best bound of $r < 0.72$ was also from BICEP [32] experiment. The QUIET

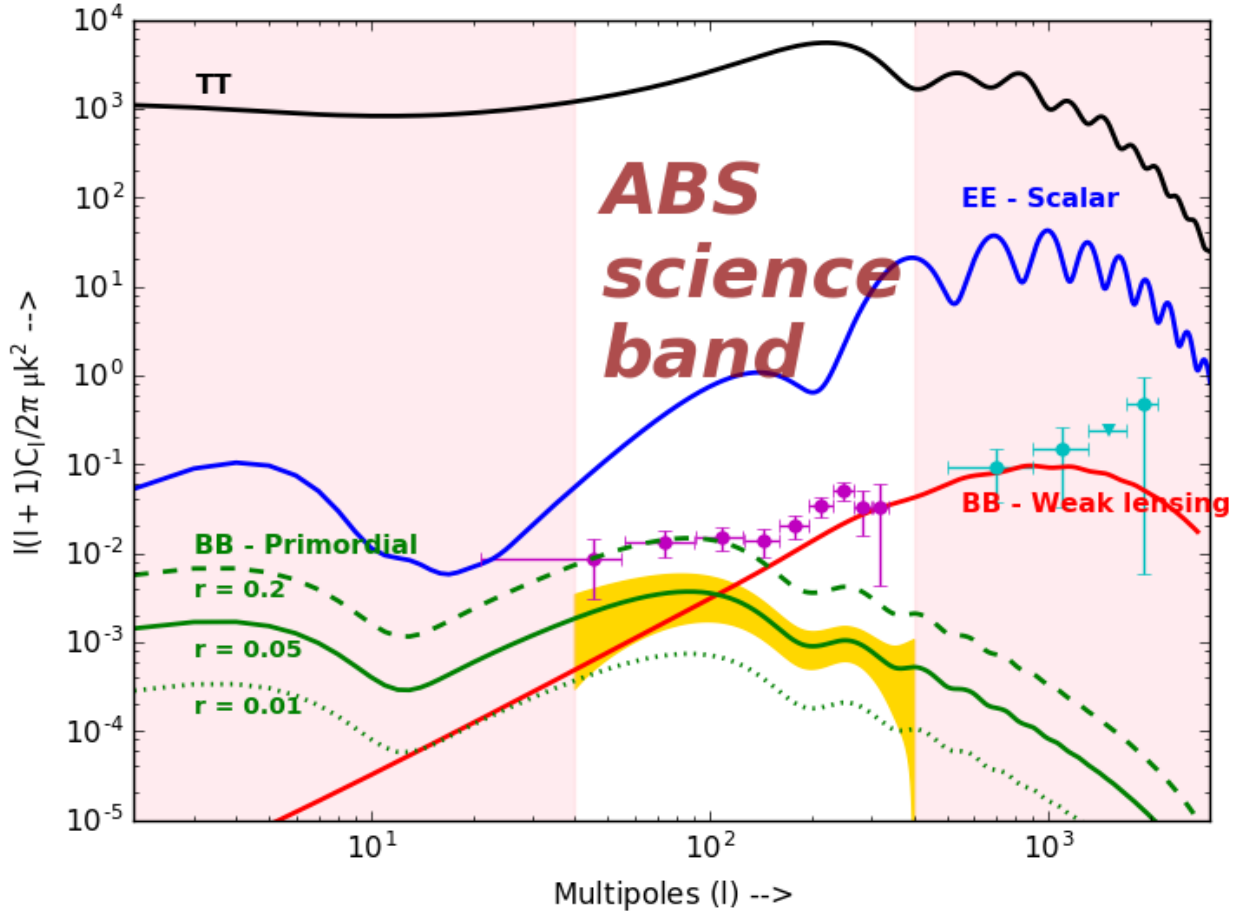


Figura 1.6: Temperature, E, and B-mode polarisation power spectrum. Black and red solid curves represent the temperature, and gravitational weak lensing power spectrum. The scalar E-mode spectrum is shown in blue. The green curves show the tensor B-mode power for different tensor to scalar ratios $r=0.2$ (dashed), $r=0.05$ (solid), and $r=0.01$ (dotted). All the curves are generated using the CAMB tool [11] for the standard Planck Λ CDM model. The data points from BICEP2 [26], and POLARBEAR [25] for the reported measurements of primordial, and lensing B-modes are shown as magenta and cyan points. The white band is the multipole range $40 \leq l \leq 400$ is the region to which the ABS telescope is highly sensitive. The errors due to sample variance and the instrumental noise (yellow band) was calculated as described in the text are also shown for $r = 0.05$.

experiment published an upper bound of $r < 2.2$ [41]. The reported primordial detection at $r = 0.2$ by BICEP2 [26] has been attributed to foreground contamination [27]. The most promising ongoing and future primordial B-mode experiments include Keck array operating at multiple frequencies, and BICEP3 at the South pole; experiments at Chile *viz.* ACTPol and AdvACTPol (observing at three different frequencies), CLASS, POLARBEAR (which recently switched to observe large patches of sky), POLARBEAR-2, and Simons array. All of the instruments operating from Chile either use or plan to use HWP for rapid polarisation modulation. This is after the successful performance of the HWP for ABS.

Some high angular resolution experiments like SPTPol, SPT-3G, ACTPol, and AdvACTPol are aiming to measure the lensing of the CMB to a very high degree of precision. The data can be combined with Dark Energy Survey (DES), Large Synoptic Survey Telescope (LSST) to constrain models of dark energy by measuring the gravitational potential along the line of sight to the last scattering surface. The CMB polarisation measurements can also help in understanding the physics of reionisation and distribution of the galactic and extra galactic magnetic fields [33].

Capítulo 2

THE ATACAMA B-MODE SEARCH

Overview, and goals:

This section contains details about the ABS instrument, observation strategy and scheduling, data acquisition, and the HWP demodulaiton technique. My work focussed particularly on

- scheduling the CMB, and other calibration observations during the second, and third seasons.
- monitoring the telescope using automatic python scripts.
- perform low-level data analysis to check the data quality.

2.1. The Instrument

The Atacama B-mode Search (ABS) experiment is devoted to the measurement of primordial tensor B-mode polarisation at large angular scales ($\sim 1^\circ$) in the multipole range $45 \leq l \leq 400$ (green band in FIG. 1.6). It was deployed on Cerro Toco at the Atacama desert in the north of Chile at an altitude of 5190 metres in February 2012 and became operational immediately. The ABS contains 240 feed-horns grouped equally in 24 triangular pods that were spread over the focal plane of the telescope. Each feed-horn consist of 2 polarisation-coupled Transition Edge Sensor (TES) detectors [35] (to detect orthogonal polarisation of the incoming light). The ABS is a cryogenic telescope with the focal-plane cooled by a $^3\text{He}/^4\text{He}$ adsorption refrigerator system to a temperature of 300 mK. There are two mirrors, 60 cms each arranged in a compact crossed-Dragone configuration. The mirrors were maintained at 4K using two pulse-tube coolers. The frequency of the operation is 145 GHz [34]. The beam size of ABS is ~ 32 arcmins¹ and the field-of-view is ~ 22 degrees.

The ABS also contains a continuously rotating ambient temperature half-wave plate

¹ABS does not need a high angular resolution as it probes the primordial gravitational waves that peak at large angular scales ~ 1 degree on the sky.

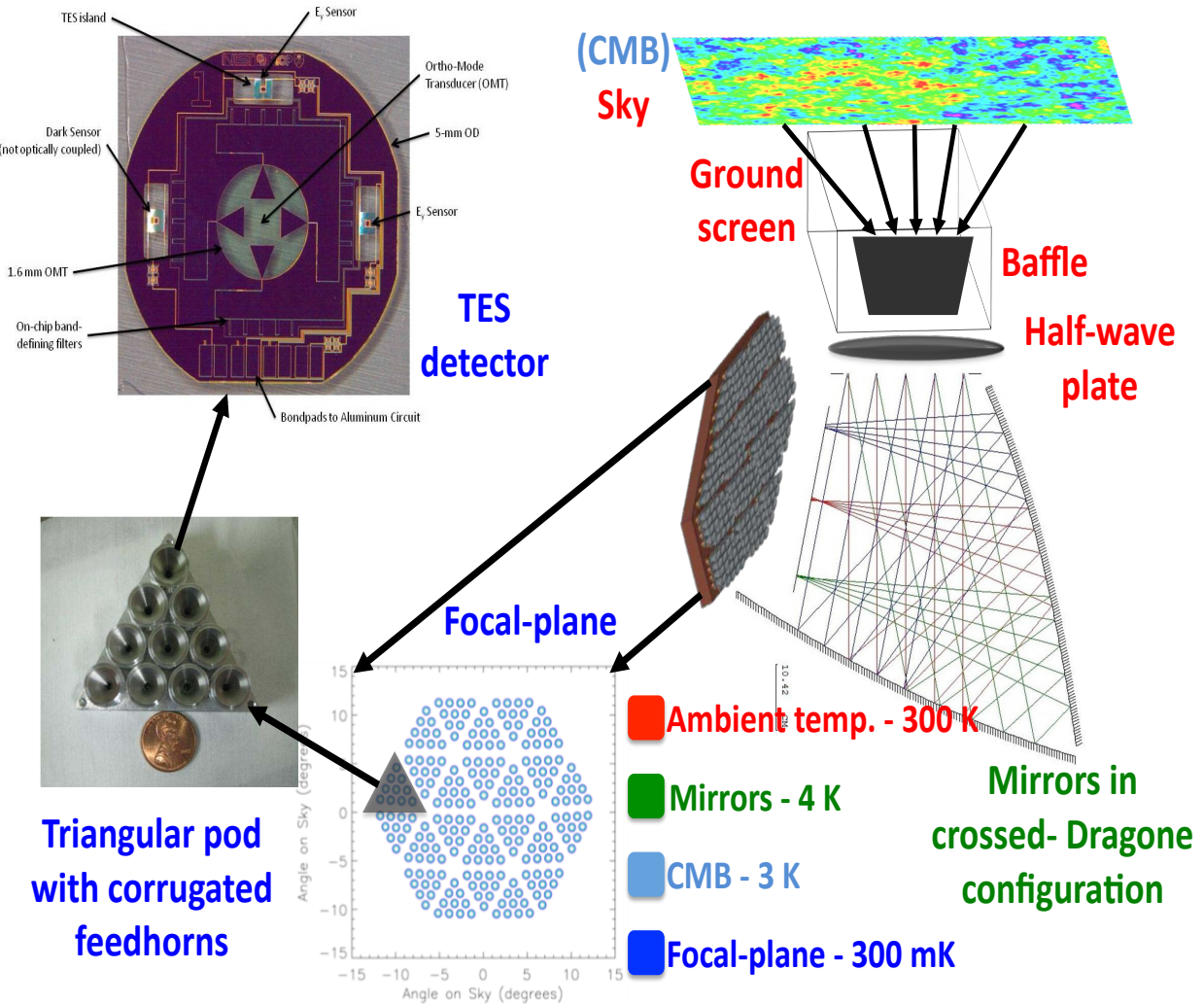


Figura 2.1: A schematic diagram showing the observation of the CMB sky using ABS. The CMB photon goes through the telescope *baffle* which blocks other undesired signals; crosses the *HWP* (the first optical element of ABS) and will be modulated; hits the *two mirrors* and captured by the detectors on the *focal-plane*. The *TES detectors* are placed behind the *corrugated feed-horns* which are planted onto the ABS *focal-plane*. The *ground screen* was installed after a month of the telescope deployment to prevent signals from far side-lobe of the telescope.

(HWP) for continuous polarisation modulation of the incoming CMB photons. The HWP rotates at a frequency of $f = 2.55\text{Hz}$. The central idea of using HWP is because of the fact that the atmosphere is unpolarised and only the polarised (CMB) signal component will be modulated by the HWP. The HWP modulates the incoming linearly polarisation of the CMB at a frequency that is four times ($4f=10\text{ Hz}$) the rotation frequency of the HWP, well above the knee frequency (atmospheric, and detector) to measure the small CMB polarisation. FIG. 2.1 shows a schematic diagram of the observation of the CMB sky using the ABS telescope. The ground screen [37], baffle, HWP, mirrors, focal-plane, feed-horns, and the TES detectors are shown in the figure. The text colours on the figure represent the different temperature at which each of the components are maintained. This figure is only a schematic, and please refer to FIG. 2.2 for a better understanding of the ABS instrument.

The ABS HWP was made out of an α -cut single crystal sapphire and was anti-reflection (AR) coated using Rogers RT/duroid 6002. The duroid is $305\text{ }\mu\text{m}$ glass-reinforced, ceramic-loaded polytetrafluoroethylene (PTFE) laminate with a refractive index of 1.71. The dimensions of the HWP is 330 mm in diameter and 3.15 mm thick. The HWP was supported by air bearings and lies just above the cold (4K) 25 cm aperture stop. It is the first optical element of the telescope which allows us to clearly distinguish between the polarisation generated by the instrument, and the sky signal. The polarised sky can be recovered efficiently from the demodulated timestreams. The use of HWP, of course introduces additional noise in the form of HWP Synchronous Signal ($A(\chi)$, see section 2.5) which are due to the thermal emission from the HWP itself. The $A(\chi)$ was found to be small and was removed from the raw TOD before demodulation. The demodulation technique is explained in section 2.5. More details about the ABS HWP refer to [36].

The ABS is the first ground-based CMB telescope to successfully perform a rapid polarisation modulation. The same technique was used earlier by the balloon-borne experiment called MAXIPOL to measure the CMB E-mode polarisation [47]. Another advantage of using a HWP is that it allows each detector to independently measure all the Stokes parameters for linear polarisation which otherwise uses the pair-differencing of the two detectors that are sensitive to orthogonal polarisations.

2.2. The site

The geographical location of the ABS telescope facilitates the polarisation modulation of the incoming signal *via* the rotation of the sky which is absent for the telescopes at the south pole. Note that this would be an additional modulation step besides the HWP modulation as described already. The exact geographical coordinates are given in Table 2.2.

One of the prime challenges for the ground-based CMB observations is the atmosphere. The reason is two fold. Firstly, the atmospheric emission chiefly due to water vapour (commonly referred to as precipitable water vapour PWV), and the molecular oxygen is immensely strong at the millimetre wavelengths, the observing wavelength of the CMB telescopes. Since the atmosphere is at a higher temperature ($\sim 300\text{K}$) compared to the CMB photon ($\sim 3\text{K}$), atmospheric emission introduces optical loading on the detectors. The detector (sensitivity)

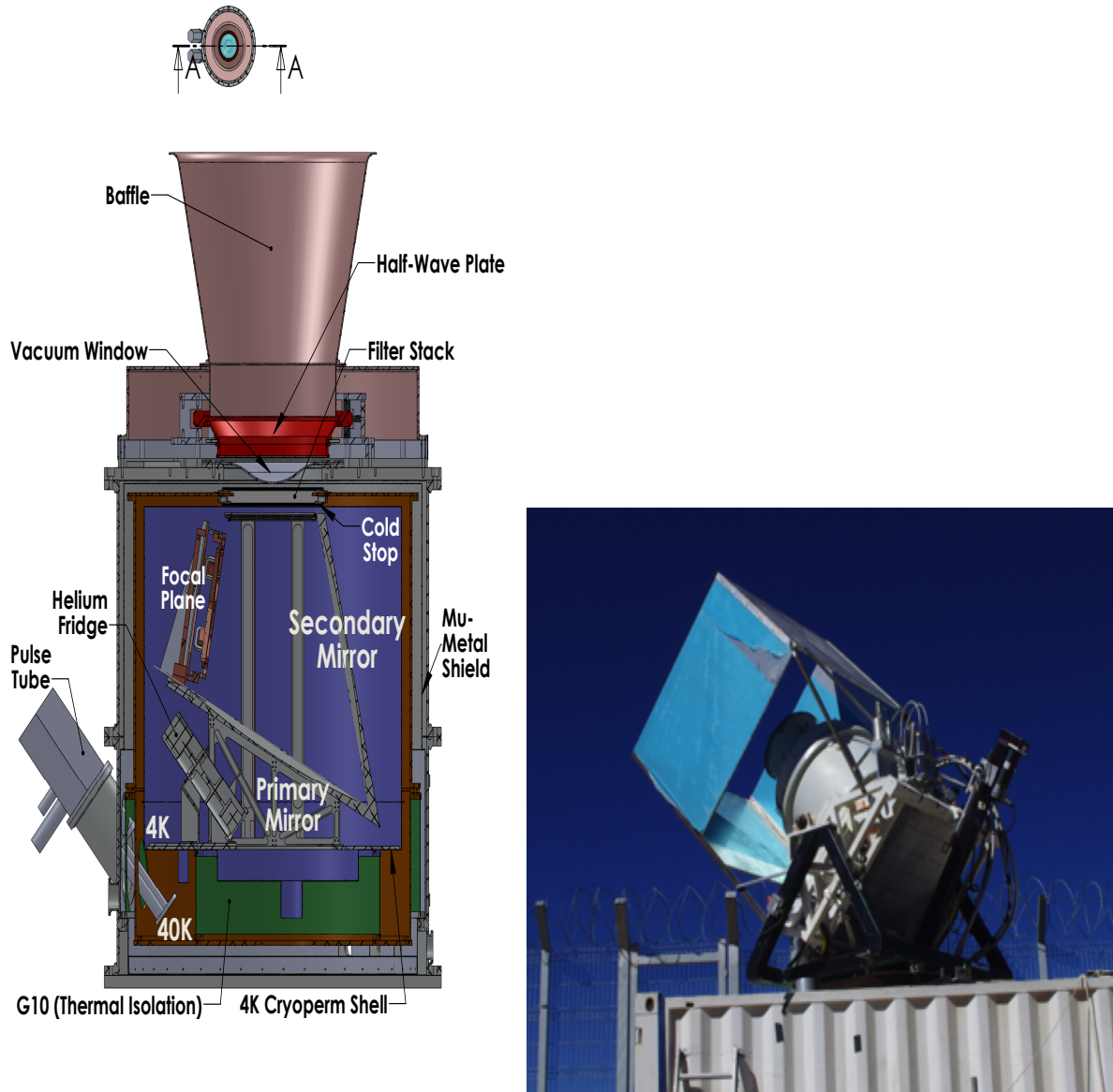


Figura 2.2: The left panel shows the ABS receiver demonstrating all the key components of the telescope *viz.* baffle, focal-plane, Helium fridge, HWP, mirrors, and the pulse tube cooler. Figure courtesy of Thomas Essinger-Hileman. The right panel shows the ABS telescope observing at Cerro Toco. The receiver in the left panel can be seen in white colour inside the giant blue ground screen. The telescope was mounted on top of a shipping container.

Tabla 2.1: Atacama B-mode Search - Information about the telescope location, and observation seasons.

Parameter	Values
Latitude	22.958° S
Longitude	67.787° W
Altitude	5190 metres
Minimum elevation	42°
Nominal pressure	55 mBar
Season 1	September 13, 2012 - December 26, 2012
Season 2	April 1, 2013 - February 2, 2014
Season 3	March 31, 2014 - October 1, 2014

performance limited by the photon-noise aggravates with the optical loading. Secondly, the atmosphere is not transparent at all wavelengths because of the absorption by different molecules. The atmospheric transparency in the sub-millimetre wavelengths at the Atacama Pathfinder Experiment (APEX) telescope location (*Llano de Chajnantor*) is shown in FIG. 2.3. The curves were calculated for different PWV levels using the APEX atmosphere model [38]. The absorption seen near 117, and 183 GHz correspond to the water molecules, and the molecular oxygen respectively.

This requires a careful selection of observation windows (low atmospheric absorption) for better transmission, and right PWV levels (low atmospheric emission) to reduce the loading and to maximise the detector performance. It is evident from the figure that the atmospheric transmission is optimal at low PWV levels in the ABS observing frequency range marked with black (red) horizontal lines for the ABS batch-A (batch-B) detectors. The batch A detectors were the detectors in the lower half of the focal-plane and had well measured bandpass responses compared to batch-B detectors from the upper half of the focal-plane.

The sensitivity (performance) of the ABS detectors is measured by the noise equivalent temperature (NET). For SNR of unity, NET is defined as the temperature of the signal required to match the photon (white) noise level of the detector. The unit of NET is normally $\mu\text{K}/\sqrt{\text{Hz}}$ or $\frac{1}{\sqrt{2}}\mu\text{K}\sqrt{\text{sec}}$ where the $1/\sqrt{2}$ is to convert $1/\sqrt{\text{Hz}}$ to $\sqrt{\text{sec}}$. The NET_{ABS} of the ABS detector array is calculated as EQ. 2.1

$$\text{NET}_{\text{ABS}} = \sum_{i=0}^N \left(\frac{1}{\text{NET}_i^2} \right)^{-\frac{1}{2}} \quad (2.1)$$

where N corresponds to the number of detectors that passed all the data cuts as discussed in section 4.1.1. The NET of each detector is calculated using the white noise amplitude from the $1/f$ noise model to the detector power spectrum.

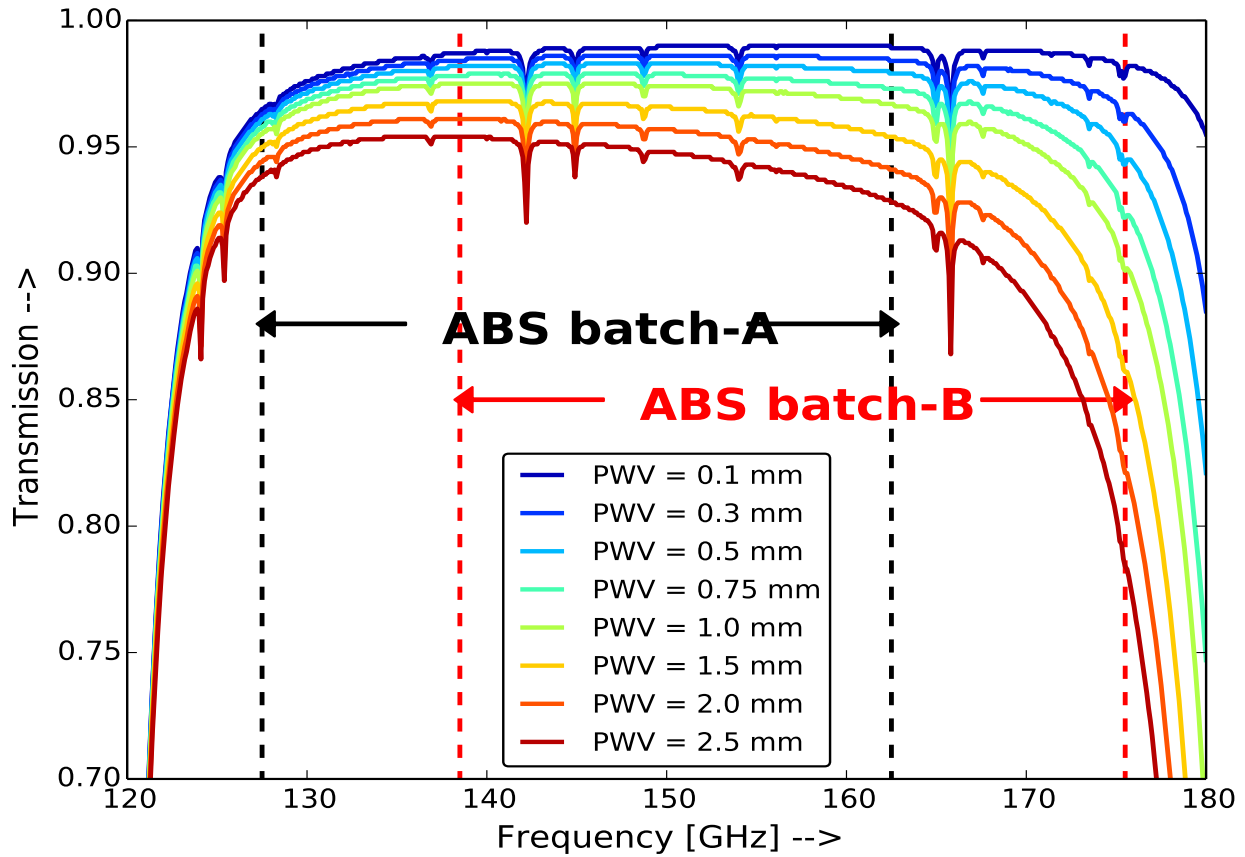


Figura 2.3: The atmospheric transmission at the ABS observing frequencies calculated using the APEX telescope atmosphere model [38] for different PWV levels at an elevation of 5100 metres at the *Llano de Chajnantor* in Chile.

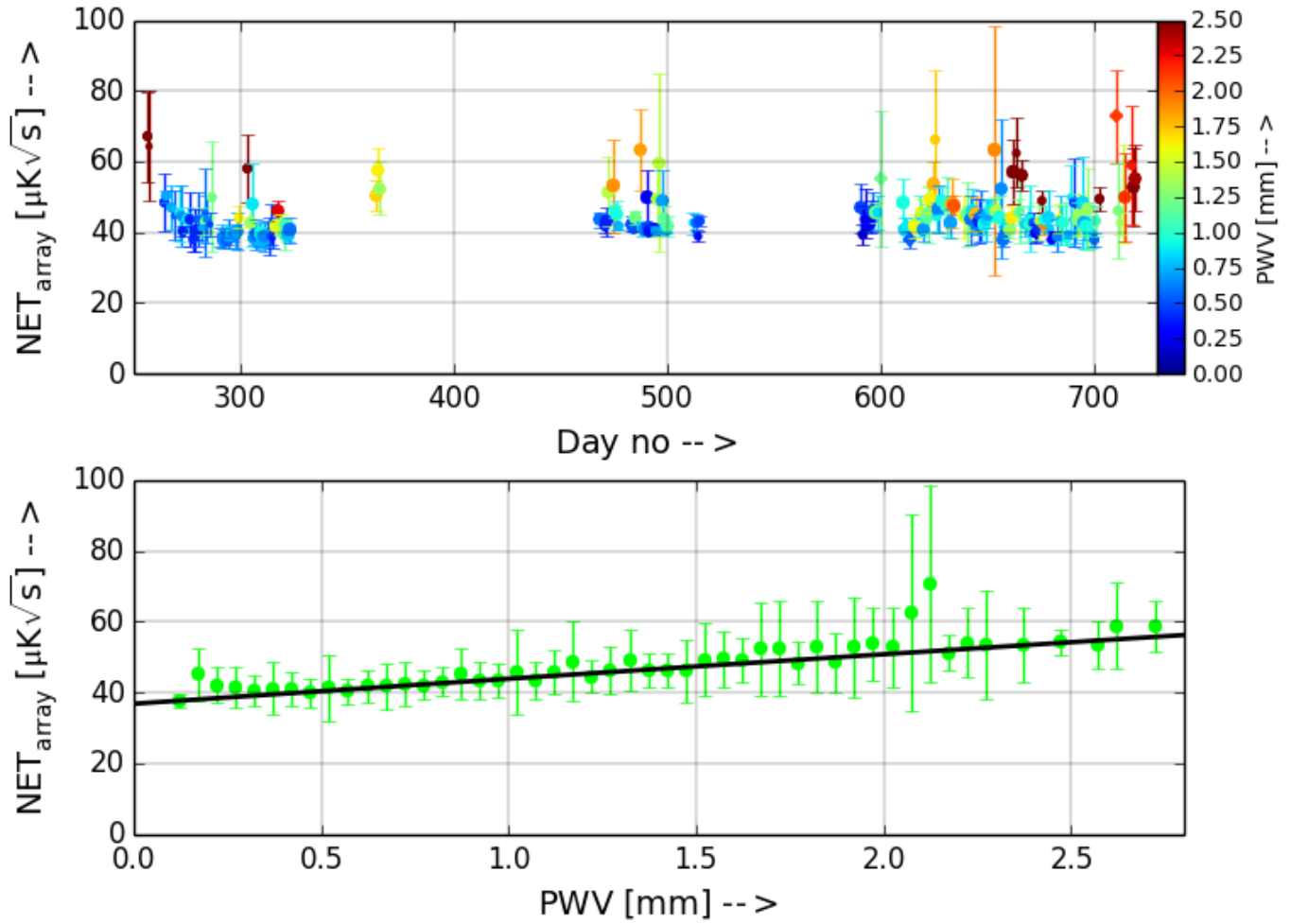


Figura 2.4: The values of the NET_{ABS} of the ABS detectors during the first, and second season of observations. The top panel shows the values for each observation day with the colour scale representing the average PWV level on the respective day. The observation day number ranges between 13 September, 2012 to 21 December, 2013. The bottom panel shows the NET_{ABS} as a function of the PWV level (bin-width = 0.05 mm). The black curve is a quadratic fit to the square of NET to account for the shot noise, and Dicke noise terms. The error bars in both panels correspond to the standard deviation in the particular bin.

$$P(f) = A^2 \left[1 + \left(\frac{f_{\text{knee}}}{f} \right)^\alpha \right]$$

where A corresponds to the amplitude of the white noise, the knee frequency f_{knee} , and the slope α characterises the $1/f$ noise (see section 4.1).

The NET of the detector is then $\text{NET}_{\text{det}} [\mu\text{K}\sqrt{\text{sec}}] = \frac{1}{\sqrt{2}} \times A [\mu\text{K}/\sqrt{\text{Hz}}]$. The median value of the ABS NET_{ABS} during the first two seasons is $43 \pm 6 \mu\text{K}\sqrt{\text{sec}}$. The top panel of FIG. 2.4 shows the NET_{ABS} values for the ABS detector array during the first, and second season of observations. The day numbers start from the 28 February, 2012 when the ABS telescope saw its first light. Thus, on the plot the first data point correspond to observations made during 13 September, 2012 and the last data point corresponds to 21 December, 2013. We ignored observations between February, and August 2012 when the ABS had a blackened baffle which introduced considerable optical loading. The error bars are the standard deviation of the NET_{ABS} values on a particular observation day. The colour bars show the average PWV level of the day. For all of the ABS work, the PWV values were obtained from the APEX telescope radiometer data. The possible systematics that might arise because of the PWV differences between the APEX, and the ABS site will be discussed in [12].

The bottom panel of FIG. 2.4 shows the NET_{ABS} as a function of the PWV level. The black curve is a quadratic fit to the square of NET to account for the shot noise, and Dicke noise terms. The decrease in sensitivity of the detectors with higher PWV, and increased optical loading is evident from the bottom panel. The large error bars for the worse PWV levels in the top panel also asserts this.

2.3. Observations

Between 2012 February and 2014 October (three seasons in total), we observed the selected CMB fields, point sources, and performed other calibration observations. The ABS targeted three sky patches on the southern sky for the CMB observations, and one patch for the galactic foreground study. Point sources *viz.* Moon, Jupiter, star forming H II region called RCW38, Taurus A (TauA), and Venus were observed to model the telescope pointing, beam, and the polarisation characterisation. Other calibration observations *viz.* the sky dips for detector responsivity and characterising the atmospheric loading; wide Moon scans for the array pointing; wire-grid (aligned, and rotating) for detector angle and responsivity measurements; Sun side-lobe scans for modelling the far side-lobe of the telescope; Fourier Transform Spectrometer (FTS) measurements for characterising the frequency response of the individual detectors were also regularly performed.

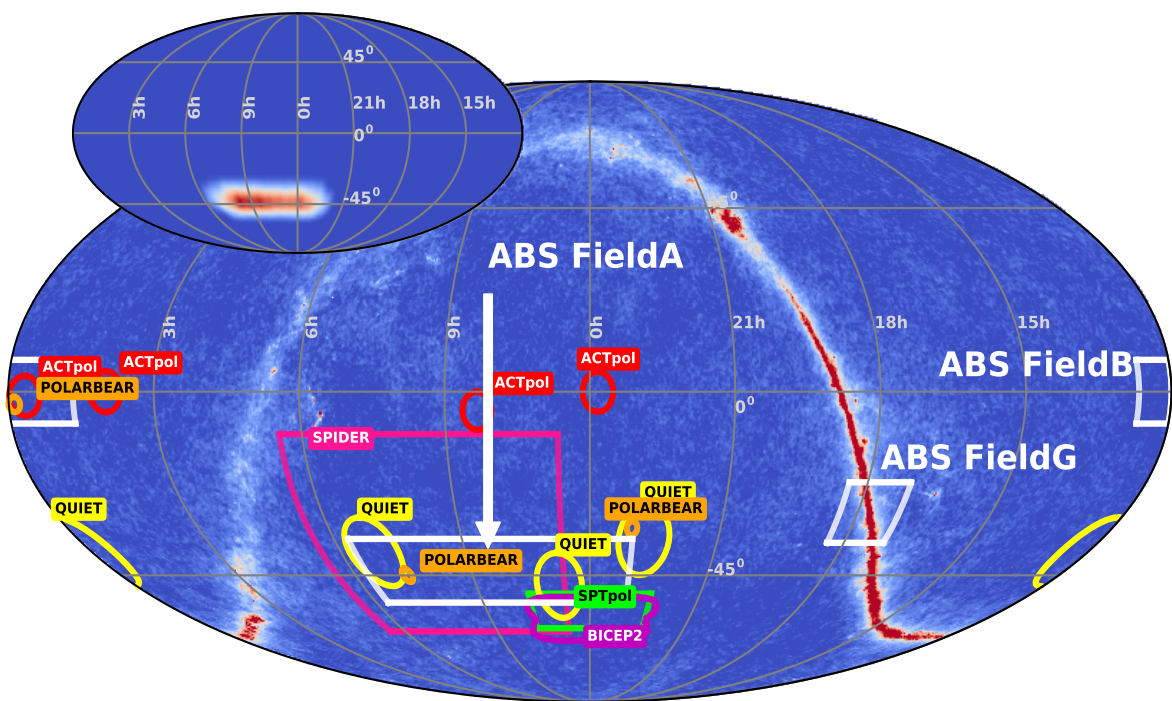


Figura 2.5: ABS observation fields (white) along with other CMB experiments (ACTpol, BICEP2, QUIET, POLARBEAR, SPIDER, and SPTpol) overlaid on the polarisation intensity map produced by the Planck HFI (143 GHz) instrument. The inset plot shows the weight map for ABS field-A. See table 2.3.1 and text for more details.

2.3.1. ABS scan fields

The ABS scan fields were defined by identifying regions of low foreground intensity from the Milky Way using the Finkbeiner, Davis & Schlegel (FDS) dust map [39]. The main patch field-A is ~ 2400 sq. degrees and centered at $(\text{RA}, \text{Decl.}) = (25^\circ, -42^\circ)$. The secondary patch (field-B) centered at $(\text{RA}, \text{Decl.}) = (175^\circ, 0^\circ)$ is ~ 700 sq. degrees. We also observed a galactic patch (field-G) for the characterisation of the polarised foreground emission from the Milky Way. The galactic patch is ~ 80 sq. degrees in size and centered at the galactic centre. Occasionally, when the Sun moved into field-B we observed field-C which is the same as the QUIET experiment's field-4 [41]. Most of the aspects of this work, however, are primarily from analysis of the data from the observations of field-A between 2012 September and 2013 December. More details about the ABS observations fields are listed in Table 2.3.1.

FIG. 2.5 shows the ABS scan fields (in transparent region) along with the observation fields of other CMB experiments overlaid on the all sky polarisation map (Stokes parameter I) using the Planck satellite mission's 143 GHz channel of the High Frequency Instrument (HFI) [44]. Note that this full sky polarisation map was only released in 2015. The figure also contains the coverage fields of other B-mode polarisation experiments *viz.* ACTpol [40], BICEP2 [26], QUIET [41], POLARBEAR [25], SPIDER [42], SPTpol [24]. The weight map for ABS field-A is also shown as an inset plot.

Table 2.2: Detail about the observation fields of the ABS experiment. The columns correspond to field name; field centre (RA, Dec.) in degrees; field widths in degrees; coverage area in square degrees; total observation hours; remarks about the field.

Field	R.A (α) [deg.]	Decl. (δ) [deg.]	$\Delta\alpha$ [deg.]	$\Delta\delta$ [deg.]	Area [deg 2]	Δt [hours]	Remarks
Field-A	25	-42	90	25	2400	1921	Main patch
Field-B	175	0	30	25	700	64	Secondary patch
Field-C	341	-36	25	10	250	239	Field-B sun avoidance
Field-G	266	-29	20	5	80	146	Galactic patch

2.3.2. Observing strategy and CMB observations

The field-A was given the top priority and was observed everyday when the patch became available around mid elevation of $\theta = 45^\circ$. Thus, it was observed in the east at azimuth $\phi = 125^\circ$ while rising and in the west at $\phi = 235^\circ$ while setting. The other CMB patches were observed when field-A was not available. The fridge cycle for the ABS telescope is 48 hours which includes 36 hours of uninterrupted observation followed by seven hours of He recycle. The He recycle time was carefully chosen to not overlap with the observations of our main patch field-A. The point source and other calibration observations sometimes superseded the observations of other CMB fields.

The scans were predominantly azimuthal scans at constant elevation except when performing the sky dips (or elevation nods as it is commonly called) primarily to calibrate the

detector responsity but also to model the atmospheric loading. Since the atmospheric loading changes widely in the elevation direction, constant elevation scans are normally adopted for the CMB observations.

The adopted scan speed was 0.75° per second with a scan amplitude of 10° . The scan amplitude was changed to 20° during the third season. Since a point on the sky moves by 15° every hour and it is not possible to cover the entire CMB field with a single scan, we staggered the CMB fields with sub fields. The telescope was thus repointed every hour to observe a new sub field and this one hour observation is called a constant-elevation scan (CES). A sky dip was performed before each CES. The large field of view of ABS ($\sim 22^\circ$) allowed all the detectors to capture an entire sub field. Note that the staggering also allows a given sky pixel to be observed in many different scan directions making the scan pattern quite messy and reducing the noise correlation between two widely separated pixels on the sky [29].

2.3.3. Point source observations

We observed point sources *viz.* Moon, Jupiter, Venus, and a star forming H II region called RCW38 for deriving the *pointing model of the telescope*. The Jupiter, and Venus observations were also used for the *beam modelling*. The Moon observations were almost always saturated and hence not used for the beam modelling. This saturation, however, caused only minimal error on the pointing calibration. The polarised supernovae remnant in the Crab nebula called TauA was observed for *characterising the polarisation properties of the detectors*.

The azimuthal scan amplitude adopted for point source observations was 10 degrees. The scan technique was to centre the source on the detector column containing the desired detector and the telescope base scans 10 degrees peak-peak in azimuth while the source drifts across. The duration of a single point source observation was 40 minutes on average and depended on the motion of the source in elevation during observation to capture the source with many feeds from a single pod. For this purpose, the duration was occasionally extended to 55 minutes for Jupiter, and TauA scans. During the first season, many point source observations were targeted on the column 23 (c23rxx) detectors (see FIG. 2.6). The detectors on this pod were chosen as reference only because they lie close to the telescope bore-sight, and are part of the batch-A detectors that had better characterised bandpass during the first season. Among others in this detector column, the detectors c23r00, c23r11 were predominantly used as reference detectors. FIG. 2.6 shows the number of targeted point source observations on different detector columns during the first two seasons.

An automatic point source observation (APSE) script was run to identify the sources that would become available on different detectors at any given point of time. The output for a particular source will be the name of the detector and the time at which the source would be available for that detector. The script was robust, and had the following functionalities incorporated

- to ignore listing the scans that can take the telescope to within 35° from the Sun.
- to set limits on azimuth, and elevation positions of the potential observations to ensure

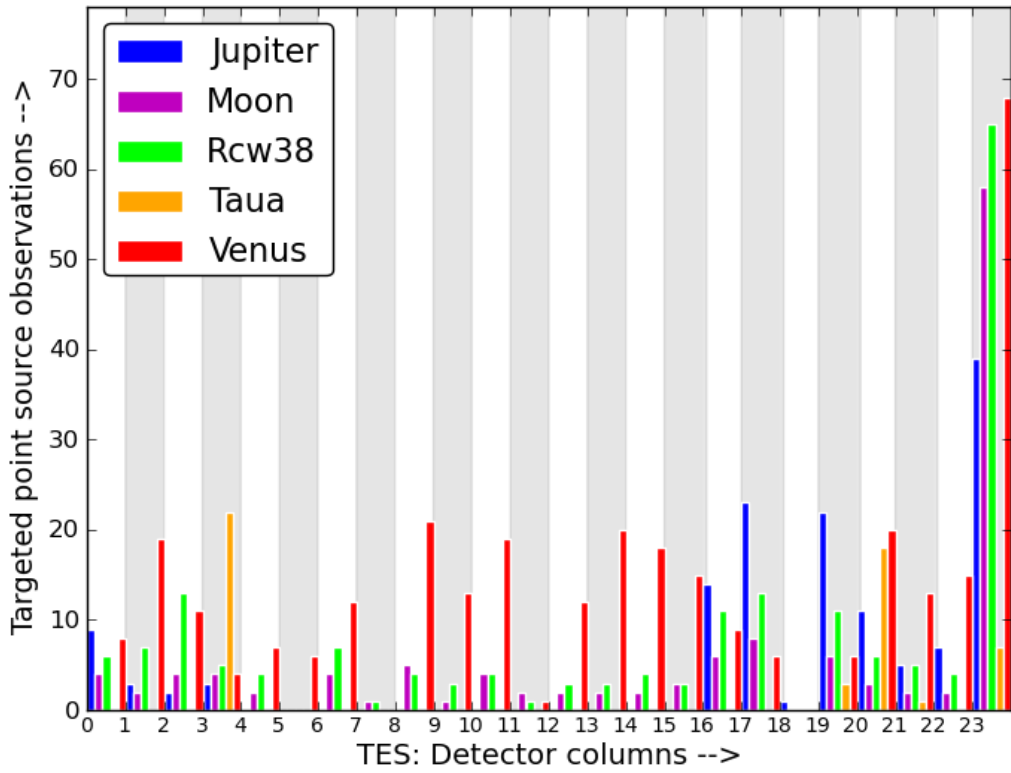


Figura 2.6: The number of targeted point source observations on detectors from different detector columns on the ABS focal-plane. The reference column c23rxx contains more targeted observations as compared to others.

that the telescope stays within the safe zone² of observation.

- to set limits on minimum elevation motion of a source during a particular observation. This is to get the source in many detectors in the targeted column as described above.
- to prioritise the CMB fields over point sources (i.e;) the potential point source scans when CMB fieldA was available for observation were ignored from being listed.
- to prioritise the detector list based on the number of observations on that particular column using information from the database.

2.4. Data Acquisition and storage

Based on the strategies described above, we generated schedule files containing both CMB, and the calibration observations. The schedule generation was generally automatic with minimal manual intervention to include cooling cycle, and the point source observations based

²Two azimuth limit switches prevent the telescope from going to positions that could be wrap and damage the cryogenic hoses and electronic cables.

on the output from APSE script described in section 2.3.3. The script to generate schedules was written by Akito Kusaka, and Lucas Parker. A typical ABS observation schedule lasts for 36 hours starting with CMB field-A observation followed by other CMB fields (or) calibration observation, and ending with the cooling cycle. An automatic telescope base monitoring script constantly (every 10 minutes) checks the telescope base during observations and triggers emails if a problem is encountered.

The schedule contain statements for creating a new housekeeping data file to store information, setting up the focal-plane temperature, detector biasing, moving the telescope to the desired location on the sky, observing, perform skydips, and recycle. An example is shown in the below box.

```

##AK_LINE:2014-09-21:00:06 1411257960 2014-09-21:06:11 1411279860 129
46 FieldAs11 FieldAs21 - Start of a CMB (staggered sub) field-A scan

new_hk_dirfile - Recording new housekeeping data file
delay, 5, seconds - Buffer time
servo_3he, 0.315 - servo to set focal-plane temperature
go_to_az_el, 129.000, 46.000 - desired azimuth, and elevation location
delay, 40, seconds - Buffer time in case of a delay/failure in performing the above
commands
setup_auto_setup, 20.000, 0.750 - detector biasing
setup_detectors - detector biasing
delay, 20, seconds
wait_until_utc, 2014, 9, 21, 0, 5 - Wait until actual start of observation
observe, 15, 60000, 20.00, 0.750, [schedule_group_name, '20140921_CMB_1',
scan_target, 'As11-As21'] - Observing CMB field for ~6 hours.

.....
.....
##AK_LINE:2014-09-21:13:10 1411305000 2014-09-21:13:40 1411306800
21.5 64.8 CALIBRATION Moon,tes:c17r11,az_el:27.1_55.1,offset
:-3.2_9.6,scan_spec:smooth_10_0.75,comments:None - Start of a Moon scan
for pointing calibration with detector c17r11
.....
go_to_az_el, 21.500, 64.800 - desired azimuth, and elevation location
delay, 40, seconds
setup_auto_setup, 10.000, 0.750
setup_detectors
delay, 20, seconds
wait_until_utc, 2014, 9, 21, 13, 9
observe, 6, 60000, 10.00, 0.750, [az_el, '27.1_55.1', scan_target,
'Moon', comments, 'None', schedule_group_name, '20140921_calib_2_1_Moon',
scan_spec, 'smooth_10_0.75', offset, '-3.2_9.6', tes, 'c17r11'] - Observing
Moon for 30 minutes
.....
##END_OBS

```

```

##begin recycle - Start recycle. We always performed a sky dip before recycling
new_hk_dirfile
go_to_az_el, 180.000, 55.000 - desired azimuth, and elevation location
.....
sky_dip, 5.000000, 30000, [schedule_group_name, '20140922_CMB_1_sky_dip',
amplitude, 5]- Perform sky dip
.....
recycle - Recycling takes ~7 hours.
wait_until_utc, 2014, 09, 22, 23, 55

```

The entire observation, and the data acquisition processes were handled by a program called `bolivar` written in `erlang` programming language. `bolivar` also handles the job of synchronising the data coming from multichannel electronics (MCE) system, housekeeping information, and the telescope motion control using a master clock. Please refer to [46] for a comprehensive reading about the ABS observation scheduling, `bolivar`, and `erlang` scripts.

The data from each detector was sampled at 200 Hz and stored as a 5-minutes long time-ordered data (TOD) in binary formatted dirfiles. Some of the housekeeping data were sampled at 100 Hz to reduce data storage. The basic information about all the observations were stored in a `mysql` database. Each CES is given an unique identification number in the database with which individual observations are later identified for data analysis purposes. The CMB scans normally lasts for more than six hours, and all of these were later grouped under a master schedule id number. The point sources observations were normally 40 minutes long. The filenames of an hour long CMB scan would be `YYYYMMDD/unixtime_dirfile.000` through to `YYYYMMDD/unixtime_dirfile.012`.

We used two computers at the site for telescope control, and the data storage. The data were regularly transferred everyday from the computers at the site to another computer at San Pedro de Atacama (SPdA) in Chile for low-level data analysis. The data were transferred to another computer at Princeton on a monthly basis for calibration, and more rigorous data analysis. All of the data at the Princeton computer were compressed without any loss of information into zip files for a better storage efficiency by Mike Nolta. We used the Sci-net General Purpose Cluster (GPC) [45] for CMB map-making and other high-level data analysis. Another `mysql` database (*abs offline*) was used at the Princeton computer and it contained detailed information about all the calibration, and data analysis processes to reduce redundancies of the analysis scripts. The analysis pipeline uses information from this database.

2.5. HWP modulation and demodulation

As mentioned earlier, ABS is the first ground-based experiment to successfully deploy a rapidly rotating warm HWP which modulates the linear polarisation of the incoming CMB photon. The raw timestream from each TES detector, because of the modulation by the HWP,

contains three-fold information corresponding to the intensity (I) and the two polarisation Stokes parameters (Q , and U). A set of demodulated timestreams comprise the basic unit of our data, and are commonly used in the calibration and CMB pipeline analyses described in the following sections. The ABS HWP rotates at $f = 2.55$ Hz modulating the incoming light at $2f$, which is detected in the detectors at $4f$. The use of HWP (4f component), suppresses the atmospheric $1/f$ noise without the need for pair differencing. In addition to this, the $2f$ component of the HWP modulated signal is used as a calibration source for checking the detector biasing and constantly monitoring their responsivities.

An HWP modulated time stream d_m can be described as

$$d_m = I + \operatorname{Re} [m(\chi)(Q + iU)] + \sigma_w + A(\chi) \quad (2.2)$$

where I , Q , and U represent the Stokes parameters of the incoming polarisation, $m(\chi)$ characterises the modulation function that is dependent on the rotation frequency of the HWP, σ_w is the detector white noise component, and χ is the angle between the frame of reference of the local polarisation and the principal axis of the HWP. The last term $A(\chi)$ receives contributions from the emissivity of the HWP $A_0(\chi)$ that is independent of the sky signal, and the HWP synchronous unpolarised sky signal $A_1(\chi)$. The emissivity component $A_0(\chi)$ can be thought of as a constant DC voltage added to the modulated signal which is removed by binning the TOD using the HWP encoder values. For demodulation, the modulated signal is multiplied by the complex conjugate of the modulation function $\bar{m}(\chi) = \exp(i4\chi)$ and the essential Q , and U Stokes parameters form the real and imaginary parts of the demodulated timestream. A detailed description of the demodulation technique and the HWP systematics are described in [48, 49].

$$d_d = \exp(i4\chi) d_m \quad (2.3)$$

$$= \exp(i4\chi) [I + \sigma_w + Q\cos 4\chi + U\sin 4\chi] \quad (2.4)$$

$$= \sigma_w^{\text{Re}} + \sigma_w^{\text{Im}} + \frac{1}{2}(Q + iU) + \frac{1}{2}\cos 8\chi (Q - iU) + \cos 4\chi \sin 4\chi (U + iQ) \quad (2.5)$$

$$= \sigma_w^{\text{Re}} + \sigma_w^{\text{Im}} + \frac{1}{2}(Q + iU) + \frac{1}{2}(Q - iU) \exp(i8\chi) + I \exp(i4\chi) \quad (2.6)$$

$$= \exp(i4\chi) (I + \sigma_{\text{det}} + \sigma_{\text{atm}} + \operatorname{Re} [m(\chi)(Q + iU)]) \quad (2.7)$$

where the third step assumes that the HWP DC component is already removed, σ_w^{Re} and σ_w^{Im} are the real and imaginary parts of the operation $\sigma_w * \exp(i4\chi)$ respectively. The final demodulated timestream EQ.(2.8) is obtained by lowpass filtering to remove all terms dependent on $\exp(i4\chi)$ and $\exp(i8\chi)$. FIG. 2.7 shows an example of the performance of ABS HWP in removing the unpolarised large atmospheric signal in the demodulated timestreams. The top panels shows the original timestream in μK , and the power spectrum. The blocked feature of the timestream is a clear indication of the $1/f$ noise. This is in fact extremely clear from the power spectrum in the right panel where the f_{knee} is around 2 Hz. The bottom panels show the demodulated timestreams in the left panel, and their power spectrum in the right panel. The green, and magenta lines correspond to the Q , and U parameters. The drop in the f_{knee} in the demodulated timestreams is evident. The top right panel also shows the bump near the scan frequency $f_{\text{scan}} = 0.04$, $f_{\text{HWP}} = 2.55$, and $2f_{\text{HWP}} = 5.1$ Hz. The scan

frequency bump is also present in the power spectrum of the demodulated data but the HWP harmonics are absent because of the low-pass filtering around at cut-off frequency of 2 Hz.

$$d_d = \sigma_w^{Re} + \sigma_w^{Im} + \frac{1}{2}(Q + iU) \quad (2.8)$$

The Q, and U Stokes parameters can now be extracted from the real and imaginary parts of the demodulated timestream (EQ. 2.8).

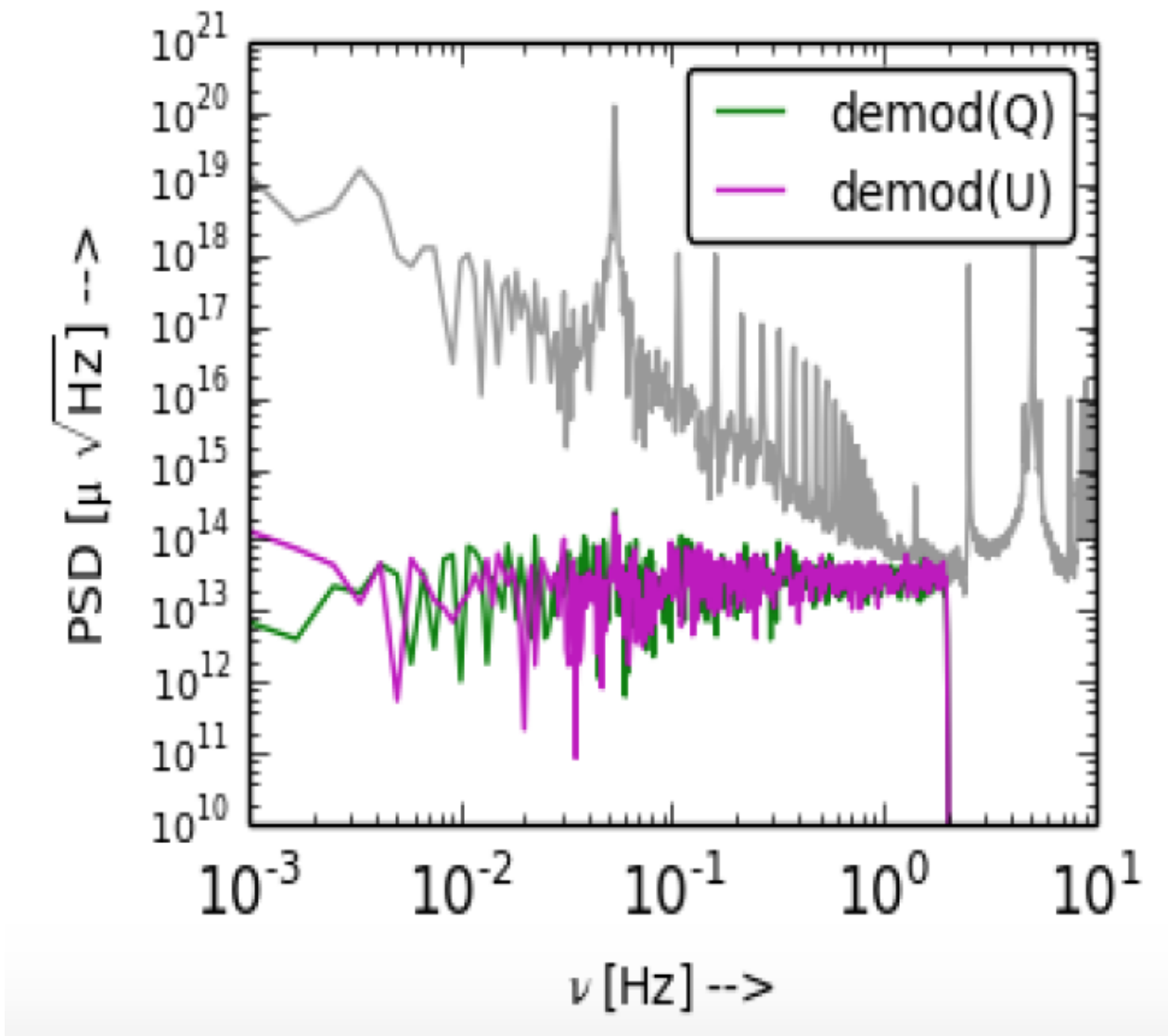


Figura 2.7: The original (top left), and the demodulated streams (bottom left) along with their power spectrum in the right panels. The black, green, and magenta lines correspond to original timestream, and Q , U Stokes parameters. The $1/f$ noise is evident in the original timestream - note the f_{knee} around 2 Hz in the top right panel. The HWP demodulation eliminates much of the unpolarised atmospheric signal and shifts the f_{knee} towards lower frequencies for the demodulated timestreams (bottom right panel). Also present in the power spectrum are the bump near the scan frequency $f_{scan} = 0.04$ Hz, and near the HWP 1f, 2f = 2.55, and 5.1 Hz. The demodulated timestreams are low-pass filtered with $f_{cut-off} = 2$ Hz.

Capítulo 3

CALIBRATING ABS TELESCOPE

Overview, and goals:

In this section, I will explain the procedure adopted to calibrate, and characterise different components of the ABS telescope. This is a critical step to correctly extract the cosmological information from the small CMB polarisation signals that are imposed on undesired large unpolarised signals. My prime contributions to ABS calibration are to

- model the telescope boresight pointing using point source observations.
- model the relative detector pointing of all detectors on the ABS focal-plane using wide Moon observations.
- characterise the telescope beam.
- capture TauA with short and tight scans using exact real-time pointing calculation.

This section also contains brief review about other necessary calibrations *viz.* measuring the telescope bandpass, detector time constants, and the polarization angle of detectors.

3.1. Telescope pointing

One of the key requirements for astronomical observations is to determine the telescope pointing accurately. Vectorially, the telescope pointing can be represented as a “boresight vector” \vec{b} EQ. (3.1) being projected from the telescope onto a desired point on the sky.

$$\vec{b} = \cos\phi \cos\theta \hat{x} + \sin\phi \cos\theta \hat{y} + \sin\theta \hat{z} \quad (3.1)$$

Given a point “p” on the sky, one could project \vec{p} perpendicularly onto a reference plane (observer’s local horizon). The azimuthal angle ϕ is then defined as the angle between \vec{p} and a reference vector (pointing north) around the horizon. Thus, the azimuthal angle increases from north ($\phi = 0^\circ$) easterly ($\phi = 90^\circ$) tracing a full circle with $\phi = 180^\circ$ at south and $\phi = 270^\circ$ at west.

Name	Coordinates	Method	Remarks	Author
M1	instrument	χ^2 TOD fitting	Moon, Jupiter maps for pointing model	JLS
M2	equatorial	ML	RCW38, Venus maps	JLS
M3	instrument	simple flat-sky projections	Beam modelling, and systematic checks	AK
M4	instrument	simple flat-sky projections	only for systematic checks	SR
M5	equatorial	maps in CEA ¹ projections	wide Moon scan map	JLS

Tabla 3.1: Different mapping algorithms for ABS point source observations. The instrument coordinates refer to $(\phi_{tel} - \phi_{obj}) \cos(\theta_{tel}), \theta_{tel} - \theta_{obj}$, ML refers to Maximum-Likelihood approach and was adopted to map faint sources namely RCW38, and Venus. The maps M1, M3, and M4 are simple projections of the TOD onto the map space using flat sky approximation.

The elevation angle (or) altitude θ is the angle between the horizon (reference plane) and the observers line-of-sight point to “p”. It is measured from horizon $\theta = 0^\circ$ towards the zenith $\theta = 90^\circ$. Since this coordinate system uses the observer’s local horizon as the reference plane, it is called the “horizon coordinate system”.

Unlike any other single-dish telescope, ABS consists of an array of 480 detectors and hence the pointing solution has been decomposed into

- Absolute boresight pointing of the telescope: to determine the overall telescope pointing.
- Relative focal-plane pointing between detectors in the array - to determine the pointing of each of the detectors on the ABS focal-plane.

3.1.1. ABS boresight pointing - Method

Any telescope is generally equipped with encoders that record the azimuth, elevation, and observation time of the telescope. If the telescope points towards point “p”, in an ideal world with no imperfections, the error associated with this pointing will be zero.

$$\Delta\phi = \phi_p - \phi_{enc} = 0 \quad (3.2)$$

$$\Delta\theta = \theta_p - \theta_{enc} = 0 \quad (3.3)$$

In reality, however, the encoder values tend to be erroneous. The situation is exacerbated when the encoder pointing offsets tend to be a function of the direction of telescope pointing, and time of observation. These could be due to the structural imperfections on the telescope *viz.* axis tilt, zero point error, gravitational sag to name some. The prime goal of this study is to understand these systematic errors and counteract them. The encoder values must be corrected once a satisfactory pointing model is obtained such that the residual offsets are minimal and random distributed.

This can be achieved by observing several bright point sources and comparing the encoder positions with the known catalogue positions of the sources. For ABS, we used the Moon, Jupiter, RCW38, and Venus observations. The map making algorithm employed are listed in TAB. 3.1.1. The M1, and M2 techniques are adopted for the boresight pointing solution.

FIG. 3.1 shows the azimuth and elevation offsets as a function of the telescope position from first and second season point source observations. The M1 mapping algorithm was used for this purpose. The circles are Moon, stars are Jupiter, and triangles are Venus observations respectively. The offsets are not randomly distributed and the presence of systematic errors are evident.

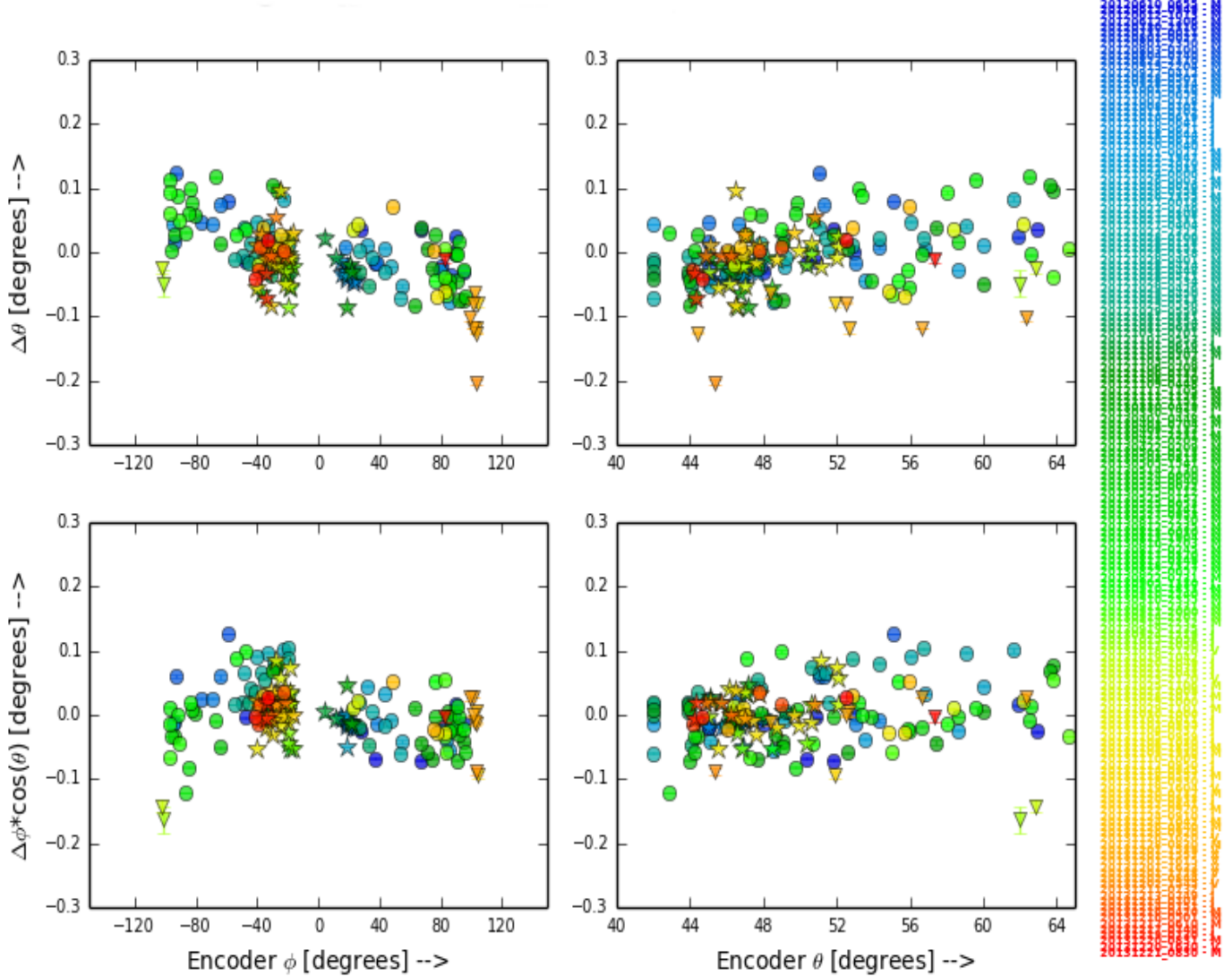


Figura 3.1: ABS original encoder offsets showing the systematics errors. Top panel shows the elevation encoder offsets $\Delta\theta$ as a function of azimuth (left) and elevation (right). Bottom panel shows the how the azimuth encoder offsets $\Delta\phi \cos(\theta)$ are affected at different azimuth (left) and elevation (right) positions. Circles are Moon, stars are Jupiter, and diamonds are Venus observations respectively. The spectral colours on the plot serve as a proxy for the observation date (although not in a linear scale) with red being the most recent observation.

Parameter	Description	v0 [radians]	v1 [radians]
$\Delta\theta = \text{ELS1} * \theta + \text{ELS2}$	Elevation skew, gravitational sag	ELS1=0.00358 ELS2=-0.0028	ELS1=0.00378 ELS2=-0.0032
$\Delta\theta \propto \text{ELZ}$	Elevation encoder zero point	3.766e-04	1.731e-044
$\Delta\phi \propto \text{IA} * \cos\theta$	Azimuth encoder zero point	-8.241e-03	-2.105e-03
$\Delta\phi \propto \text{NOAO} * \sin\theta$	Non-orthogonality between Az, and El axis	1.741e-03	1.383e-03
$\Delta\theta \propto \text{AN} * \cos(\phi)$ $\Delta\phi \propto \text{AN} * -\sin(\phi) * \sin(\theta)$	Azimuth axis tilted towards north	-4.846e-04	-3.389e-04
$\Delta\theta \propto \text{AE} * \sin(\phi)$ $\Delta\phi \propto \text{AE} * \cos(\phi) * \sin(\theta)$	Azimuth axis tilted towards east	-6.033e-04	-6.855e-04

Tabla 3.2: ABS six parameter pointing model derived using Moon, Jupiter, and Venus observations from the first, and second seasons as shown is FIG. 3.1.

3.1.2. Pointing model v0 and v1

The initial versions of the ABS boresight pointing solution was a six parameter model shown in TAB. 3.1.2 accounting for the structural flaws in the telescope to nullify the systematic errors evident from FIG. 3.1. The functional forms were modelled as linear combinations of trigonometric functions to fit the encoder offsets. The first version of ABS pointing model (v0) was derived using the Moon, and Jupiter data from the first season. The pointing model was included into the analysis pipeline as a python function. Given the azimuth, elevation, and time of observation, the pointing model will return the corrected encoder values. This model was later updated to v0_1 to correct for the nine degree azimuth encoder slip that occurred during August 2012 (see section 4.2) although note that the parameter values remained the same.

The extension of v0_1 to v1 using similar modelling techniques was obtained after including data from the second season. There were more encoder slips in the second season, and the model v1 takes all of them into account. The parameter values for v0, and v1 can be found in TAB. 3.1.2.

3.1.3. Pointing model v2 - The Euler rotation pointing model

This section discusses about the extension of the simple pointing models v0 and v1 to a more sophisticated model v2 using *Euler rotations*. This model also uses the observations of Moon, Jupiter, and Venus from FIG. 3.1. This pointing model also contains six parameters (see TAB. 3.1.3) to model the structural imperfections. Before going into the process of Euler rotations, note from the figure that there are no observations in the azimuth west direction. The maps of RCW38 made using the M2 mapper (both individual and stacked) were used to characterise the ABS telescope pointing in the west. The SNR of the RCW38 observations was poor leaving us with only three satisfactory observations in the west. Because of the large uncertainties in the RCW38 fitting, the pointing model parameters was not very sensitive to the inclusion of RCW38 data. We will revisit the ABS pointing in the west direction in section 3.1.4.

The three components of the telescope pointing vector \vec{p} in cartesian coordinates are

Parameter	Description	v2 [radians] [rad]
AZZ	Az. encoder zero error	-0.0028
ELZ	El. encoder zero error	-0.0027
ELS	El. encoder slope	0.0036
AZT	Az. tilt direction	1.0379
AZTM	Az. tilt magnitude	0.0010
NOAE	Non-orthogonality between Az, and El axis	-0.0023

Tabla 3.3: Euler pointing model v2 derived using Moon, Jupiter, and Venus observations.

$$\begin{aligned}\vec{p}_x &= \cos(-\phi)\sin(90 - \theta) = \cos\phi \cos\theta \\ \vec{p}_y &= \sin(-\phi)\sin(90 - \theta) = -\sin\phi \cos\theta \\ \vec{p}_z &= \cos(90 - \theta) = \sin\theta\end{aligned}$$

The goal here is to correct the angles ϕ, θ to reduce the pointing offsets as described earlier but now using *Euler rotations*. For a single pointing model parameter, the Euler rotation matrix can be defined by a combination of three successive rotations through the angels α, β , and γ which are commonly called the *Euler angles*. The key now is find the Euler angles (and the corresponding rotation matrices) for each of the pointing model parameter. The final rotation matrix R_{v2} will compose a series of successive rotations obtained for each of the model parameter. We perform *extrinsic Euler rotations* where the rotations are with respect to the axes of the fixed original coordinate system in the ZYZ^2 sequence [52]. In case of *intrinsic* Euler rotation in ZYZ sequence, the first rotation is by an angle α about the z -axis. The new basis is now x', y', z' . The next rotation is about the new x' -axis by an angle β followed by a final rotation by angle γ about the second intermediate z'' -axis. For *intrinsic* rotations, the rotations are by angle γ about z -axis, then by β about y -axis and finally by angle α about z -axis again.

To understand this better, consider vector \vec{v} with $(az, el) = \phi, \theta$. We now want to correct the elevation θ by an amount $\delta\theta$ while the azimuth ϕ must remain unchanged. To do this,

- first rotate \vec{v} by an amount $\gamma = -\phi$ about z -axis. This will align \vec{v} with the North $\phi = 0$ degrees.
- then correct θ by $\beta = \delta\theta$ about the y -axis. Note that, since \vec{v} is now aligned with the north, any rotation in θ will only affect elevation and not the azimuth.
- The vector \vec{v} should finally be moved back with the rotation $\alpha = \phi$ about the z -axis.

Euler angles and rotation matrices for model parameters

Before proceeding we convert all azimuth and elevations values from degrees to radians. The corrections for azimuth, and elevation encoder zero point errors are just linear equations

²<http://mathworld.wolfram.com/EulerAngles.html>

and parameters are

$$\phi = \phi + AZZ \quad (3.4)$$

$$\theta = \theta + ELZ \quad (3.5)$$

Elevation skew

The next correction is the skew in the elevation which is modelled as a first degree polynomial in $v0$ model. Since the intercept (ELZ) have already been included above, we only consider the slope $ELS * \theta$. The corresponding Euler angles and rotation matrix R_{ELS} to correct the elevation skew are

$$\begin{pmatrix} \alpha \\ \beta \\ \gamma \end{pmatrix} = \begin{pmatrix} -\phi \\ ELS * \theta \\ \phi \end{pmatrix} \quad (3.6)$$

Rotation matrix $R_{ELS} = BCD$ contains three matrices BCD which are rotations about z , y , and z axis by angles α , β , and γ respectively. Note that D is the first rotation and must not be interchanged as matrix multiplication is not commutative.

$$D = \begin{pmatrix} \cos\gamma & \sin\gamma & 0 \\ -\sin\gamma & \cos\gamma & 0 \\ 0 & 0 & 1 \end{pmatrix} C = \begin{pmatrix} \cos\beta & 0 & \sin\beta \\ 0 & 1 & 0 \\ -\sin\beta & 0 & \cos\beta \end{pmatrix} B = \begin{pmatrix} \cos\alpha & \sin\alpha & 0 \\ -\sin\alpha & \cos\alpha & 0 \\ 0 & 0 & 1 \end{pmatrix}$$

Azimuth tilt

The tilt in the azimuth axis is represented by the magnitude $AZTM$, and the direction AZT of the tilt. Earlier in $v0$, two parameters were used to represent the azimuth tilt towards the north, and east directions. The corresponding Euler angles to get the rotation matrix R_{AT} are

$$\begin{pmatrix} \alpha \\ \beta \\ \gamma \end{pmatrix} = \begin{pmatrix} AZT \\ AZTM \\ -AZT \end{pmatrix} \quad (3.7)$$

Non-Orthogonality of az and el axis

The R_{NOAE} to correct the non-orthogonality between the azimuth, and elevation axis can be obtained using

$$\begin{pmatrix} \alpha \\ \beta \\ \gamma \end{pmatrix} = \begin{pmatrix} -90. - \phi \\ NOAE \\ 90. + \phi \end{pmatrix} \quad (3.8)$$

Final rotation matrix

With all the above definitions, the final rotation matrix will be

$$R_{v2} = R_{NOAE} * R_{AT} * R_{ELS} \quad (3.9)$$

Note that the order of rotations is very important as the matrix multiplication does not commute. The order is based on the following corrections

- azimuth and elevation encoder zero point shifts
- elevation skew and sag
- azimuth tilt
- non-orthogonality of azimuth, and elevation axis

The equations from EQ. 3.4 through 3.8 constitute the parameters *Euler rotation pointing model v2*. Once the final rotation matrix R_{v2} is obtained, the corrected vector \vec{p}' will be

$$\vec{p}' = \begin{pmatrix} \vec{p}'_x \\ \vec{p}'_y \\ \vec{p}'_z \end{pmatrix} = \begin{pmatrix} R_{11} & R_{12} & R_{13} \\ R_{21} & R_{22} & R_{23} \\ R_{31} & R_{32} & R_{33} \end{pmatrix} \times \begin{pmatrix} \vec{p}_x \\ \vec{p}_y \\ \vec{p}_z \end{pmatrix} \quad (3.10)$$

and \vec{p}' can then be converted into spherical coordinates to obtain the correct encoder values.

$$\phi = \tan^{-1}\left(\frac{-\vec{p}'_y}{\vec{p}'_x}\right) \quad (3.11)$$

$$\theta = \tan^{-1}\left(\frac{\vec{p}'_z}{\sqrt{\vec{p}'_x^2 + \vec{p}'_y^2}}\right) \quad (3.12)$$

3.1.4. RCW38 observations and ABS pointing in the west

We used the RCW38 observations to characterise the boresight pointing in the west. This is of crucial importance since our main CMB field is observed everyday while rising at the east ($\phi = 125^\circ$) and while setting at the west ($\phi = 230^\circ$). There are plenty of observations (Moon, Jupiter) to satisfactorily model our pointing in the east but only RCW38 (and occasionally Venus) in the west.

The SNR of the RCW38 observations were generally poor to map them using M1 algorithm. Instead we used the M2 mapper which stacks all the observations from a single column to produce a stacked map in the equatorial coordinates using *Maximum likelihood (ML) approach*. The M2 maps were then converted into instrument coordinates using the time at which the object was closer to the detector. This approximation is valid for sources like Jupiter, RCW38, Venus as their positions in the equatorial coordinates remain fixed during

the course of an observation. We did not use M2 mapper for the bright Moon, and Jupiter observations as it performs rigorous high pass filtering which leads to large negative bowls around the sources. Occasionally, Venus maps were made using M2 mapper for consistency checks.

Despite having ~ 30 RCW38 observations, only three of them with a good SNR were considered for pointing model. Combing them with other weaker RCW38 observations did not improve the pointing model significantly because of the large uncertainties in the centroid fitting. Hence, the pointing model versions $v0, v1$, and $v2$ were implemented initially in the analysis pipeline without using RCW38 observations under the assumption that there is no special effect in the west.

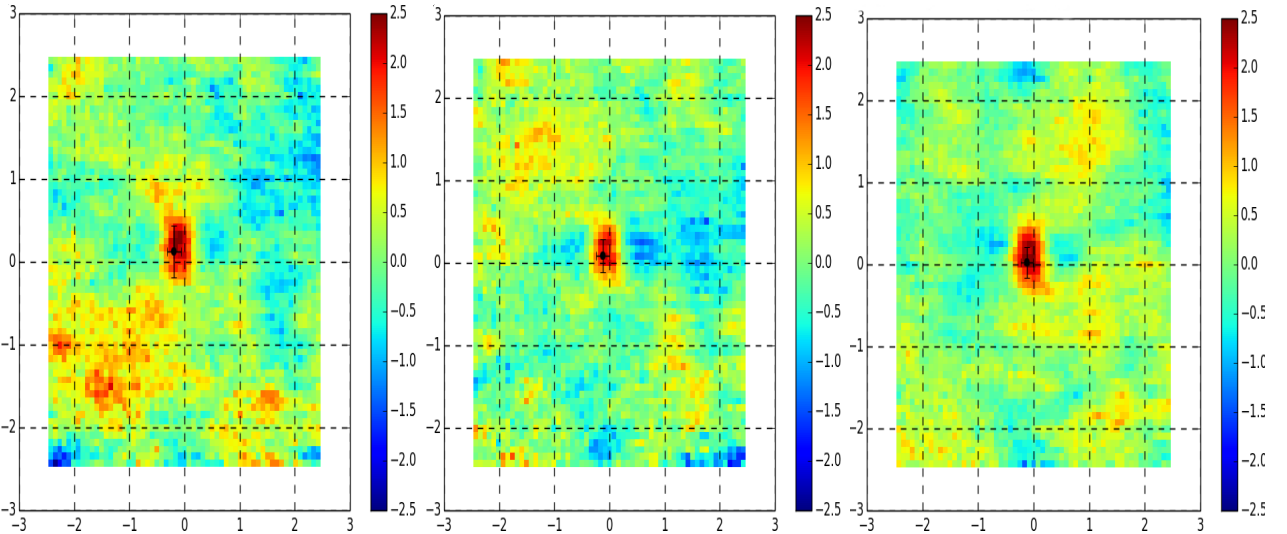


Figura 3.2: Stacked RCW38 maps observed in the azimuth west during the second observation season. The three panels correspond to the stacked maps before applying the pointing model (left panel), after applying pointing model $v0$ (middle panel), and the Euler rotation pointing model $v2$ (right panel). The pointing models does not correct the $\sim 0.13^\circ$ azimuth shift.

However, stacking the (three good) RCW38 observations after applying different pointing modes revealed an additional $\sim 0.13^\circ$ azimuth shift in the west. FIG. 3.2 shows the stacked RCW38 observations with no pointing model, $v0$ model, and $v2$ model respectively from left to right. It is clear that the pointing models does not work well in the west direction as the middle and right panel have the $\sim 0.13^\circ$ azimuth shift as in the left panel. This shift in the west direction was also confirmed independently using the ABS \times Planck TE maps. The TE power using the data from the azimuth east is larger than from the azimuth west. This shift was added to all observations with $\phi \geq 180$ degrees. The exact location to add this shift is not important as our CMB field-A scans were performed either at $\phi = 125^\circ$ (or) $\phi = 235^\circ$.

Encoder, and GPS issues

During the three seasons of observations, we had four instances of undesired large azimuth encoder slips. One of them was due to the azimuth encoder breakage during the third season.

There was also a period of \sim 12 days when the GPS stopped working. The azimuth encoder slips were almost always immediately identified and corrected resulting in minimal data loss. Section 4.2 discusses these two issues in detail.

The distribution of the pointing residuals after using Euler rotation pointing model v2 is shown in FIG. 3.3. The rms value of $\sigma_{\text{pointing}} = 0.04$ degrees will be used along with the FWHM of the ABS telescope beam (section 3.3.2) to compute the experimental beam function B_l . This is shown in FIG. 3.8 in the section 3.3. For simplicity, we model the effect of pointing residual on the B_l as given by EQ. 3.13. The green curve in FIG. 3.8 correspond to the beam window function $W_l = B_l^2$ for the ABS beam (simple Gaussian) $\sigma_{\text{ABS}} + \sigma_{\text{pointing}} = 34.9$ arcmins. The black curve in the figure is the actual ABS window function with a sophisticated beam modelling, and includes the pointing residuals in it. We checked the effects of lunar phases on our centroid and did not find any significant effect. The saturation of Moon coupled with the detector time response could lead to a small shift in the centroid values particularly if the response time is slow depending on the scan direction. This was checked for left, and right going scans. No significant shift in the centroid was discovered.

$$B_{\ell_{\text{pointing}}} = \exp \left[\frac{\ell(\ell+1)}{2\sigma_{\text{pointing}}^2} \right] \quad (3.13)$$

3.2. ABS focal-plane pointing

The previous section 3.1.1 described the methods to obtain the telescope boresight pointing model (i.e:) the corrections applied to the azimuth, and elevation encoders of the telescope based on a six parameter pointing model. The ABS telescope, however, consists of several detectors and the signals from all of them will be stacked to achieve the desired sensitivity. This requires us to know the pointing of all the detectors accurately. In this section I will cover the focal-plane pointing derived using seven wide Moon observations performed during the first two seasons. The maps were made using M5 algorithm (see 3.2 for definitions of different mapping algorithms) and are simple projections³ of the data on the sky in the equatorial coordinates. This focal-plane pointing model can precede the boresight pointing step. This is because the pointing of all the detectors on the focal-plane will be equally affected by any systematic error that depends on the position on the sky where the telescope is pointed.

3.2.1. Method

Given the angles ν, ω which represent the offset of a particular detector on the focal-plane in the azimuthal and elevation direction, we can write

$$\vec{d}_h = \cos\nu \cos\omega \hat{x} + \sin\nu \cos\omega \hat{y} + \sin\omega \hat{z} \quad (3.14)$$

$$\vec{d}_s = \cos\phi_{d_s} \cos\theta_{d_s} \hat{x} + \sin\phi_{d_s} \cos\theta_{d_s} \hat{y} + \sin\theta_{d_s} \hat{z} \quad (3.15)$$

³Since Moon is extremely bright, we need not use rigorous filtering techniques.

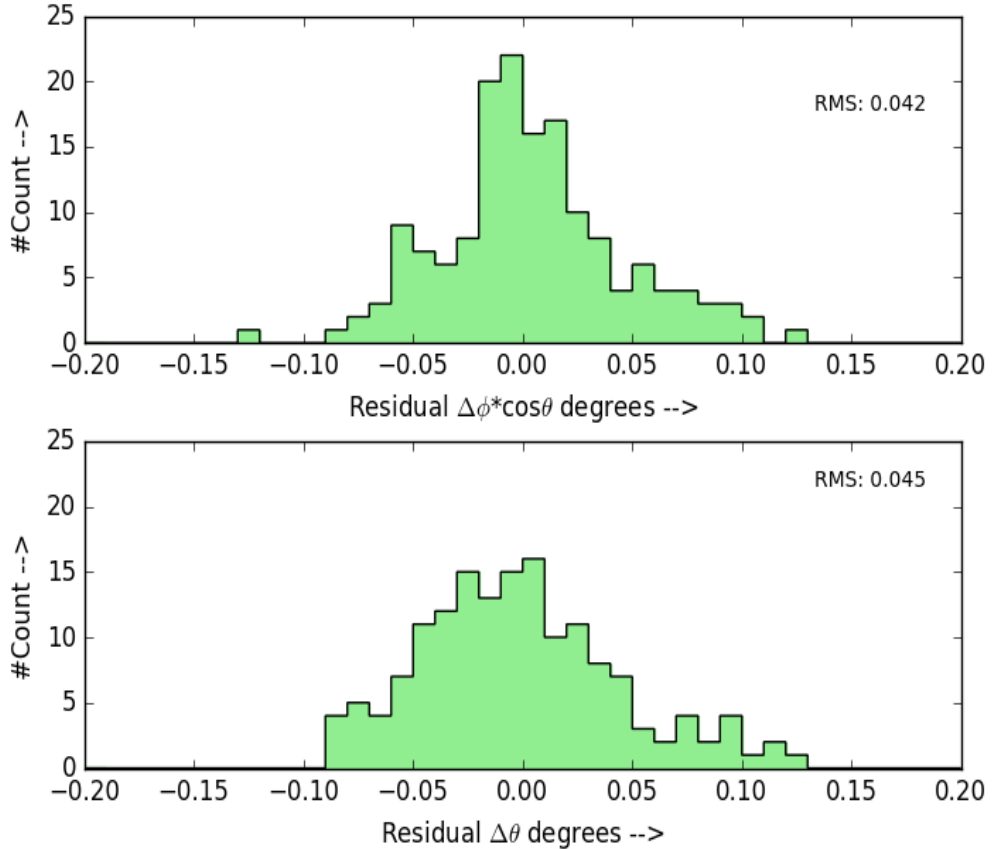


Figura 3.3: The final pointing residuals after performing the pointing offsets modelling using Euler rotations v2. The top, and bottom panels correspond to the azimuthal, and elevation residuals respectively.

where \vec{d}_h and \vec{d}_s describe the detector vectors at the horizon and the sky. The angles ϕ_{ds} , and θ_{ds} represent the azimuthal, and elevation angles of the detector on the sky. The known vector \vec{d}_h can be converted into the unknown vector \vec{d}_s using the azimuthal ϕ_s , and elevation θ_s angles of the telescope boresight on the sky obtained from the position encoders.

$$\vec{d}_s = R_{hs} * \vec{d}_h \quad (3.16)$$

R_{hs} can be decomposed further into

$$R1 = \begin{pmatrix} \cos\theta_s & 0 & -\sin\theta_s \\ 0 & 1 & 0 \\ \sin\theta_s & 0 & \cos\theta_s \end{pmatrix}, \text{ and } R2 = \begin{pmatrix} \cos\phi_s & \sin\phi_s & 0 \\ -\sin\phi_s & \cos\phi_s & 0 \\ 0 & 0 & 1 \end{pmatrix}$$

giving

$$R_{hs} = R2 * R1 = \begin{pmatrix} \cos\phi_s \cos\theta_s & \sin\phi_s & -\cos\phi_s \sin\theta_s \\ -\sin\phi_s \cos\theta_s & \cos\phi_s & -\sin\phi_s \cos\theta_s \\ \sin\theta_s & 0 & \cos\theta_s \end{pmatrix}$$

Thus, we obtain \vec{d}_s as

$$\vec{d}_s = \begin{pmatrix} \cos\phi_{ds} \cos\theta_{ds} \\ \sin\phi_{ds} \cos\theta_{ds} \\ \sin\theta_{ds} \end{pmatrix}$$

$$\vec{d}_s = \begin{pmatrix} \cos\phi_s \cos\theta_s & \sin\phi_s & -\cos\phi_s \sin\theta_s \\ -\sin\phi_s \cos\theta_s & \cos\phi_s & -\sin\phi_s \cos\theta_s \\ \sin\theta_s & 0 & \cos\theta_s \end{pmatrix} * \begin{pmatrix} \cos\nu \cos\omega \\ \sin\nu \cos\omega \\ \sin\omega \end{pmatrix} \quad (3.17)$$

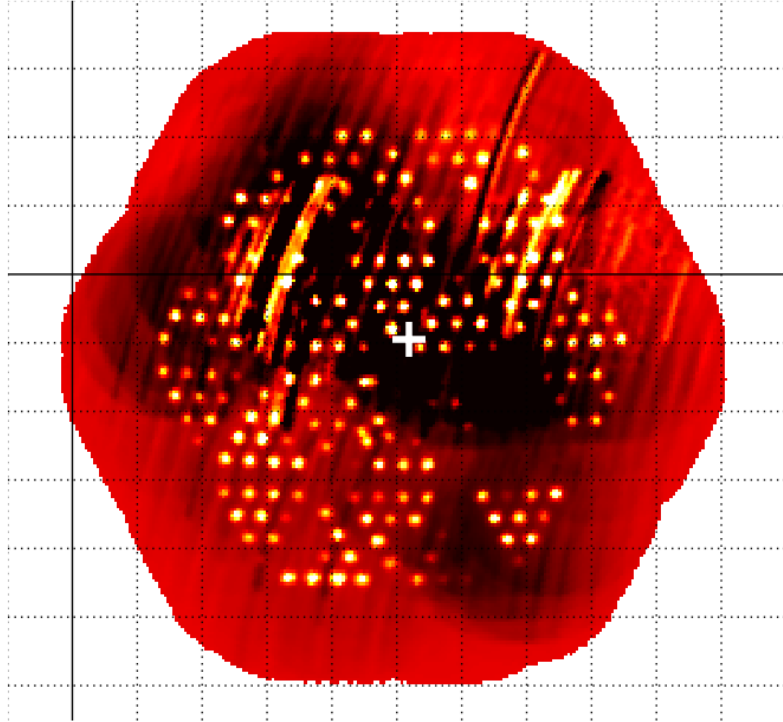


Figura 3.4: Moon maps from various detectors on the ABS focal-plane using a single wide Moon observation performed on August 1, 2012. The maps were originally made in equatorial coordinates using HEALPix Pixelization, and then shifted by 3x the detector positions for visualising the maps of on detectors on a single image. The scan centre ($\alpha, \delta = 308.1, -9.5$) degrees is marked with white plus symbol for reference.

Since, it is not practical to have several encoders to determine the \vec{d}_s for all detectors individually, it is important to know the angles ν , and ω of the detectors precisely to obtain their pointing on the sky. Having known the physical location of the detectors on the ABS focal-plane, it is possible to derive the two angles using geometric ray-tracing techniques. For ABS, we used the Diffraction Analysis of a Dual Reflector Antenna (DADRA) [50] software for this purpose before the deployment of the telescope in Chile. The main goals of this study are to 1. ensure that ν, ω determined using DADRA are accurate and not affected by any physical defects during the deployment, and 2. continuously monitor the angles for any seasonal variations *viz.* deformation of the focal-plane.

3.2.2. Wide Moon scans

The focal-plane pointing was derived using Moon observations. These are special observations in the sense that they lasted for ~ 140 minutes unlike other point source observations which were only 40 minutes on average. The azimuthal scan widths adopted for these observations were $\geq 40^\circ$, much larger than the normal scan widths. The reason for such long observations, and wide coverage is to capture the Moon on as many detectors as possible.

FIG. 3.4 shows an example of a single wide Moon scan performed during the first season. This map was made in equatorial coordinates using the *Hierarchical Equal Area isoLatitude Pixelization of a sphere* (HEALPix) [51] with a resolution 0.22° characterised by the $n_{\text{side}} = 256$. The angles ν, ω of the detectors have been stretched 3x times only to visualise the maps of all detectors on a single image.

3.2.3. Mapping, and detector pointing

For every wide Moon observation i , we first made the map of the reference⁴ detector m_{ref}^i using EQ. 3.17 where the detector positions $(\nu_{\text{ref}}, \omega_{\text{ref}})$ were obtained from the results of the DADRA software. Note that the angles ν, ω are defined in horizon coordinates. The pointing offsets of the reference detector are

$$\Delta\phi_i^{\text{ref}} = \phi_{\text{Moon}}^i - \phi_i^{\text{ref}} \quad (3.18)$$

$$\Delta\theta_i^{\text{ref}} = \theta_{\text{Moon}}^i - \theta_i^{\text{ref}} \quad (3.19)$$

Here, we convert the actual offsets in equatorial coordinates into horizon coordinates. This is only to simplify the process as ν, ω are actually defined in horizon coordinates. The above shift $(\Delta\phi_i^{\text{ref}}, \Delta\theta_i^{\text{ref}})$ was then added to make maps of all the detectors \tilde{m}^i where \sim symbol represents the maps with this additional shift.

The pointing offsets $\widetilde{\Delta\phi}_i, \widetilde{\Delta\theta}_i$ were calculated for all the detectors from \tilde{m}^i . Note that the offset of the reference detector will now be $(\widetilde{\Delta\phi}_i^{\text{ref}}, \widetilde{\Delta\theta}_i^{\text{ref}}) = (0, 0)$. Likewise, the offsets of others detectors will also be $(0, 0)$ within the error bars if ν, ω were determined precisely for all detectors.

This procedure was performed for all wide Moon observations, and a set of pointing offsets $\Delta\phi_i, \Delta\theta_i$ were collected for all the detectors. The desired shift $\Delta\nu, \Delta\omega$ in every detector position was determined as the average of the obtained pointing offsets using EQ. 3.21

⁴The TES detector c23r00 was chosen as the reference detector only because it is close to the telescope boresight, and would not suffer from any small approximations in pointing calculation

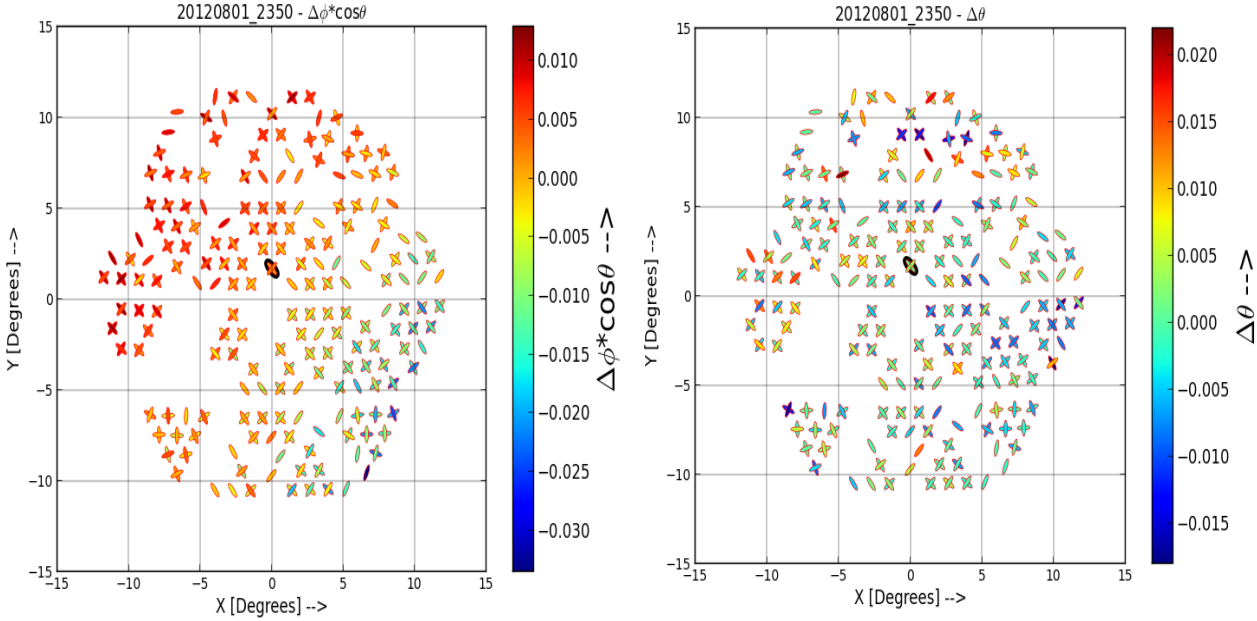


Figura 3.5: The offsets $\Delta\phi\cos(\theta)$ (left), and $\Delta\theta$ (right) in degrees for all the detectors on the ABS focal-plane for the Moon observation on 1 August, 2012. The coverage was exceptional and the gaps in the plot are because of the dark (or) bad detectors. The reference detector c23r00 near the centre of the focal-plane is marked with a black outline. An extremely small gradient can be seen in the $\Delta\phi\cos(\theta)$ offsets in the left panel. We decided to ignore the gradients after verifying the gradient levels of several observations. The gradients does not correspond to systematic effects due to the motion of Moon during the scan, and detector response time.

$$\Delta\nu^{C_{xx}R_{xx}} = \frac{\sum_{i=1}^n w_i \widetilde{\Delta\phi_i^{C_{xx}R_{xx}}}}{\sum_{i=1}^n w_i} \quad (3.20)$$

$$\Delta\omega^{C_{xx}R_{xx}} = \frac{\sum_{i=1}^n w_i \widetilde{\Delta\theta_i^{C_{xx}R_{xx}}}}{\sum_{i=1}^n w_i} \quad (3.21)$$

where the weight w was set to 0 (bad scan) or 1 (good scan) upon visual inspection of the map and n is the number of observations that captured Moon with the respective detector $C_{xx}R_{xx}$. As a consistency check, we also used the median value instead of averaging and did not see any significant difference. FIG. 3.5 shows the example of the azimuthal, and elevation offsets of the detectors on the ABS focal-plane for a particular wide Moon observation. The distribution of the offsets for all the Moon observations is shown in FIG. 3.6.

The whole process was iterated p times by setting $\nu_{p+1} \rightarrow \nu_p + \Delta\nu_p$, and $\omega_{p+1} \rightarrow \omega_p + \Delta\omega_p$ after each iteration. The values $\Delta\nu, \Delta\omega$ improved with every iteration and the residual error in the detector offsets was ≤ 1 arcmin after six iterations. The distributions of the final residuals after six iterations are shown in FIG. 3.7. Using this procedure we constrained the detector positions ν, ω for 93 per cent of the detectors on the ABS focal-plane. The remaining seven per cent were either dark detectors (or) stopped working around the middle of the first season.

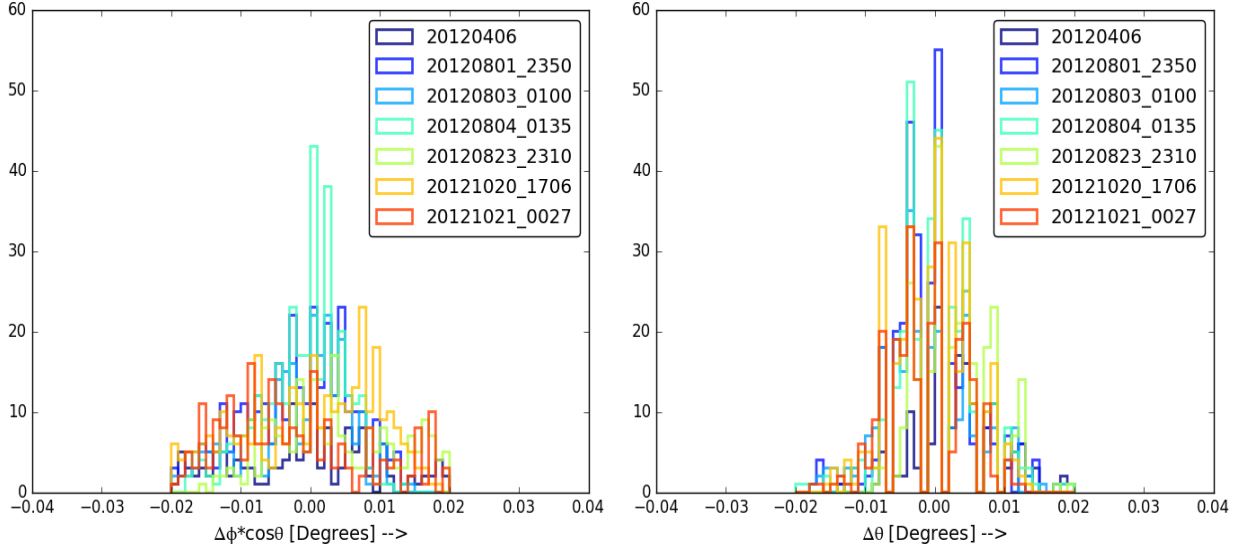


Figura 3.6: The distribution of the residuals $\Delta\phi\cos(\theta)$ (left), and $\Delta\theta$ (right) of every wide Moon observation used for the focal-plane pointing modelling. The residuals correspond to the values after six iterations where every iteration corresponds to 1. deriving the shifts in the detector positions using the offsets from the previous iteration; 2. map making with this shifts added; 3. deriving the new offsets for each detector from every observations; 4. use the average value of the offset for each detector from seven different observations.

3.3. Beam characterisation

A precise knowledge of the telescope beam is crucial for an accurate interpretation and extraction of the cosmological information from the CMB maps. The telescope beam defines the resolution power of the telescope. The angular resolution of a telescope can be theoretically calculated using the “Rayleigh formula” given in Eq. (3.22)

$$\Theta = \sin^{-1} \left(1.22 \frac{\lambda}{D} \right) \text{ radians} \quad (3.22)$$

where λ and D represent the wavelength and the telescope diameter in metres. But it is conventional to use frequency ($\nu = c/\lambda$ Hz, c = velocity of light in m/s) instead of wavelength for radio astronomy. The ABS telescope operating at a frequency of $\nu=150$ GHz with an aperture diameter of $D=25$ cm should have an angular resolution of $\theta \sim 33$ arcmins.

3.3.1. Beam window function

Provided the beam profile is azimuthally symmetric, the *window function* B_ℓ which is the response of the telescope as a function of multipole moments can be obtained by taking the square of the Legendre transformation of the beam profile. This is important for CMB experiments to measure the angular power spectra of the temperature, and polarisation anisotropies (see section 6.1). Since the residuals of the pointing offsets can expand the beam profile, the pointing residuals are taken into account along with the beam profile to obtain

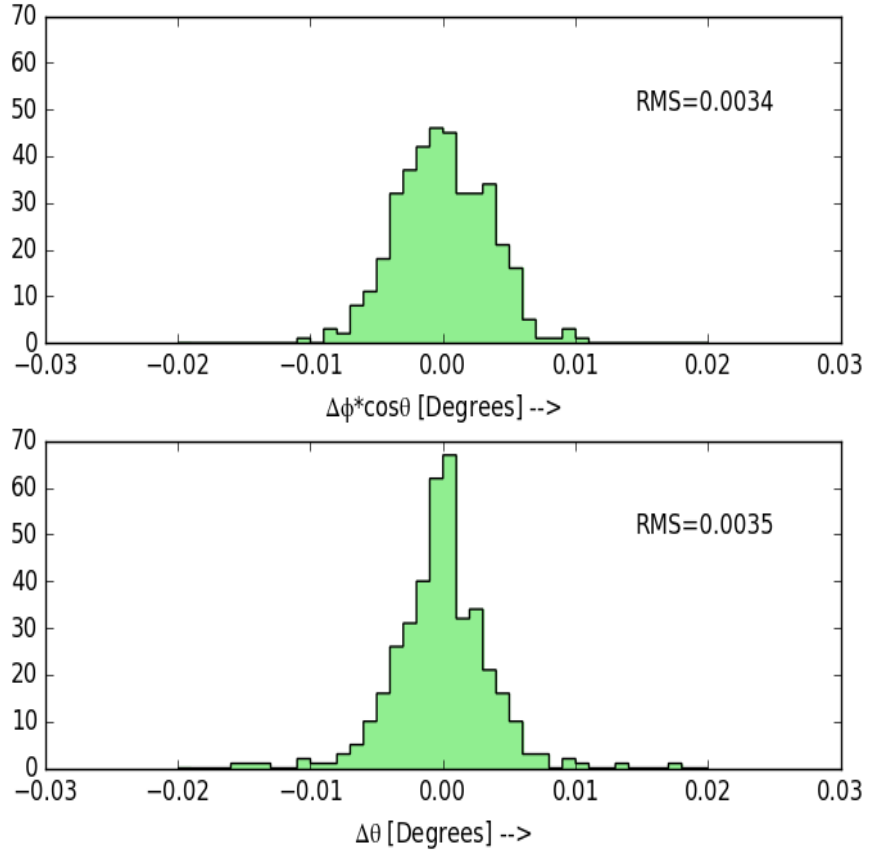


Figura 3.7: The distribution of the final residuals $\Delta\phi\cos(\theta)$ (top), and $\Delta\theta$ (bottom) after six iterations of the focal-plane pointing procedure described in the text. The rms value of the offsets are also mentioned in each panel. The data points were obtained using seven wide Moon observations from the first season.

B_ℓ .

$$B_\ell = \frac{4\pi}{\Omega_{\text{ABS}}} \left[\int b(\Theta) P_\ell(\cos\Theta) d(\cos\Theta) \right]^2 \quad (3.23)$$

where $\Omega_{\text{ABS}} = 2\pi \left(\frac{\sigma_{\text{ABS}}}{\sqrt{8\log(2)}} \right)^2 \sim 100.5 \mu\text{sr}$ is the main-beam solid angle, $\sigma_{\text{ABS}} = 32.4 \pm 1$ arcmins is the FWHM of the ABS Gaussian main-beam (see below), and the beam response at a radial distance Θ is given as

$$b(\Theta) = \exp \left(\frac{\Theta^2}{2\sigma_{\text{ABS}}^2} \right) \quad (3.24)$$

Subsequently for this symmetric Gaussian beam, the B_ℓ reduces to

$$B_\ell = \exp \left[\frac{\ell(\ell+1)}{2\sigma_{\text{BP}}^2} \right] \quad (3.25)$$

where σ_{BP} is the FWHM of the ABS beam profile σ_{ABS} along with the pointing residuals σ_p . The beam window function for ABS is shown in FIG. 3.8. The red, and green curves are for symmetric Gaussian beam (EQ. 3.25) with, and without pointing residuals. The polarisation beam is not shown as the correction factor for a symmetric Gaussian beam with no cross polarisation leakage is tiny. The black curve corresponds to actual ABS beam window function based on a sophisticated beam model. The curves have been normalised using the power at $\ell = 55$ corresponding to the first power spectral bin for ABS.

3.3.2. Beam profiles

For ABS, beam characterisation was performed using planet scans (Jupiter in particular as it is a bright and well understood nearby point source). Jupiter observations captured at different positions on the sky and at different times were stacked together to average out the mapping artefacts associated with a single observation. To stack the maps, we first fit 2d-Gaussians to individual maps and shift them so that the centroid of all scans fall at (0,0). As every detector (at least in different detector columns) could have a slightly different response to the incoming photons we did not stack observations from different detector columns together. Ideally all detectors are expected to have the same response.

The beam model was initially derived for detectors in the lower half of the focal-plane (detectors from batch-A). The detectors in the upper half of the focal-plane cannot capture Jupiter because 1. The ABS telescope cannot go below elevation of $\theta = 42$ degrees, and 2. Jupiter does not go to high elevations ($\theta \geq 46$ degrees) at the ABS telescope location. For the upper half detectors, we used Venus observations from the second observing season. We did not observe Venus during the first season as it was quite far way from Earth, and fainter to be captured by ABS. For the polarisation beams we used TauA, a supernova remnant in the taurus constellation and popularly known as the “Crab nebula”. This is discussed in the next section.

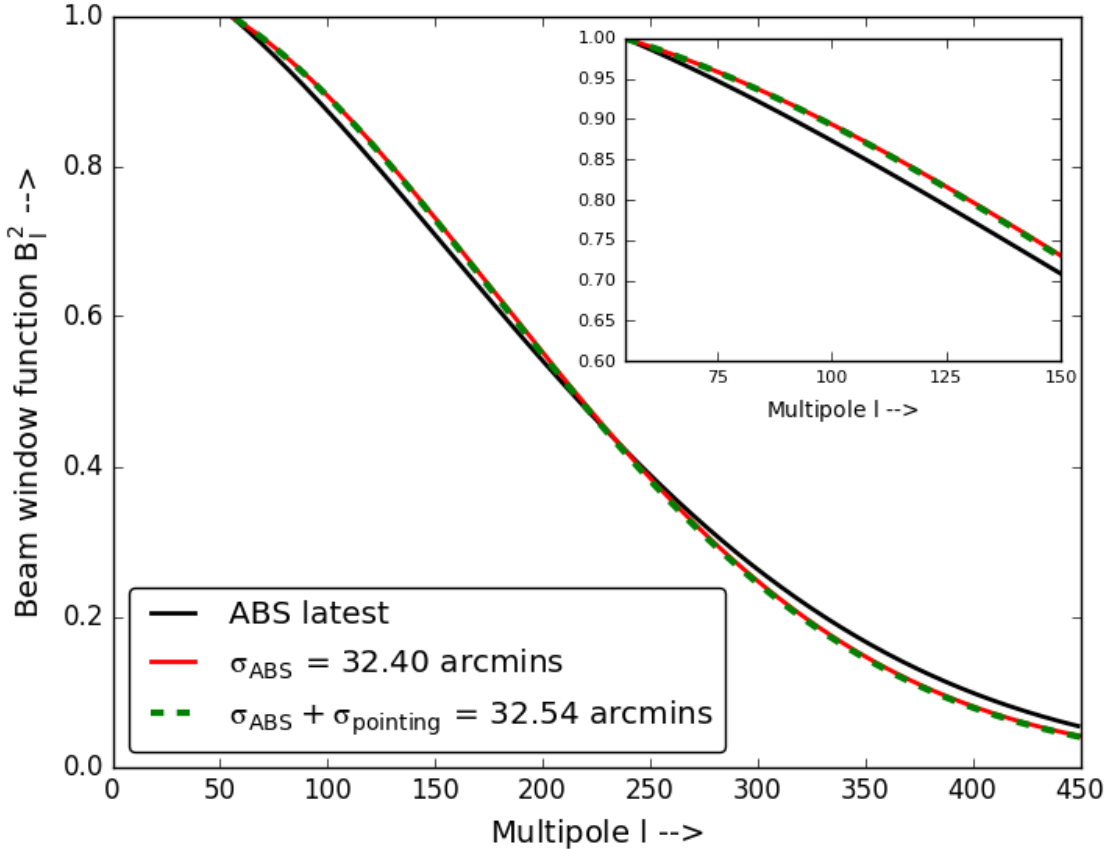


Figura 3.8: ABS beam window functions calculated using EQ. 3.23, 3.25. Three curves are shown. The black curve correspond to current ABS beam window function based on a sophisticated beam modelling along with the pointing residuals by Glen Nixon. The red, and green curves assume Gaussian beam EQ. 3.25 and correspond to ABS main beam, and mean beam with the pointing residuals included. The inset plot is the multipole region around the multipoles where the peak of the B-mode power spectrum is expected. The curves have been normalised using the power at $\ell = 55$ corresponding to the first power spectral bin for ABS.

The ABS beam was expected to be perfectly Gaussian from DADRA simulations. However, since the CMB photons will be truncated at the telescope aperture $D = 25\text{cm}$, we modelled the beam as the Fourier transform (FFT) of a truncated Gaussian. This model was fit to the stacked Jupiter observations. The main-beam of ABS was found to be a symmetric Gaussian with an FWHM of $\sigma_{\text{ABS}} \sim 32.4 \text{ arcmins}$. The Jupiter maps were made using the M3 mapper (see TAB. 3.1.1) after the basic filtering below. See section 4.1 for more details about the ABS data filtering techniques.

- base line removal using median filter.
- common mode removal by computing the median value of data from the detectors belonging to the same column.
- HWP A(χ) component removal.
- high azimuth scan turn over noise removal.
- notch filtering the bumps near scan frequency, and the HWP harmonics.

Some sample Jupiter observations from the first season after the above mentioned filtering targeted on the c23rxx detectors are shown in FIG. 3.9. The title of each panel show the date and time (YYYYMMDD_HHMM) of observation given in UTC format. Colour scale represent the Jupiter power in atto watts (aW). The stacked map of 25 Jupiter first season observations from c23rxx detectors is shown in the left panel of FIG. 3.10. The $\sigma_{\text{ABS}} = 32.4 \pm 1$ arcmins obtained using the FFT of the truncated Gaussian is used to produce the solid line in the radial profile plot of the stacked map (right panel of FIG. 3.10).

To characterise the side-lobes better, the beam model can be extended using Gaussian-Hermite (GH) polynomials (EQ. 3.26) as done for the WMAP satellite [53]. Since our first side-lobe power was ≤ -16.5 dB we did not consider this initially.

$$b(\Theta) = \exp\left(\frac{\Theta^2}{2\sigma_{\text{ABS}}^2}\right) \sum_{o=1}^n A_{2o} H_{2o}\left(\frac{\Theta}{\sigma_{\text{ABS}}}\right) \quad (3.26)$$

where o is the order of the GH polynomial H , A is the coefficient representing the contribution of a particular order to the side-lobes. In this equation, σ_{ABS} , o , A are the free parameters. Note that the equation uses only even ordered polynomials which signifies the azimuthal symmetry of the beam.

The beam modelling for the other detectors on the ABS focal-plane is being done by Glen Nixon using Venus observations, and the results from DADRA simulations. This is a more sophisticated model and accounts for side-lobes, and phase aberration and it is not a simple Gaussian beam. The beam window function computed using this model along with the residuals from the pointing is shown as the black curve in FIG. 3.8.

3.4. Crab Nebula observations and maps

3.4.1. Absolute polarisation angle

The TauA (Taurus A) or Crab nebula ($\alpha, \delta = 83.63, 20.01$ degrees) is a supernova remnant in the Taurus constellation. It is a highly polarised source and most widely used by the CMB polarisation experiments for calibrating the polarisation angle of the detectors accurately and to measure the cross-polarisation leakage. A highly precise measurement of the polarisation characteristics of TauA at 90 GHz has been provided by Aumont et al. [54] using the IRAM 30m radio telescope. Using maps of the I , Q , and U Stokes parameters they reported a flux value of 195.5 ± 11 Jy in intensity, and 14.5 ± 3.2 Jy in polarisation ($P = \sqrt{Q^2 + U^2}$) respectively with a mean polarisation fraction of $\langle P/I \rangle \sim 8.4\%$. The mean polarisation angle defined as $\gamma = \frac{1}{2}\tan^{-1}\langle U/Q \rangle$ was 152.1 ± 0.3 degrees.

We observed TauA to check the absolute polarisation angle calibration of the ABS detectors. This work was performed by Thomas Essinger-Hileman. FIG. 3.11 shows the stacked P polarisation intensity map of several TauA observations using detectors close to the telescope boresight (c23rxx). We obtained a polarisation angle value of $\gamma = 150 \pm 1.7$ degrees which is in excellent agreement with [54] mentioned above.

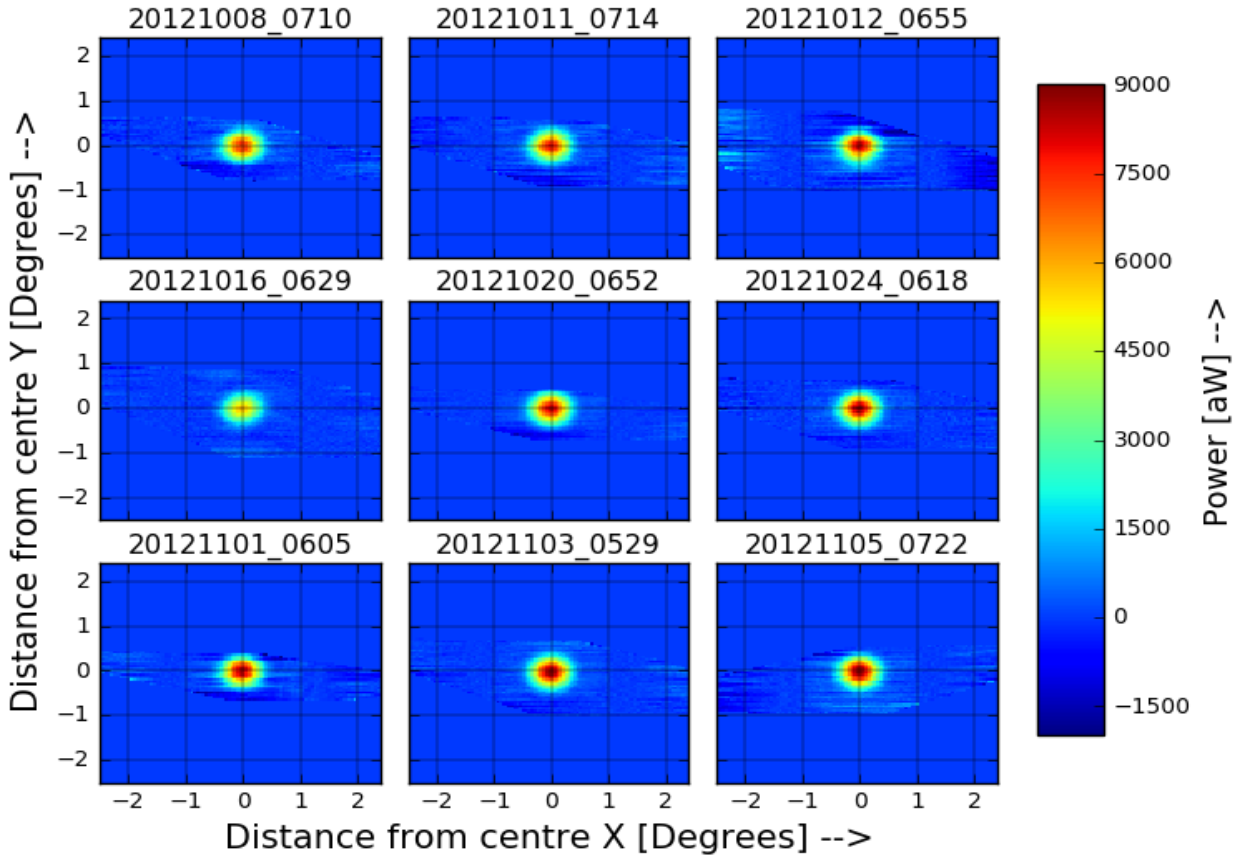


Figura 3.9: Sample Jupiter observations from season 1 data targeted on pod 23. Plot titles show the date and time (YYYYMMDD_HHMM) of observation given in UTC format. Colour bars represent the Jupiter power in aW.

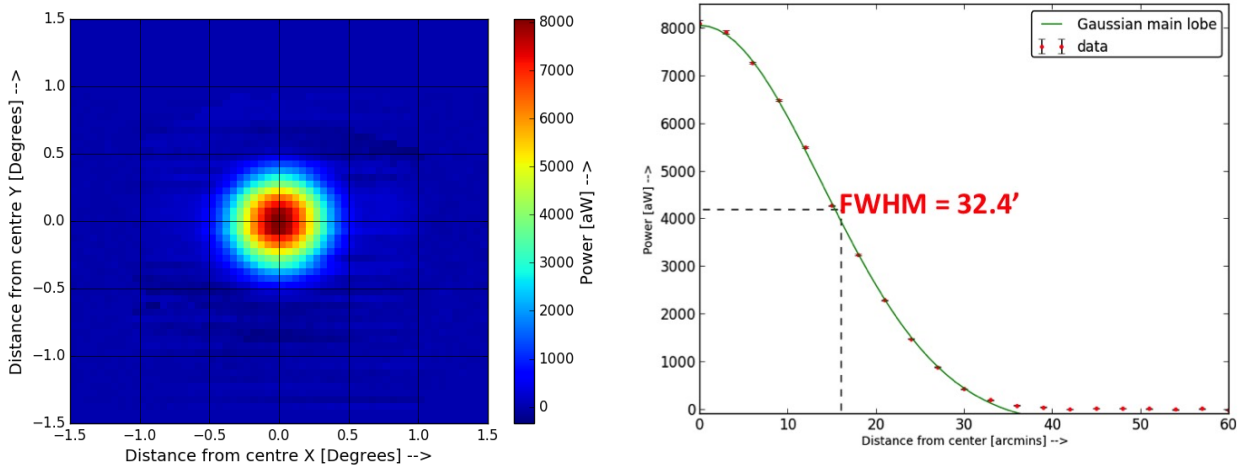


Figura 3.10: Stacked Jupiter scans captured using detectors on c23rxx during the first season. The left panel shows the stacked map, and right panel shows the radial profile of the stacked map. The green solid line correspond to the Gaussian main-beam with $\sigma_{\text{ABS}} = 32.4 \pm 1$ arcmins.

3.4.2. Accurate real-time pointing for bolivar and tight TauA scans

The map in FIG. 3.11 was produced by stacking several TauA observations using a special scan strategy. During the first season, TauA was observed normally using the procedure explained in section 2.3.3. However, the SNR of the source was too weak and no significant improvement was detected even after stacking multiple observations. As a result the scan strategy for TauA observations was modified during the second season by Lucas Parker. We call these *tight scans* as the scan amplitude was only 2.5 degrees and the telescope tracked the source by repointing every 5 minutes over the period of \sim 50 minutes. There was a significant improvement in the SNR with the new scan strategy (FIG. 3.11) and hence it was adopted for all future TauA observations. Note that a highly precise pointing technique is required for this new scan technique to capture TauA as we are scanning a small region around the source.

This pointing is not the offline pointing correction incorporated using the pointing model explained in previous section 3.1.1. Rather, this is the real-time pointing used by **bolivar**. The azimuth and elevation encoders record the boresight position $(\phi_{\text{tel}}, \theta_{\text{tel}})$ of the telescope on the sky at any instant of time. Using the detector offsets $(\nu_{\text{det}}, \omega_{\text{det}})$, $(\phi_{\text{tel}}, \theta_{\text{tel}})$ can be converted into $(\phi_{\text{det}}, \theta_{\text{det}})$ on the sky. To observe a source using a particular detector, **bolivar** performs an inverse calculation (i.e:) it converts $(\phi_{\text{det}}, \theta_{\text{det}})$ to $(\phi_{\text{tel}}, \theta_{\text{tel}})$ using a *flat sky approximation*. The field-of-view of ABS is quite large (22 degrees) and care must be taken to use the flat sky approximation for detectors at the edge of the focal-plane. The approximation works well for all detectors on the focal-plane for a normal scan strategy with a scan amplitude of 10 degrees. However, when using the tight scans to capture TauA with the edge detectors, the coverage was always poor, and the source was completely missed. An

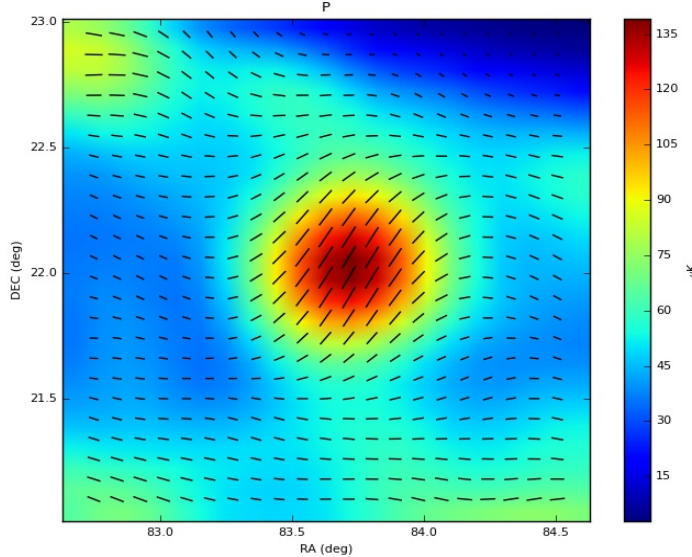


Figura 3.11: Stacked polarisation intensity map of several TauA observations using detectors close to the telescope boresight. The observed mean polarisation angle is $\gamma = 150 \pm 1.7$ degrees. Figure courtesy of Thomas Essinger-Hileman.

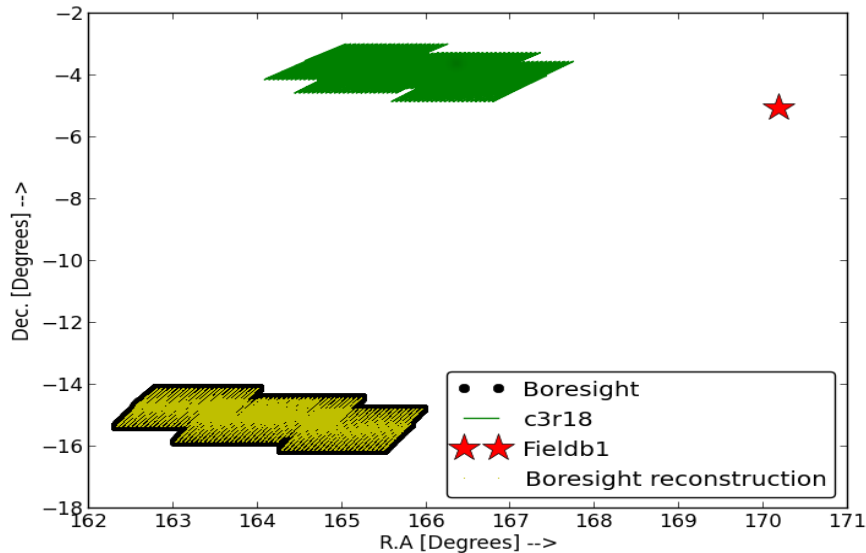


Figura 3.12: A test tight TauA type scan of field-B1 scan on 23 April, 2014 using the edge detector c03r18. Red star indicates the desired point to be scanned which has been missed by the scan (green) because of the flat sky approximation used by `bolivar`. The original boresight location is shown in black. The *boresight ->detector ->boresight* reconstruction using the exact pointing equations correctly places the reconstructed yellow region over the original black region.

accurate real-time pointing calculation was needed for `bolivar` in this case.

The equations EQ. 3.16, and EQ. 3.17 are shown here again for reference.

$$\vec{d}_s = \begin{pmatrix} \cos\phi_{ds} \cos\theta_{ds} \\ \sin\phi_{ds} \cos\theta_{ds} \\ \sin\theta_{ds} \end{pmatrix} = R_{hs} * \vec{d}_h \quad (3.27)$$

$$\vec{d}_s = \begin{pmatrix} \cos\phi_s \cos\theta_s & \sin\phi_s & -\cos\phi_s \sin\theta_s \\ -\sin\phi_s \cos\theta_s & \cos\phi_s & -\sin\phi_s \cos\theta_s \\ \sin\theta_s & 0 & \cos\theta_s \end{pmatrix} * \begin{pmatrix} \cos\nu \cos\omega \\ \sin\nu \cos\omega \\ \sin\omega \end{pmatrix} \quad (3.28)$$

The goal here is to obtain (ϕ_s, θ_s) from (ϕ_{ds}, θ_{ds}) which are the source positions. The inverse calculations will have two distinct solutions for ϕ_s . But, using the position of TauA at the expected time of observation the correct value can be easily obtained. The exact problem is shown in FIG. 3.13. We performed a test tight TauA type scan at the centre of the field-B denoted by the red star. `bolivar` should do the inverse calculation of getting $(\phi_{tel}, \theta_{tel})$ from $(\phi_{det}, \theta_{det})$ which is the red star to point the telescope boresight correctly. However, the flat sky approximation used results in a disappointing scan coverage for the edge detector c03r18 shown as green. The boresight position is shown in black. To test the new pointing equation, the *boresight ->detector ->boresight* was performed. This is shown as yellow in the figure. As it is evident, the calculation is exact.

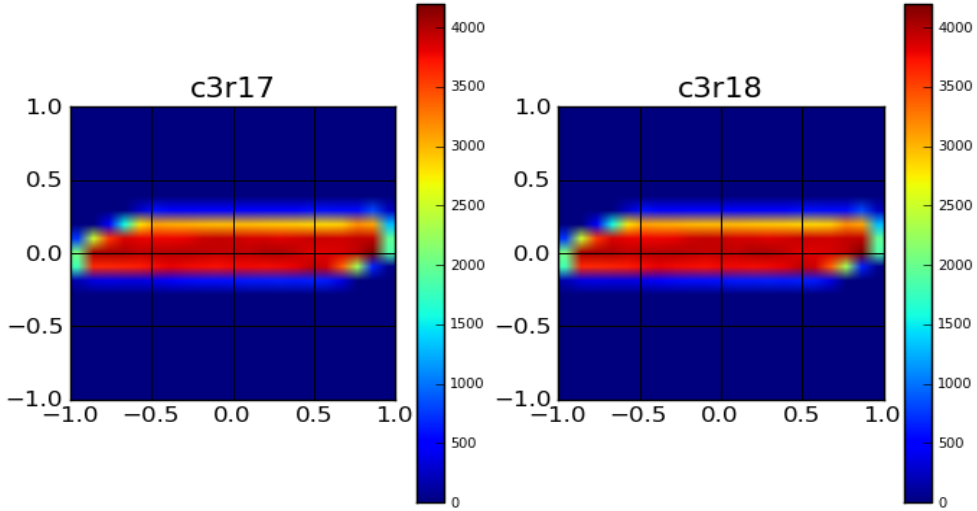


Figura 3.13: The hit map of two test tight TauA scans using two edge detectors. The exact Euler pointing calculation was used by `bolivar` for these scans. The coverage looks good. The colour scale represents the number of time samples with a sampling frequency of 200 Hz. The total time span of test scan was \sim 5 minutes.

3.5. Other calibrations

3.5.1. Jupiter temperature and detector responsivities

Blackbody spectrum

We used Jupiter observations to calibrate the ABS detectors (i.e.) to obtain the factor necessary for converting the detector flux values to the Rayleigh-Jeans (RJ) temperature units. Here I show the calculations of the Jupiter temperature along with necessary correction factors *viz.* the distance of Jupiter during the observation, and the beam solid angle of the ABS telescope.

Jupiter being a black body obeys Planck's law given by EQ. 3.29

$$B_\nu(T) = \frac{2\hbar\nu^3/c^2}{\exp(\hbar\nu/kT) - 1} [\text{erg s}^{-1} \text{ cm}^{-2} \text{ Hz}^{-1} \text{ ster}^{-1}] \quad (3.29)$$

where $B_\nu(T)$ is the specific intensity, ν is the frequency, T is actual temperature of Jupiter, \hbar is the Planck's constant, and k is the Boltzmann's constant. This is called the *thermal black body* spectrum of Jupiter and it extends to the entire electromagnetic frequency range. There is also a small non-thermal contribution to the Jupiter temperature due to the synchrotron emission of charged particles at low frequencies $\leq 40\text{GHz}$ [55], and is irrelevant for ABS observing frequencies.

At frequencies where $\hbar\nu \ll kT$, the EQ. 3.29 can be approximated to Rayleigh-Jeans

law given by EQ. 3.30

$$B_\nu(T_{RJ}) = \frac{2\nu^2}{c^2} k T_{RJ} [\text{erg s}^{-1} \text{ cm}^{-2} \text{ Hz}^{-1} \text{ ster}^{-1}] \quad (3.30)$$

where the subscript RJ indicates the low frequency approximation of EQ. 3.29. The T_{RJ} is also called as the *Brightness temperature* of the blackbody (Jupiter in this case T_J). The temperature obtained from EQ. 3.30 depends on the directionality of the antenna given by the *beam solid angle* Ω and must be integrated over the entire sky (4π radians) to obtain the temperature corresponding to the radiation (field) in all directions. Subsequently, brightness temperate T_J of Jupiter can be written as

$$T_J = \int_{4\pi} T_{obs} d\Omega [\text{K}] \quad (3.31)$$

where T_{obs} is the observed temperature. Also, note that since ABS observes at a particular frequency we will only be sensitive to a small window in the black body spectrum centered around $\nu = 145$ GHz which is the observing frequency of ABS.

Calibration using WMAP measurements

We use the WMAP's *W-band* (93 GHz) measurements of Jupiter for calibration purposes ($T_{obs} = T_{WMAP}$ in EQ. 3.31). The WMAP team [53, 55] adopted a reference distance of $d_J = 5.2$ AU for all beam referencing because of the considerable change in the Jupiter distance (d_J) all around the year. EQ. 3.31 has accordingly been modified as

$$T_{J_{WMAP}} = \int_{4\pi} T_{WMAP} d\Omega / \Omega_{J_{WMAP_{ref}}} [\text{K}] \quad (3.32)$$

where $T_{WMAP} = 173\text{K}$ is the WMAP observed temperature temperature of Jupiter, and $\Omega_{J_{WMAP_{ref}}}$ is the reference beam solid angle from [56] as used by the WMAP team.

$$\Omega_{J_{WMAP_{ref}}} = 2.481 \times 10^{-8} [\text{sr}] \quad (3.33)$$

The corrected apparent beam solid angle Ω_J for the matter of interest is given by

$$\Omega_J = 2.481 \times 10^{-8} \left(\frac{5.2}{d} \right)^2 [\text{sr}] \quad (3.34)$$

where d is the distance of Jupiter during the time of observation. Jupiter's brightness temperature for the ABS telescope $T_{J_{ABS}}$ can now be obtained from WMAP determined $T_{J_{WMAP}}$ using EQ. 3.35

$$T_{J_{ABS}} = T_{J_{WMAP}} \frac{\Omega_J}{\Omega_{ABS}} [\text{K}] \quad (3.35)$$

The ABS beam solid angle Ω_{ABS} is

$$\Omega_{ABS} = 2\pi \sigma_{ABS}^2 [\text{sr}] \quad (3.36)$$

where $\sigma_{ABS} = 32.4$ arcmins is the FWHM of the ABS main beam (see section 3.3.2). The value of Jupiter temperatures after the above corrections for ABS reference detectors was $T_{J_{ABS}} = 63.54 \pm 4.28$ mK.

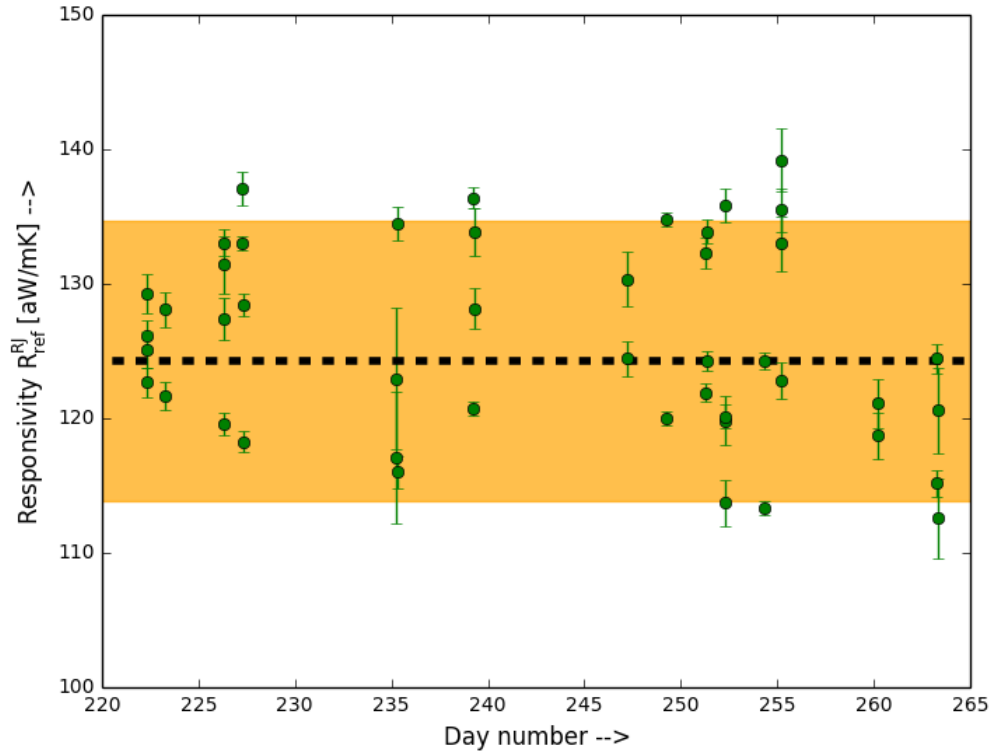


Figura 3.14: Responsivites of individual detectors in ABS using Jupiter observations from season 1 data. The horizontal axis of the plot show the day number starting from 28th February, 2012 when ABS saw the first light.

Absolute detector responsivities

We performed the “absolute” calibration using the Jupiter data for a set of reference detectors d_{ref} from column c23 as they are located near the centre of the focal-plane and belong to batch-A which have well calibrated beams, and bandpass responses. Once the Jupiter temperatures have been obtained as described above, the absolute responsivities ($R_{\text{ref}}^{\text{RJ}}$) of reference detectors can be readily calculated as

$$R_{\text{ref}}^{\text{RJ}} = \frac{\text{Power}_{\text{J}_\text{ABS}}}{T_{\text{J}_\text{ABS}}} \left[\frac{\text{aW}}{\text{mK}} \right] \quad (3.37)$$

FIG. 3.14 shows the responsivites of the ABS reference detectors from column c23 using Jupiter observations from the first season. The horizontal axis of the plot show the day number starting from 28th February, 2012 when ABS saw the first light. The responsivities were calculated using maps of Jupiter made using M3 algorithm. The dashed black line, along with the 1 σ orange band show the median absolute responsivity value of $R_{\text{ref}}^{\text{RJ}} = 124.24 \pm 10.39 \text{ aW/mK}$. The responsivity values (not shown here) using Jupiter observations were also obtained for other detectors in the lower half of the focal-plane during the first two seasons. The continuos monitoring did not reveal any seasonal degradation of the responsivity values for the Jupiter targeted detectors.

Relative detector responsivities

To measure the relative detector responsivities, we manually inserted a circular frame containing sparse wire grid above the HWP. This technique was first used by the QUIET experiment [59]. The wire grid consists of reflective parallel wires spaced at 2.5 cm. This induces an artificial polarisation signal onto the detectors. The grid was also rotated in the clockwise direction (detectors looking at the sky) in discrete steps of $\beta = 22.5^\circ$ around the telescope boresight to modulate the induced polarisation signal. These observations were made with the telescope pointing to zenith (only because it is easy for the manual insertion of the wire grid), and normally were 6.5 minutes long. ~30 seconds of data was taken at each rotation angle β .

The amplitude of the sinusoidal response ($A_{\text{det}}(\beta) \propto \sin(2\beta)$) of all the detectors to the rotating wire grid was analysed using the Stoke's parameters Q , and U of the demodulated TODs. The “relative” detector responsivity of the detectors, defined as the ratio of the amplitude of the detector’s response to the reference detector $r_{\text{det}}^{\text{grid}} = \frac{A_{\text{det}}(\beta)}{A_{\text{ref}}(\beta)}$ was calculated. We performed ten such observations, and the median value of all $r_{\text{det}}^{\text{grid}}$ measurements was used as the responsivity of a particular detector. The conversion factor for a detector i to convert the flux value into temperature units is thus $R_{\text{ref}}^{\text{RJ}} \times r_i^{\text{grid}}$. The wire grid analysis work was performed by Akito Kusaka, Patty Ho, and Steve Choi.

The continuous monitoring of the responsivities of detectors showed a slight degradation in the responsivities of batch-B detectors. We did not have Jupiter observations on batch-B detectors for a cross-check. No seasonal variations were discovered for batch-A detectors though. Subsequently we used two responsivity models in the analysis pipeline, one with a constant respective responsivity value of all detectors, and the second with the seasonal variation for the batch-B detectors.

3.5.2. Polarisation angle of detectors

The rotating wire grid measurements described above can also help in deriving the *relative* polarisation angles of the detectors with respect to the HWP encoder. But here we use the phase ϕ information of the sinusoidal response of the demodulated 4f component (Q , and U) instead of the amplitudes. A subtle point here is that the phase also depends on the detector response time τ by

$$\phi = \phi_0 + (4f * 2\pi \tau) \quad (3.38)$$

We also made seven non-rotating wire grid measurements where the wire grid was aligned to the azimuth north direction to measure the *absolute* detector angles. The wire grid analysis for detector angle measurements was performed by Steve Choi. The polarisation angle of TauA was checked using the detector angles obtained from the wire grid measurements. The $\gamma_{\text{TauA}} = 150 \pm 1.7$ degrees is consistent with the measurements from other experiments (see section 3.4.1). Monthly measurements using the wire grid did not show any major shifts in the values of the detector angles.

3.5.3. Detector bandpass, and time constants

To measure the detector bandpass, and central frequency we used the Fourier Transform Spectrometer (FTS).⁵ Two mirrors, one fixed and other movable, were placed orthogonal to each other and the light from a source is split by a beam splitter equally to both the mirrors. The reflected light from both the mirrors are combined together and transmitted to the detectors on the ABS focal-plane. Nothing interesting happens when both mirrors are stationary except producing the maxima. But, when the movable mirror moves forward and backward on its axis, an interference pattern is produced. The interference patterns were averaged and apodized using a *Welch apodization function*. The FFT of this apodized signal is the bandpass (frequency response) of the detector. We grouped the detectors based on their fabrication information and performed the FTS measurements independently for each group.

Using the EQ. 3.39, we found the central frequency f_c for each group of detectors

$$f_c = \frac{\int v f(v) \alpha dv}{\int f(v) \alpha dv} \quad (3.39)$$

where $f(v)$ is the interference pattern observed at frequency v , and the term α captures the frequency dependance of the thermal radiation of the CMB. The centre frequency of the reference detectors were $f_c = 154.1 \pm 3.4$ GHz. The f_c of other detectors in batch-A were roughly close to this value ~ 157 GHz. The f_c of batch-B detectors were lower ~ 143 GHz. We identify that the reason for this bandpass shift is due to the changes in the fabrication process. The bandwidth of the reference detectors was 36.1 ± 2.1 GHz. The bandwidth of other detectors was ~ 35 GHz. More details about the detector bandpass and the FTS measurements can be found in [34].

The bolometer time constant is the response speed of the bolometer for a fractional change from its initial value P_i to final value P_f by $P_i + \Delta P_{fi} \exp(-t/\tau)$. Subsequently it is the ratio of the amount of heat required to raise the temperature of the detectors (heat capacity C) to the conductivity (G). Thus the time constant of the detector can be measured by modelling its response using an exponential decay to a step voltage signal. There are also other ways to measure τ . As mentioned in 1. section 3.1.1 the slow response of detectors can cause shifts in the centroid of the point source depending on the scan direction, 2. section 3.5.2 the phase angle of the 4f will vary based on the detector time response. Apparently, the time constants can also be measured using these two steps. However, the shift in the centroid of the point source was too small to detect for ABS, and we relied on the 4f response of the detectors to the rotating wire grid measurements. We rewrite τ in EQ. 3.38 using a new parameter $f_{3dB} = 1/2\pi\tau$ and model it as $\tan^{-1}\left(\frac{4f}{f_{3dB}}\right)$. The f_{3dB} is the frequency at which the detector response drops by 50 per cent. The average value of the time constants for the ABS detectors is 1.6 milli sec corresponding to $f_{3dB} \sim 100$ Hz. The detectors with a slow response will have a smaller f_{3dB} and we ignore all detectors with $f_{3dB} \leq 30$ Hz (or 5.2 milli sec) during data selection. The FTS, and the detector time constant measurements were performed by Sara Simon.

⁵<http://scienceworld.wolfram.com/physics/FourierTransformSpectrometer.html> shows a FTS setup.

Capítulo 4

DATA PROCESSING AND CUTS

Overview, and goals:

This chapter deals about the basic filtering techniques employed while processing ABS data, and the cuts applied due to undesired events during the observations. My work focussed particularly on

- identifying, and accounting for the unexplained failures of azimuth encoder, and the GPS in the pointing model.
- modelling the undesired “ghost” images of bright sources.
- investigating the presence of correlated noise in the data.
- detecting the far-side lobe contamination.

4.1. Data corrections

This section deals with the preliminary corrections applied to the detector TODs, followed by the different data selection techniques used to pick the good CESes, and the detectors for the map making process. The other sections of this chapter deal with other sources of data contamination and the way they were handled for ABS. As mentioned in section 2.4, the merging of detector TOD, housekeeping information, and the telescope motion control using a master clock is performed by `bolivar`. This merged data was checked, and corrected for the below issues.

Glitches

We first searched for *sporadic glitches that are due to cosmic ray hits, and detector readout malfunctions* in the merged TOD. To identify the glitches, 1. the TOD is first smoothed (low pass filtered) using a *median filter* of a specific window size W , 2. this smoothed TOD is now subtracted from the original TOD, and the standard deviation σ of the cleaned TOD

is calculated, 3. The samples that exceed a specific threshold $N\sigma$ are termed as *glitches* and were masked. The glitches normally do not span several time samples, and hence the window size W can be very narrow. We used a $W = 10$ for the glitches due to cosmic ray hits, and $W = 2$ for the ones due to detector readout issues. The same process can also be performed by using a *Gaussian filter smoothing* instead of the median filter.

The next is to identify, and correct the jumps in the DC levels in the detector TODs that are a result of the issues with flux-locked SQUID readout. There were also *integer jumps* which were due to the DAQ counts exceeding the maximum number of storage bits. These jumps were only present when observing extremely bright sources *viz.* the Moon. Although the integer jumps can easily be corrected, we ignored them from the pipeline as the jumps were absent for CMB scans. Detailed statistics of the all the above glitches were recorded for each detector TOD, and stored in the *abs_offline* MySQL database.

$1/f$ noise modeling

A $1/f$ noise fit based on EQ. 4.1 were fit to the power spectrum ($\text{abs}(\text{FFT})^2$) of each detector TOD. The noise model contains three parameters *viz.* 1. the white noise amplitude A , 2. the knee frequency f_{knee} which is defined as the frequency where the levels of $1/f$, and white noise are equal, and 3. the decay of the $1/f$ noise towards higher frequencies determined by the slope α .

$$P(f) = A^2 \left[1 + \left(\frac{f_{\text{knee}}}{f} \right)^\alpha \right] \quad (4.1)$$

The scan frequency region $f \sim 0.04$ Hz was masked before performing the noise fitting. For ABS, the f_{knee} will be relatively lower at mHz range because of the exceptional performance of the HWP in removing the atmospheric $1/f$ noise. Nevertheless, a high pass filter is designed based on the noise model, and it acts to suppress the $1/f$ noise in the detector TODs.

HWP, and the Scan Synchronous Structure (SSS) removal

Like mentioned in section 2.5, the usage of HWP introduces an additional spurious component. This is because of the emissivity of the HWP component, and the unpolarised sky signal synchronous to the HWP rotation. Together, they are the $A(\chi)$ component in the demodulation equation EQ. 2.3. For a well behaved smoothly spinning HWP, the $A(\chi)$ is stable over time and dominated by the $2f$ component. The modulated CMB signal, however, is expected near the $4f$ where the contribution of $A(\chi)$ is expected to be minimum. From the FIG. 4 of [48] it is clear that this is true for ABS. Regardless of this, the raw TOD was first binned using the HWP encoder counts to remove the $A(\chi)$ component before the demodulation step. Similarly, there are also structures that are synchronous to the scan (SSS) direction (azimuthal in case of ABS) and if not accounted for can show up as strong features on the CMB map. These structures can be modelled using higher order polynomials by binning the data using azimuth encoder values. For ABS, a 20 degree Legendre polynomial was used to

model the SSS. This fit was removed from the demodulated TOD (binned in azimuth) to eliminate the SSS. We use χ^2 statistics to estimate the goodness of the SSS modelling. This work was performed by Kevin Crowley, and Akito Kusaka. We also use these χ^2 values to perform a null test (see section 6.2.2) to estimate the systematics. We also reduce the high noise near the scan turn arounds because of the uneven velocities, and jerks. This was done by subtracting the baseline near the azimuth scan edges.

4.1.1. Data selection

Our data selection techniques were both at the CES level, and at the TOD level. The following statistics were created with the help of a script provided by Sara Simon. In all the below SQL commands, the day_number = 255.5, and 800 correspond to start of first, and end of second season respectively. The queries are to extract entries from `abs_offline` database.

Firstly all observations with a scan duration less than 100 seconds, (or) poor azimuth scan widths were removed.

```
select CONCAT(sched_id,'.',sched_subid) from abs_scan natural join
abs_TOD natural join abs_TOD_derived_tes natural join abs_ces_iv_tes
where target like "fielda" and (duration >= 1000) AND (scan_az_width >
5) AND (scan_az_width <= 25) and (day_number >= 255.5 and day_number <
800.0);
```

The CES level data selection was based on the observing conditions, and the HWP performance. Since a large water vapour column level introduces high optical loading on the detectors, the *observations performed during poor weather (PWV $\geq 3\text{mm}$) conditions were not considered for further data analysis*. Look into section 2.2 for evidence of the degradation of the detector performance as the PWV raises. The PWV cut passed 2057 hours, and ignored 144 hours of CMB field-A observations. The SQL query to select CMB field-A data during good weather conditions is below.

```
select CONCAT(sched_id,'.',sched_subid) from abs_scan
natural join abs_housekeeping where target like "fielda" and
abs_housekeeping.apex_pwv_mean <= 3 and (day_number >= 255.5 and
day_number <= 800);
```

Since HWP is a key component of the ABS telescope, and its rotation is crucial we ignored the CESes in which the HWP did not rotate properly. The HWP is extremely important to differentiate the large unpolarised atmospheric signal from the small polarised cosmological signal. The most common reason for the HWP stoppage was when the telescope scanned closer to the Sun. The HWP is supported by air bearings for a minimal friction while rotation. Pointing close to the Sun caused some of the HWP supporting elements to expand (due to heat) causing friction ultimately leading to the HWP stoppage. For the CMB field-A scans, the ABS telescope was never pointed close to the Sun and hence the HWP stoppage problem was hardly experienced. The CESes in which the HWP did not rotate at its nominal frequency

of 2.55 Hz were cut allowing 2370 hours, and removing only 27 hours of observation.

```
select CONCAT(sched_id,'.',sched_subid) from abs_scan where target
like "fielda" and hwp_frequency >= 2.5 and (day_number >= 255.5 and
day_number <= 800);
```

The CESes that passed the above two cuts will be called the “*passed*” CESes from now. We selected the detector TODs from the passed observations based on the glitch statistics, detector biasing, SSS removal, white noise amplitude, and 1/f knee frequency. The detectors with zero responsivities were removed.

The glitches described above were completely random events. Subsequently all detectors with more than 200 cosmic ray type *10-sample*, and 100 detector readout failure type *2-sample* glitches were removed.

```
select CONCAT(sched_id,'.',sched_subid), col, row from abs_scan
natural join abs_TOD where target like "fielda" and
(n_2sample_glitch_10sigma <= 100 and n_10sample_glitch_10sigma <= 200 and
n_squid_jump <= 2.5) and (day_number >= 255.5 and day_number <= 800);
```

Using the 1/f model fitting in EQ. 4.1, the TES detectors with *sensitivity (white noise level) worse than $150 \text{ aW}\sqrt{\text{sec}}$, and a high 1/f $f_{\text{knee}} \geq 50 \text{ mHz}$ were removed. The detector TODs to which a satisfactory fit was not obtained were also ignored based on the χ^2 values.*

```
select CONCAT(sched_id,'.',sched_subid), col, row from
abs_scan natural join abs_TOD where target like "fielda" and
(demod_chisquare_above_1Hz <= 4 and demod_chisquare_below_1Hz_excl_scan
<= 4 and demod_white_noise_ampl >= 20 and demod_white_noise_ampl <= 150
and demod_knee_frequency <= 0.05) and (day_number >= 255.5 and day_number
<= 800.0);
```

A limit was also set on the presence of the structures synchronous to the scan by calculating the χ^2_{SSS} based on the Legendre polynomial fit. Since the CMB (polarisation) signal is extremely faint the detector TODs are typically white noise dominated, and hence are expected to follow a Gaussian normal distribution. We devised cuts to remove bad TES detectors based on some simple tests based on the stationarity, and the first four moments. The SQL query for these cuts is below.

```
select CONCAT(sched_id,'.',sched_subid), col, row from
abs_scan natural join abs_TOD natural join abs_TOD_derived where
target like "fielda" and (demod_scan_synchronous_chi2_real +
demod_scan_synchronous_chi2_imag > 50 and demod_sss_median > 5 and
demod_stationarity <= 0.2 and raw_stationarity <= 0.2 and raw_skewness
>= -0.3 and raw_skewness <= 0.3 and raw_kurtosis <= 5.0 ) and (day_number
>= 255.5 and day_number <= 800.0);
```

The IV curves, HWP 2f signal, and the $f_{3\text{dB}}$ frequencies were used to remove the slowly responding bad detectors. The detectors for which more than 25 per cent of the TOD was masked due to high noise during the 1/f noise modelling were also removed.

```
select CONCAT(sched_id,'.',sched_subid), col, row from
abs_scan natural join abs_TOD natural join abs_TOD_derived_tes
natural join abs_ces_iv_tes where target like "fielda" and
(day_number>380.5 and hwp_2f_chi>4.5 and hwp_2f_flag=1 and is_good and
noise_flareup_mask_fraction <= 0.250000) and (day_number >= 255.5 and
day_number <= 800.0);
```

Finally, the *CESes with less than 150 passed detectors were not considered for the map making stage*. FIG. 4.1 show the amount of time the data from a TES detector contributes to the final CMB map after incorporating the above mentioned cuts. The four sub panels are for different ABS fields. The plots have been normalised to one, and the total observation hours from the CESes that passed the cuts are 1920, 64, 239 for the three CMB fields A, B, C, and 146 hours for the galactic patch respectively.

4.2. Encoder slips

4.2.1. Details about the unknown encoder slips

We encountered three instances of large unexplained azimuth encoder slips. Although the reason for these shifts remain unknown, due to continual monitoring of the telescope pointing using point source observations (see Table 4.2.3), the shifts were identified almost immediately leading to minimal loss of CMB data. The first of these shifts was $\sim 9^\circ \text{N}$ and occurred sometime between 04 August, 2012 and 23 August, 2012. No point source observations were made during this intermediate period and hence the exact date of shift remains unknown. This event also prompted us to continuously monitor the pointing from then on. The second shift was $\sim 7.8^\circ \text{E}$ on the 01 June, 2013 and was identified on the same day using Moon observation. The third shift of $\sim 1.2^\circ \text{N}$ occurred on the 04 November, 2013 and was also immediately resolved using Jupiter observation.

4.2.2. Other events

There was another period of 15 days during the month of October, 2013 when the pointing code reported large azimuth, and elevation encoders shifts. This was due to failure of the Global Positioning System (GPS) system and will be explained in the following section 4.2.3. During the third season we had the azimuth encoder breakage on 07 July, 2014 and the encoder was subsequently replaced. All the above events are “real” events.

Finally, the pointing model reported

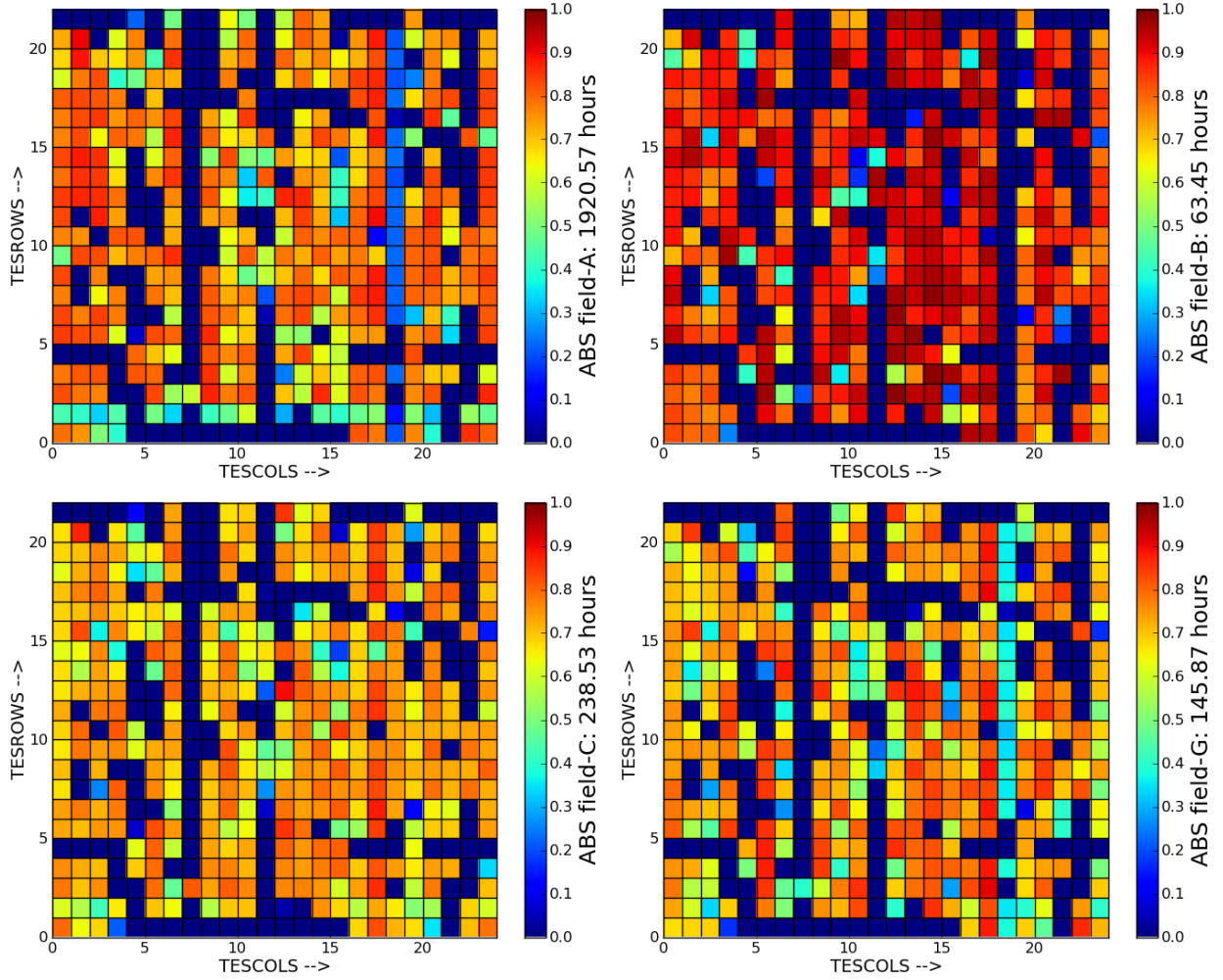


Figura 4.1: The contribution of each TES detector to the final map making stage based on the data selection techniques described in section 4.1.1 for all the ABS scan fields. Note that the data selection techniques were only based on the CMB field-A, and the other fields are just shown for the entirety. The colour bar represents the total observation hours based on the passed CESes.

- $\sim 0.1^\circ$ shift in the elevation encoder data after the end of first observation season.
- $\sim 0.1^\circ$ shift in the azimuth encoder during the month of September, 2013.

Note that the above two shifts are not real events, and were guessed based on the results of the pointing model. The corrections for the above two issues were effected by using two versions of the pointing code in the analysis pipeline (with, and without the 0.1° shifts). Any systematic error due to this correction will be reported in the ABS science results [12].

The figures in the following pages show the azimuth (FIG. 4.2), and elevation offsets (FIG. 4.3) as a function of observation time. The stars (circles) represent Jupiter (Moon) observations, and the colour of each data point represent the distance of the detector (that captured the source) from the boresight. The need to use different colours for different detectors was to show that there are no systematic shifts due to our pointing code that converts $(\phi_{\text{tel}}, \theta_{\text{tel}})$ to $(\phi_{\text{det}}, \theta_{\text{det}})$. Note again that the ABS field-of-view is $\sim 22^\circ$, and a small approximation in the pointing calculation could lead to significant (based on the detector position on the focal-plane) pointing shifts. The yellow bands in the figures show the period of no observations either due to weather related issues, (or) instrument failure. The red (blue) vertical lines enclose the first (second) season of observation. The dashed magenta lines show the dates of the different azimuth encoder slips. The magnitude of the shifts are marked in the figures.

4.2.3. Faulty GPS

After accounting for all the encoder slips discussed above, three Jupiter observations (20131011_1115, 20131012_1119, and 20131013_1102) and two wide Moon observations (20131011_2007, and 20131012_1958) during October, 2013 were found to have large $\sim 0.3^\circ$ offsets. As a consistency check, maps of these observations were made using different mappers (M1, M2, and M4) (see section 3.1.1 for definitions of different ABS mapping algorithms). Irrespective of the mapping algorithm, the pointing offsets were always large. Fig. 4.4 shows the map of two of these observations with two different mappers (top panel - M2, and bottom panel - M4).

While the reason for this weird shift was not clear initially, the systematic shift of the detector offsets of a wide Moon observation (see FIG. 4.5) hinted a problem with the recorded `unix time` of the observations. Finally using the GPS housekeeping information we found that the ABS GPS was not working properly during the above observations. As a result, all CMB scans performed during this faulty GPS period (4 October, 2013 to 13 October, 2013) were ignored from further processing.

Finally, in table 4.2.3, I summarise the details about all the azimuth encoder slips and the GPS failure events during the three seasons of ABS observations as detailed above.

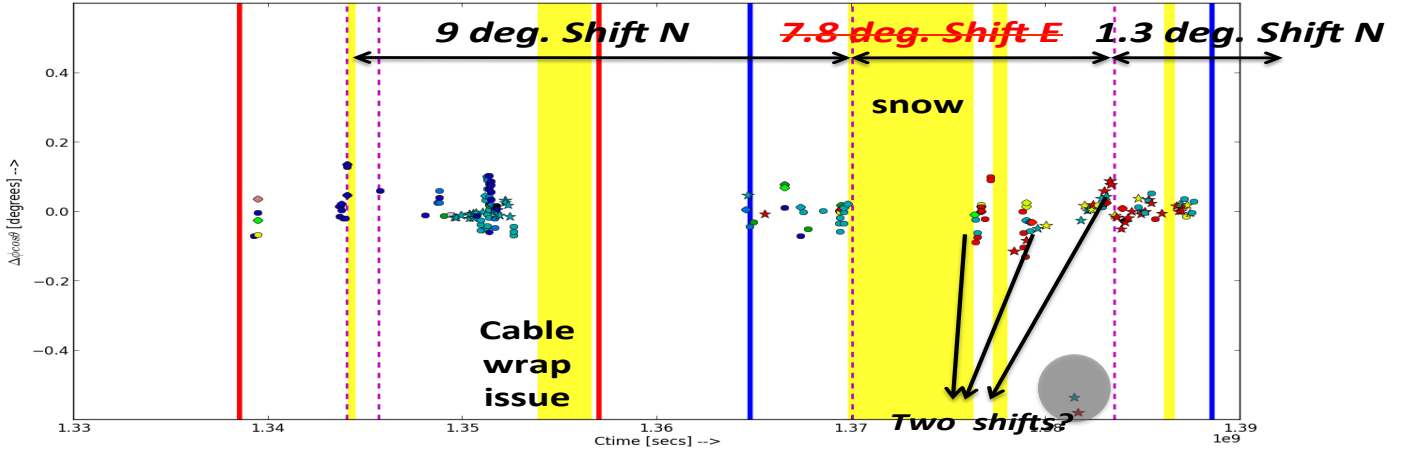
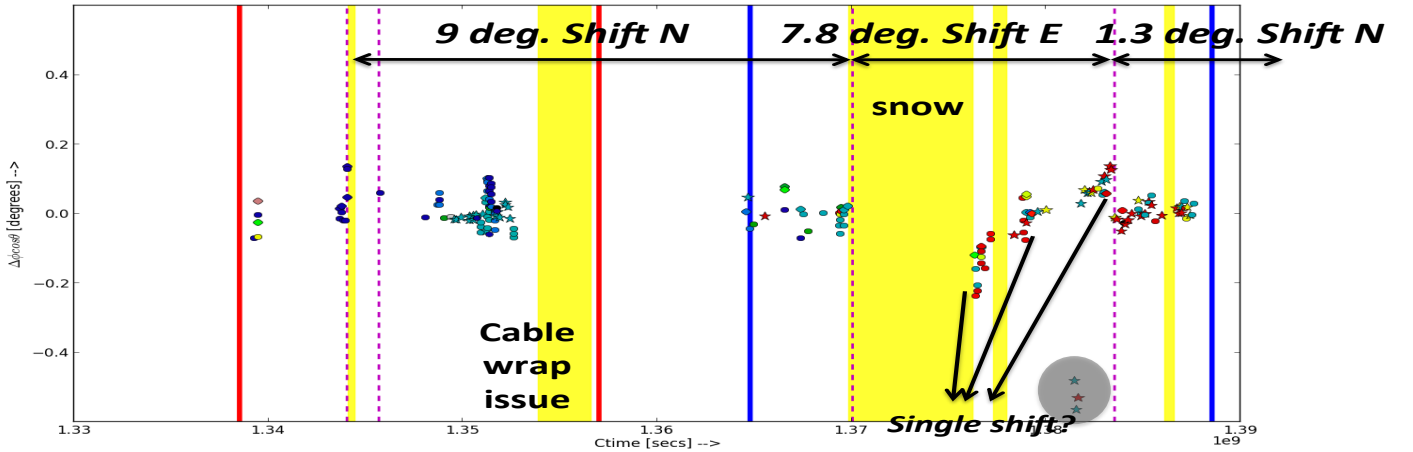


Figura 4.2: The azimuth offsets of point source observations as a function of the observation date during the first two seasons. Stars, and circles correspond to Jupiter, and Moon observations. The colour of the data points represent the distance of the detector that captured the source from the boresight (blue = near; red = far). The yellow bands correspond to dates when no observations were made due to weather (or) instrument related issues. The red, and blue vertical lines enclose the season 1, and 2 respectively. The dashed magenta lines show the date of the azimuth encoder slips. The magnitude, and the direction of all the shifts are marked. The three stars at the bottom enclosed by black circle of the plot correspond to Jupiter observations made during the faulty GPS period. The data points in the far right in the top panel correspond to observations in September 2013, where there is an additional 0.1° shift. These were handled by two different version of the pointing model as mentioned in the text and the result is shown in the bottom panel.

Colour of the data points not to be considered

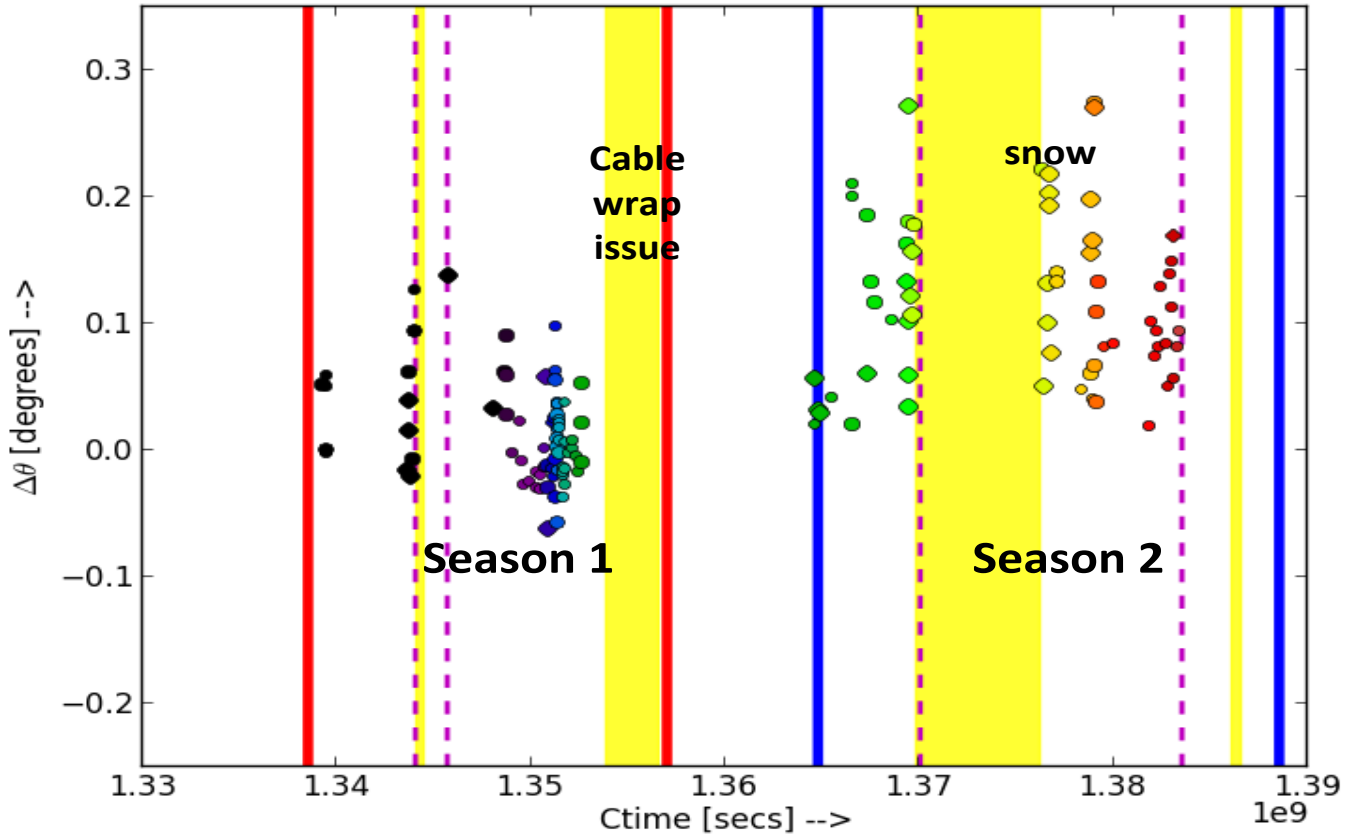


Figura 4.3: Similar to FIG. 4.2 but the vertical axis correspond to elevation offsets during the first two observation seasons. The increase in the elevation offset ($\sim 0.1^\circ$) during the second season is evident here. I emphasise that the colour of the data points in this plot only correspond to observation date (same as the horizontal axis) unlike the detector location on the focal-plane in FIG. 4.2, and not to be considered.

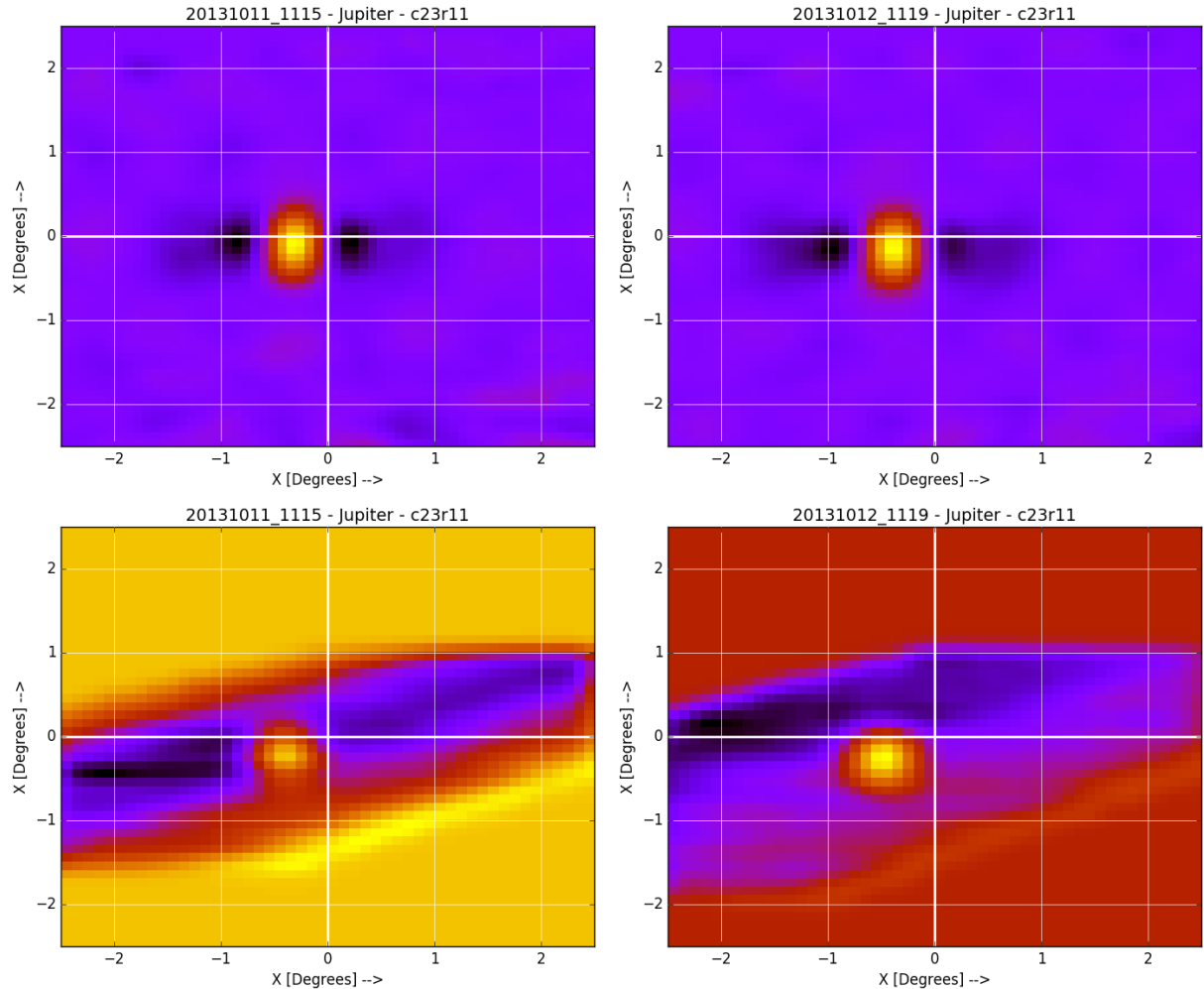


Figura 4.4: Maps in boresight coordinates of two Jupiter observations 20131011_1115 (left), and 20131012_1119 (right) with different mapping algorithms M2 (top), and M4 (bottom). Both the mapping algorithms return significant pointing offsets. The large pointing offsets are because of the issue with the ABS GPS.

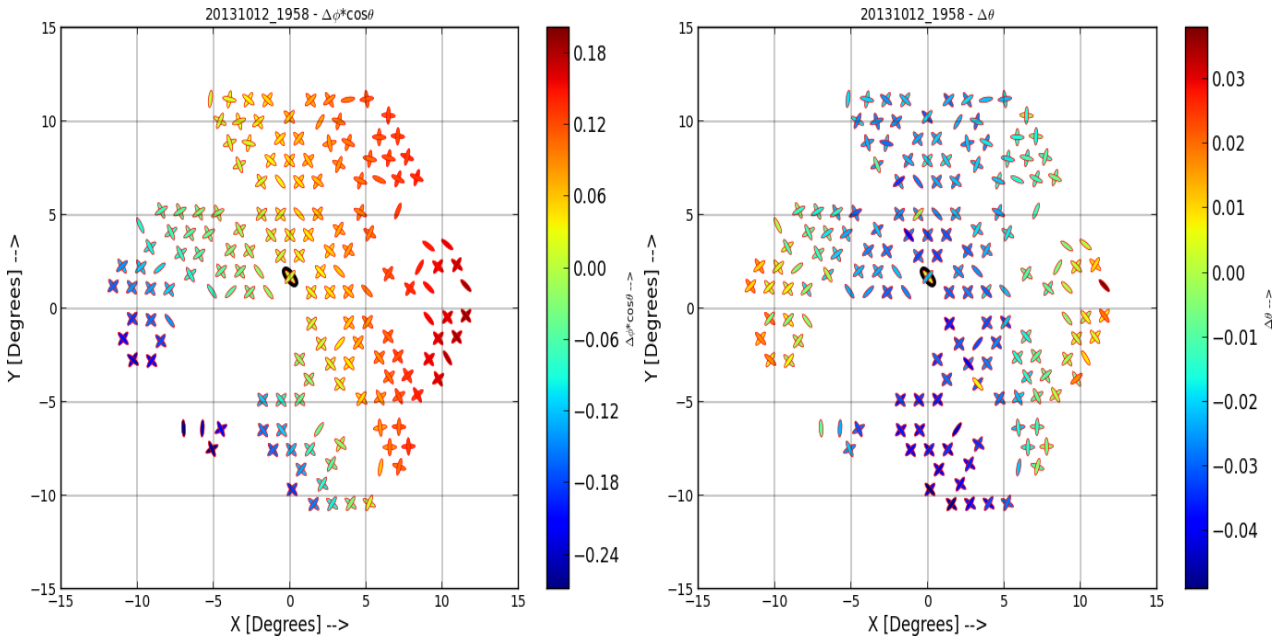


Figura 4.5: Detector offsets in degrees in the azimuthal ($\delta\phi \cos(\theta)$), and elevation ($\delta\theta$) shown in the left, and right panels for a wide Moon observation performed on 12 October, 2013. The offsets show a systematic error (gradient across the focal-plane) due to the faulty GPS.

Shift number	Date of shift	Δ_{shift} and direction	Number of days in potential problem	Exact date known	Closest point source observation		Remarks
					M - Moon; J - Jupiter before shift	after shift	
1	20120804 - 20120823	9° N	19	No	20120804 (M)	20120823 (M)	CMB data cut
2	20130601	7.8° E	0	Yes	20130530 (J)	20130812 (M)	No observations (poor weather)
2(a)	20130901	0.1° N	5	No	20130822 (M)	20130905 (J)	
2(b)	20130913	0.1° N	1	No	20130912 (M)	20130914 (M)	
3	20131004 - 20131014	N.A	10	Yes	20131004 (J)	20131013 (J)	GPS failure
4	20131104	1.2° N	1	Yes	20131103 (J)	20131104 (J)	-
5	20140707	35° N	1	Yes	N.A	20140705 (M)	Encoder breakage

Tabla 4.1: A timeline of ABS azimuth encoder slips, and faulty GPS issues during the three seasons of observations. The title of the columns give the obvious description about the columns. The entires in red colour correspond to the smaller shifts which are guessed from the pointing model. For these observations, the analysis pipeline will be run twice with, and without introducing the shifts.

4.3. “Ghost” images of bright sources

Occasionally (when performing wide Moon scans for the focal-plane pointing solution), we observed “ghost” images of the Moon. An example of this is shown in FIG. 4.6 captured with the detector c06r10 on July 28, 2012. The ghost image is enclosed by the white dashed circle on the map for clarity. While it was clear that these were reflected images of the “bright” sources that was being observed, the exact reason was not evident initially. Several factors were considered for producing the reflected ghost images *viz.* 1. HWP, 2. inside of the shiny baffle, 3. a ring present between the baffle, and the HWP. We performed several tests like blackening the baffle by using eccosorb (Electromagnetic absorbers) material, removing the baffle, removing the ring, stop the HWP from spinning, but the reflected images were still present in all the wide Moon observations.

The ghost images were quite faint with ≤ 3 per cent of the power as compared to the “real” Moon image and are sometimes comparable to the rms of the map. This made it quite difficult to model the ghosts. However, the model fitting improved by ignoring regions on the map with a poor SNR, and “visually” identifying realistic initial parameters. We were able to model ~ 30 per cent of the TES detectors in each observation. By using 2d-circular Gaussian models, the amplitudes, and the location of the ghost images were estimated. From the location of the ghosts, it was evident that they are the reflected images of the source from the rim off the feed horns onto which the detectors were planted. The rims are slightly (\sim five per cent) reflective. So when a detector with offsets (α, β) captures the Moon, its image

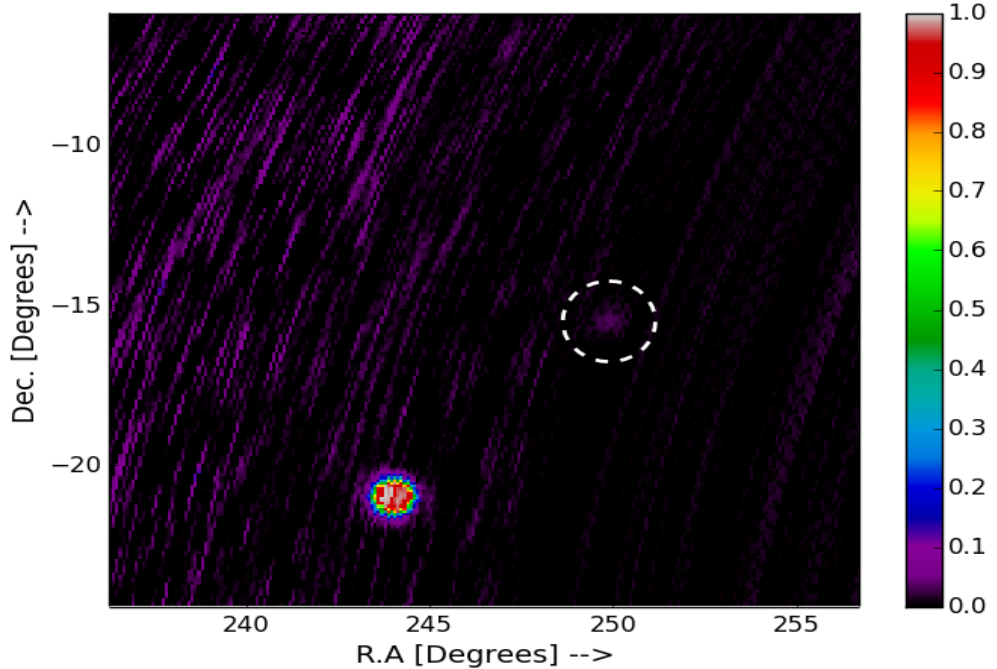


Figura 4.6: The ghost image of Moon enclosed by the white dashed circle from a wide Moon scan performed on July 28, 2012. The colour scale has been normalised to unity to show that the amplitude of the ghost is ≤ 5 per cent of that of the Moon. The map is shown in equatorial coordinates.

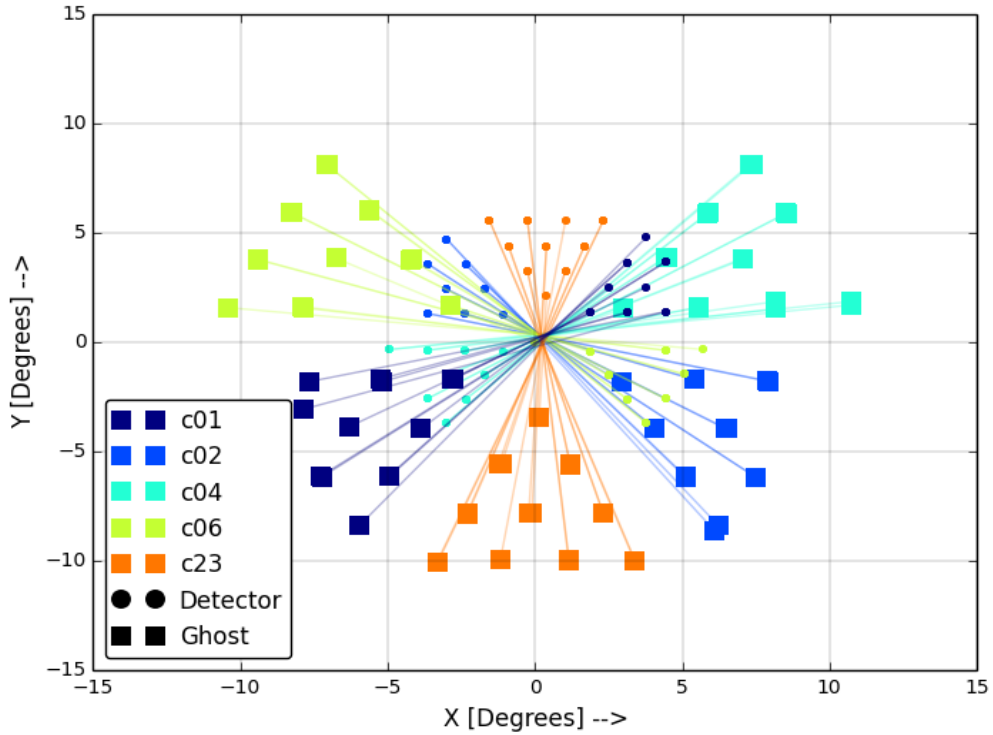


Figura 4.7: The location of the ghost images on the ABS focal-plane for selected detector columns (1,2,4,6,23) from a single wide Moon observation. The circles show the location of the detector α, β , and the bigger squares show the location of the ghost of the same columns (but at $-x\alpha, -y\beta$) which are reflections of the Moon from different detector columns. The exact value of x, y will depend on the region of the sky scanned, and the motion of the Moon during the observation time. It is clear from the plot that the ghost images are reflections of the source by the (rim of the) feed-horns. The colours just show different columns that are plotted.

is reflected off the rim of the feed horn, hits the secondary mirror, and is captured back by another detector at (α, β) on the focal-plane. FIG. 4.7 shows the location of the ghost images on the ABS focal-plane for selected detector columns from a single wide Moon observation.

The ratio of the amplitude of ghost to the Moon ($\frac{A_{\text{ghost}}}{A_{\text{Moon}}}$) is shown in FIG. 4.8 using the maps from three wide Moon observations during the months of July, and August in 2012. The ratio does not exceed ~ 3 per cent. No ghost images were seen in CMB scans as expected (or) in other point source observations. There is, however, a possibility to see ghost images of the Sun in scans performed at distances that were roughly equal to the field-of-view of ABS. But we never pointed the telescope very close to the Sun as that would heat up the HWP bearings leading to its stoppage. All our CMB field-A scans were performed far away from the Sun. A simple script checked for ghost images of the Sun in the CMB scans, and did not return any potentially affected observation. Based on the above results, we did not consider the ghost images for the process of data selection.

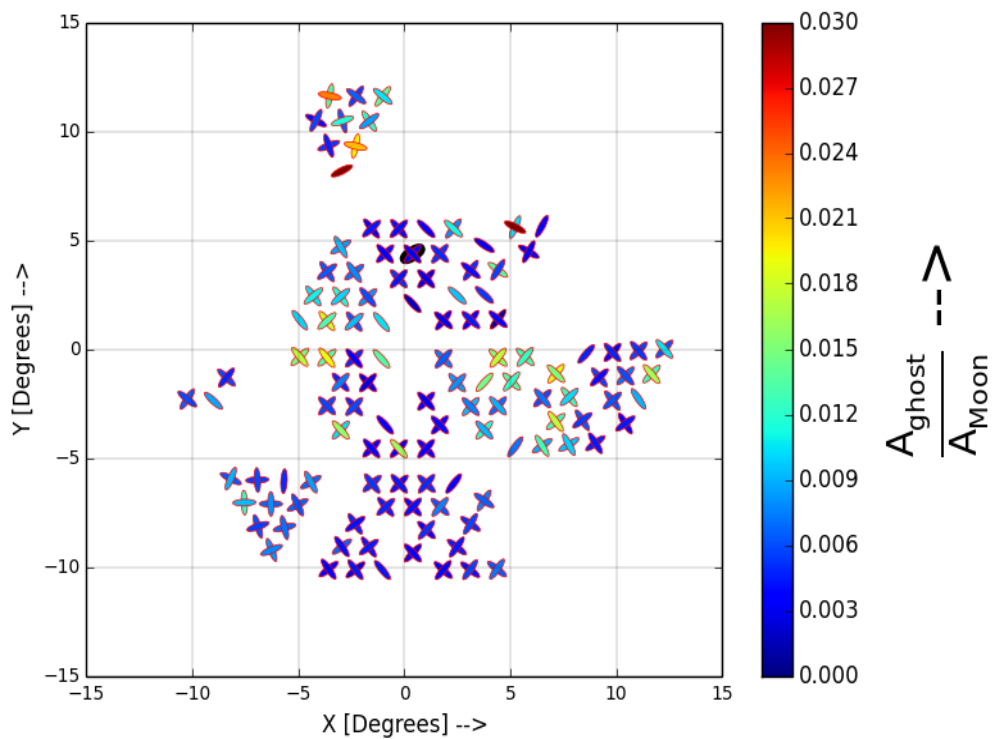


Figura 4.8: The ratio of the amplitude of ghost image to the Moon using three wide Moon observations from the first season. Only the detectors shown in the plot have a satisfactory Gaussian fits. The amplitudes of the ghost images are extremely low and does not exceed more than three per cent of the amplitude of the Moon. No ghost images were seen in the CMB scans, and other point source observations.

4.4. Correlated noise

After the preliminary data correction, and rigorous data cleansing *viz.* glitches, HWP ($A(\chi)$) signal, SSS, azimuth encoder slips, and faulty GPS we performed the data selection to get the good CESes, and the good TES detectors in each CES. The *inverse noise variance maps* of the Stokes parameters Q, U were made from the demodulated TODs using the technique mentioned in section 5.1, and the power spectrum was derived using the *Pseudo- C_l* estimator described in section 6.1. As part of the analysis procedure, we performed *null tests* to estimate the systematics by estimating power spectrum from the maps made out of two subsets of data as described in section 6.2. The difference between the power spectrum from the two subsets should be consistent with a null power spectrum if there are not any systematic errors present in the data or introduced as artefacts during any of the analysis steps.

We analyse the null power spectrum in 13 multipole ℓ bins quantitatively using χ^2 statistics and believe in our results only when the null tests pass certain criteria. For ABS, most of the null tests failed particularly at the low ℓ bins which is the region of interest because the tensor power spectrum peaks at low ℓ , and then decays. The null test failure indicated presence of systematic errors that dominated on large-scales despite the exceptional performance of the HWP in removing the large unpolarised atmospheric signals.

To investigate the reasons for the null test failure on large-scales we computed the covariance between different TES detectors for each CES and used *Eigen decomposition* techniques to find the dominant modes that affect the data quality. This was motivated by the results of ACT experiment [57]. The idea is to remove these dominant modes from the data and repeat the null tests using the cleaned data. Since we are worried only about the large-scale features this method is appropriate.

4.4.1. Decomposition technique and mode finding

The covariance matrix Σ was computed from the demodulated TODs of all passed detectors. The Σ contains information about $\text{cov}[I_i, Q_j]$, $\text{cov}[I_i, U_j]$, and $\text{cov}[Q_i, U_j]$ where i, j are two different detectors, and I, Q , and U correspond to the Stokes parameters. Thus, the dimension of the covariance matrix of a particular CES would be $3N \times 3N$ where N is the number of passed TES detectors in that CES. We ignore the I information since we are only interested in the polarisation information and so Σ will have dimensions $2N \times 2N$. The Σ was calculated in four different frequency bands *viz.* $(0 \geq f < 2 \text{ mHz})$, $(2 \leq f < 5 \text{ mHz})$, $(1 \geq f < 1.5 \text{ Hz})$, and $(9 \geq f < 9.9\text{Hz})$. The gaps in the bands correspond to the likely presence of features due to scan frequency, and HWP harmonics. For this study, we only focus on the bands $0 \geq f < 5 \text{ mHz}$ that corresponds to the large-scales and it is also the region that will be dominated by $1/f$ noise.

Just to visualise the amount of correlation between different detector data, FIG. 4.9 shows the *correlation matrix* for two passed CESes 2082.0 (left), and 2176.2 (right) from the CMB field-A observations during the first season. The plots show the correlation between the Q ,

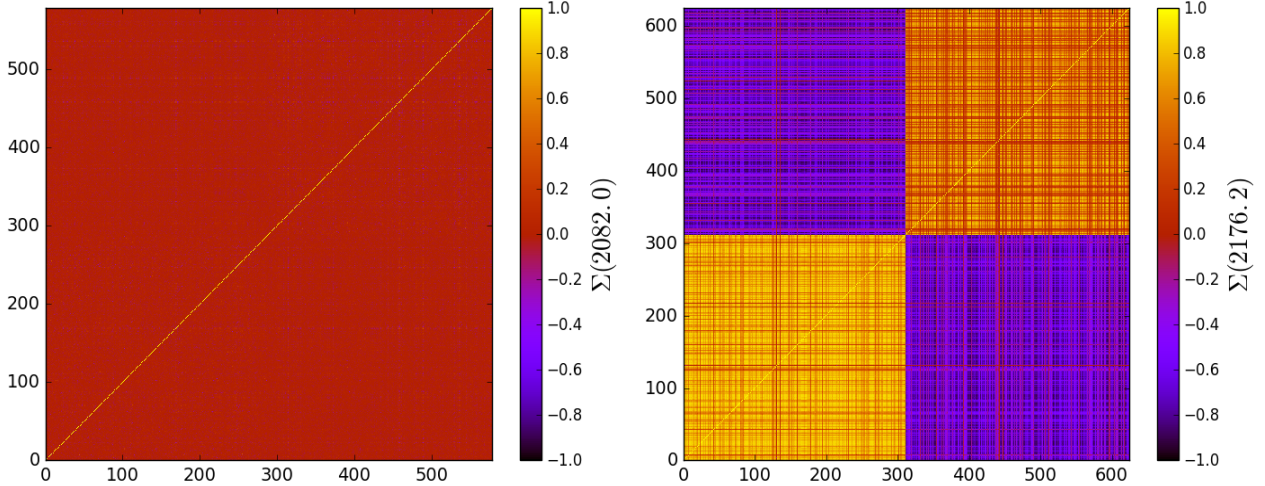


Figura 4.9: Correlation matrices of the Q , and U Stokes parameters for the 2082.0 (left), and 2176.2 (right) CESes from the first season of CMB field-A observations. The correlation matrix of CES 2086.0 (left) looks normal while the 2176.2 (right) reveals the presence of a strong correlated noise component.

and U Stokes parameters for the detectors that passed the cuts. The strong correlation across the entire detector array in the right panel indicates the presence of correlated noise in the CES 2176.2. Such strong correlation is absent in the CES 2082.0 (left). Most of our CMB field-A data look like the figure in the left panel.

Using Singular Value Decomposition (SVD), we decompose the covariance matrix of each CES into their eigenvalues, and the eigenvectors. An exhaustive review of the SVD technique for CMB data analysis can be found in [58]. Mathematically the decomposition can be described as

$$\Sigma_{M \times N} = U_{M \times M} S_{M \times N} V_{N \times N}^T \quad (4.2)$$

where $U_{M \times M}$, and $V_{N \times N}^T$ are unitary matrices, S is a diagonal matrix with the specified dimensions. In our case since Σ is a symmetric Hermitian matrix, the case is a lot simpler. The eigenvectors can be obtained from V^T , and S^2 will form the eigenvalues of Σ . While SVD is more powerful, in the special case of Σ being a symmetric Hermitian matrix, a simple Eigen decomposition technique can be used instead of the SVD. We used the *linear algebra* package available in `python scipy` for this purpose.

The dominant modes in the Σ can be obtained using the linear combination of the entries from the (demodulated) TOD matrix weighed appropriately. For example, the mode m_i can be obtained as

$$m_i = D_{2N \times 2N} \times U_i \times H \left[\lambda_i - \xi \sum_{j=1}^n \lambda_j \right] \quad (4.3)$$

Normally, the TOD matrix $D_{n_s \times N}$ can be formed by stacking the TOD (d_{n_s}) with n_s time samples¹ from different TES detectors as $[d_1, d_2, \dots, d_N]$. When using the demodulated data,

¹We down sample our data to 1 Hz from 200 Hz for this study only for computation reasons.

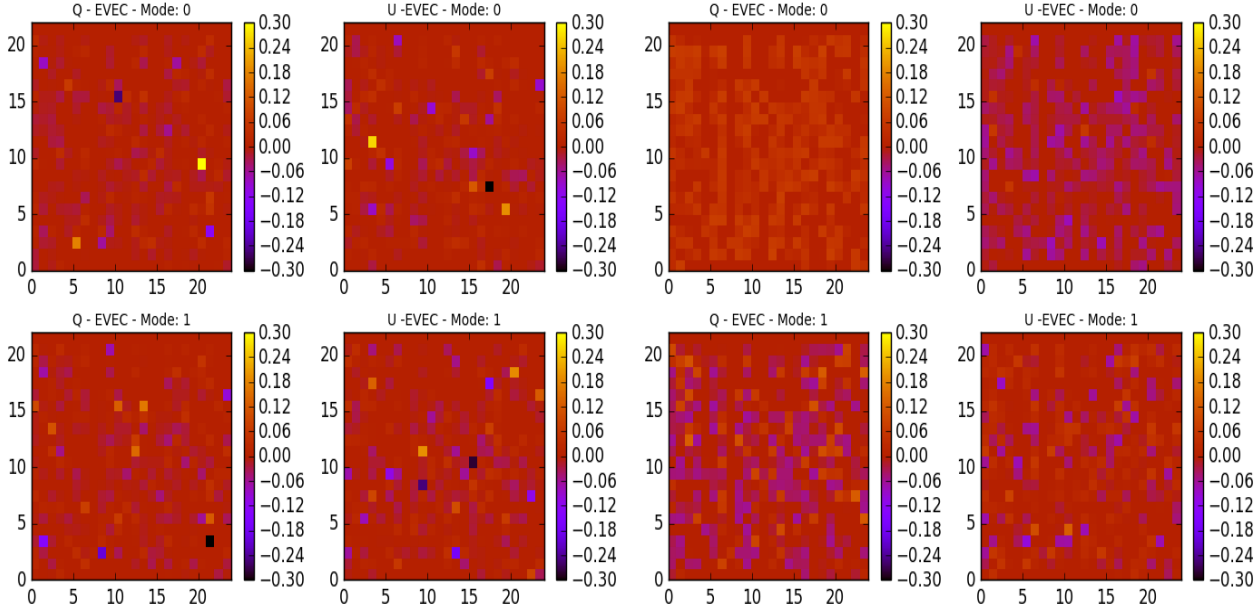


Figura 4.10: Q, and U eigenvectors of the first two dominant modes for the 2082.0 (left), and 2176.2 (right) CESes obtained using the SVD.

we form \mathbf{D} as

$$\mathbf{D}_{n_s \times 2N} = [\text{Re}(d_1), \text{Im}(d_1), \text{Re}(d_1), \text{Im}(d_2), \dots, \text{Re}(d_N), \text{Im}(d_N)]$$

As already mentioned in section 2.5, the real and imaginary parts of the demodulated TOD represent the Q, and U Stokes parameters. The weight for the data from each detector for the linear combination is given by the eigenvector \mathbf{U}_i for the respective mode i . The last term in Eq. 4.3 represent the Heaviside step function to pick only the dominant modes. Dominant modes are those with eigenvalues λ_i greater than the threshold $\xi = 10$ times the average of all the eigenvalues.

The eigenvectors of the first two dominant modes calculated using Eq. 4.2 are shown in the Fig. 4.10. The four plots in the left, and right panels correspond to Q, and U eigenvectors of the first (top), and second (bottom) dominant modes for the two CESes 2082.0, and 2176.2, respectively. The figure shows that the noise modes of 2082.0 (left) is due to just \sim four detectors behaving badly. For the 2176.2 (right) several detectors contribute equally to the modes revealing the presence of correlated noise in the data.

The TOD of the first six dominant noise modes, calculated using Eq. 4.3 as the linear combinations of the TOD matrix weighed by eigenvectors for the above two CESes are shown in Fig. 4.11 along with their power spectra. The CES 2082.0 (left) shows the presence of structure in its first three noise modes after which the modes become white noise dominated. The CES 2176.2 (right) also contains structures in its first two modes (or even up to mode 6). However, the noise modes in CES 2082.0 are dominated by few detectors behaving badly (left panel of FIG. 4.10) as opposed to 2176.2 where several detectors are equally affected (right panel of FIG. 4.10). From these results we conclude that the CES 2176.2 is strongly dominated by some kind of correlated noise across the entire detector array. We perform the above mentioned process to all the passed CESes of the CMB field-A observations.

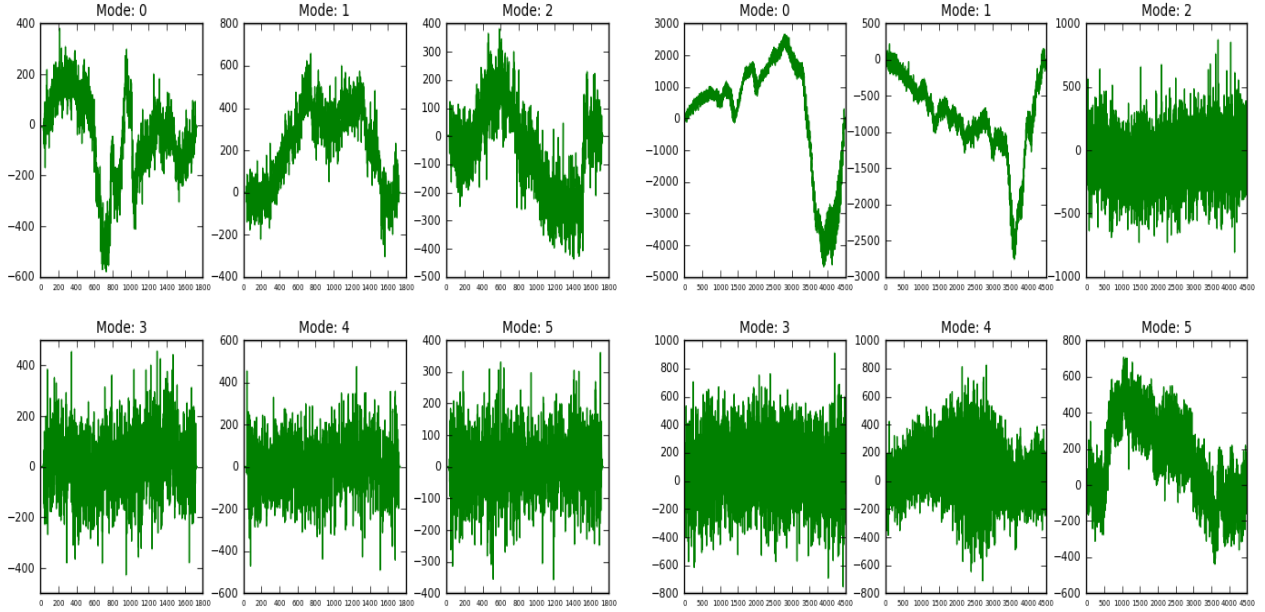


Figura 4.11: The first six dominant modes for the 2082.0 (left), and 2176.2 (right) CESes calculated using EQ. 4.3. The units are aW . The TODs have been down sampled to 1 Hz, and the horizontal axis correspond to the data values at each second. The first few modes of both the CESes show the presence of structure of $1/f$ noise although only the 2176.2 CES contain the correlated noise component. See text for more details.

4.4.2. Affected CES data sets

We first analysed a subset of data containing 153 CESes from the first season. The noise modes were calculated and 30 CESes were flagged for the strong correlated noise component upon visual inspection of the eigenvectors, and the TODs and the power spectra (not shown in the above figures) of the dominant noise modes. The power spectra of the noise modes and the detector TODs are modelled using Eq. 4.1. As expected, the 30 affected CESes have a higher f_{knee} compared with the other normal CESes. The results of the $1/f$ model fitting are shown in FIG. 4.12. The top (bottom) panel correspond to the distribution of the f_{knee} of the detector TODs of the CES affected (not affected) by the correlated noise component.

Next, we developed an automatic detection algorithm that bypasses the visual inspection step. This only uses the correlation matrices of the demodulated detector TODs to estimate the presence of the $1/f$ noise component. The details of the algorithm are mentioned in Appendix B. Before running the auto detection algorithm on the full list of season 1 data, we made sure that it recovers the visually flagged bad data. After this confirmation, we ran it on the full season one data. There are only 33 CESes with a strong correlated noise component. The f_{knee} of the detectors for the full season one data is shown in FIG. 4.13. The figure is same as FIG. 4.12. Since less than ten per cent of our data have this strong correlated noise component, we decided to remove the affected CESes from further analysis. Because of this small fraction we did not try to recover the good data by remove the dominant modes from them. But for reference the details of the mode removal procedure and the source of the correlated are described in Appendix B.

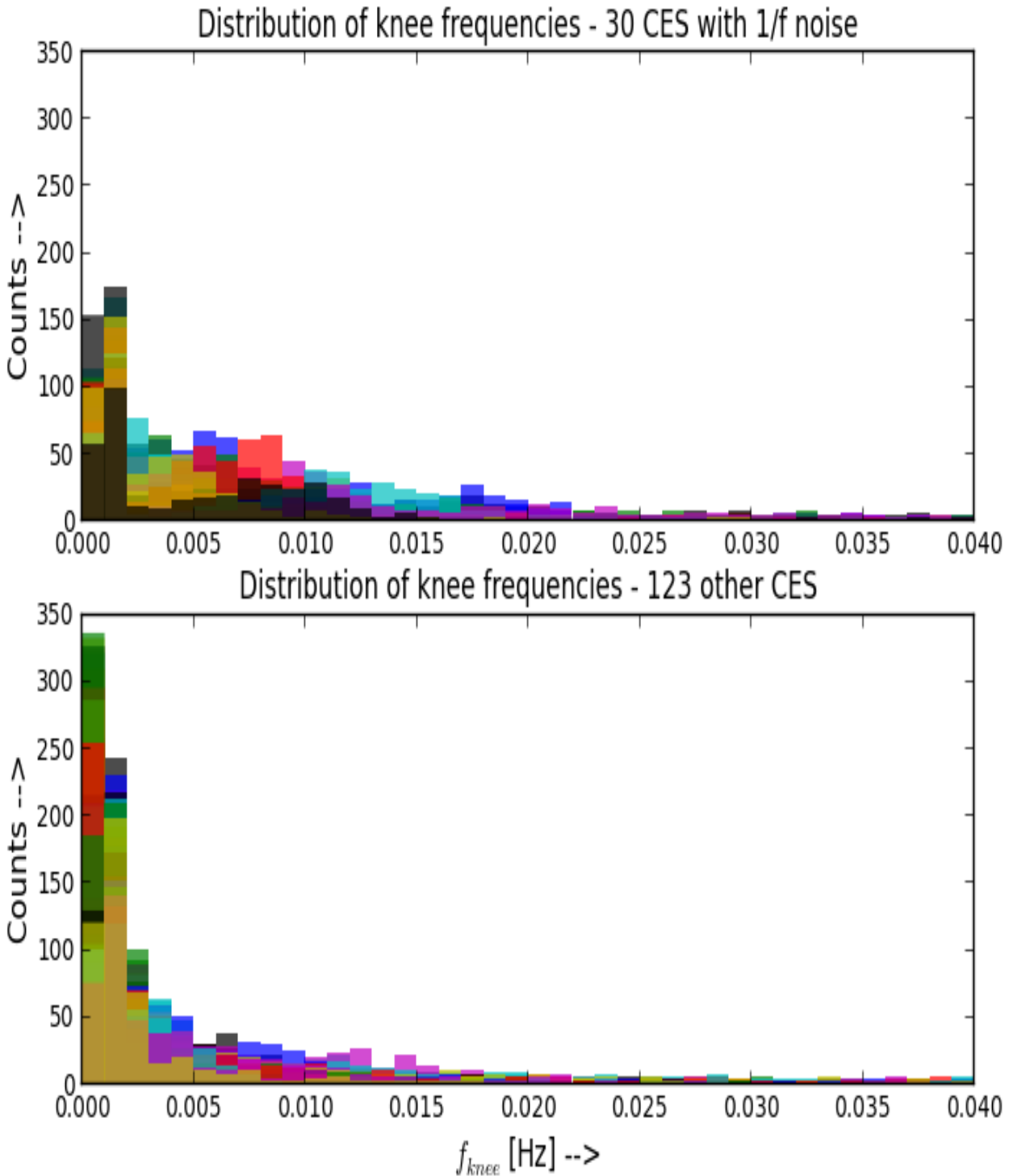


Figura 4.12: The distribution of f_{knee} of the detector TODs for the 30 affected CESes in the top panel, and the normal CESes in the bottom panel. Clearly, the bad detectors in the affected CES have a higher f_{knee} .

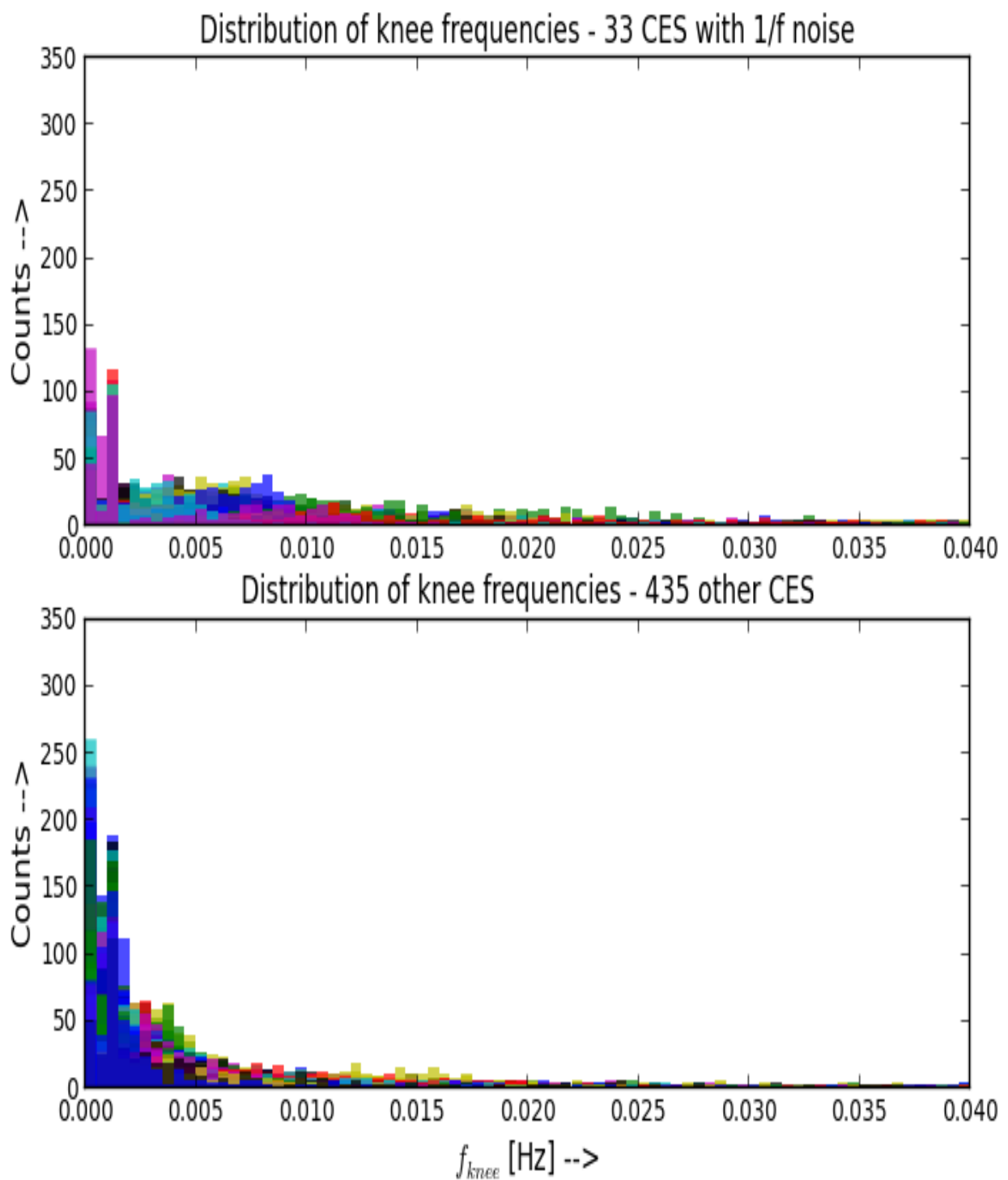


Figura 4.13: Same as FIG. 4.12 but for all the CESes from the first season. The affected CESes were identified using the automatic detection algorithm described in Appendix B.

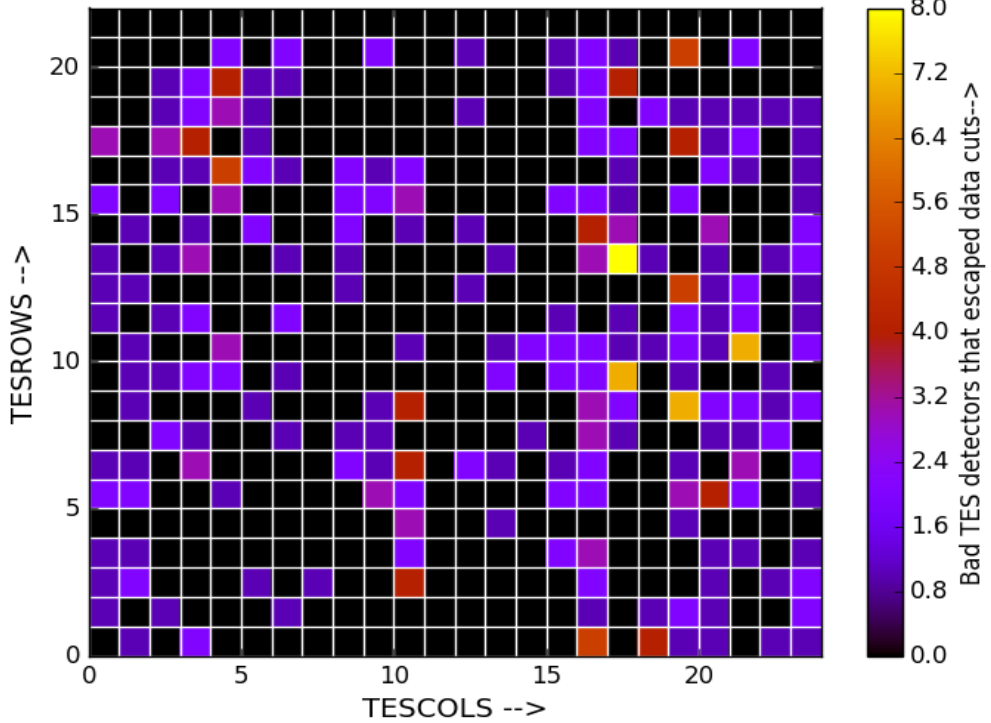


Figura 4.14: The number of CESes in which a particular detector behaves badly after all the data cuts. See EQ. 4.4 for more details.

4.4.3. Bad TES detectors that escaped data cuts

Finally using the above method we checked if a particular detector behaves consistently bad during several observations. Note that for this study we only picked the TES detectors that passed the data cuts, and no consistent bad behaviour of a particular detector is expected. Having the eigenvector for all the dominant modes in each CES, we flag a detector as bad if its contribution (eigenvector of the detector) to the mode is significantly different from the other detectors (median value of the eigenvectors of all detectors). This is shown in EQ. 4.4 where F_i is the flag set for a bad detector i for a particular CES, U_{ij} is the value of the eigenvector corresponding to detector i in mode j , \tilde{U}_j is the median value of eigenvectors corresponding to all detectors in mode j , $\xi = 3.5$ is the threshold used, and σ_{U_j} is the standard deviation of the eigenvectors of mode j . We set F_i^{CES} to one if the detector is flagged in at least one mode j . We compute the total $F_{\text{TES}}^{\text{tot}}$ for each detector in all CES and the result is shown in 4.14. The colour scale in the figure corresponds to the number of CES in which the detector has been found bad using the procedure outlined above. Considering the maximum number of CESes in which a detector behaved badly after all the data cuts is only eight, we do not flag these detectors as bad for the further analysis pipeline.

$$F_i^{CES} = \begin{cases} 1; U_{ij} - \widetilde{U}_j \geq \xi \sigma_{U_j}; 0 < i \leq N_{dets}; 0 < j \leq M_{modes} \\ 0; \text{otherwise.} \end{cases} \quad (4.4)$$

$$F_{TES}^{tot} = \sum_{c=0}^{N_{CES}} F_{TES_c} \quad (4.5)$$

4.5. Far-side lobe study

The side lobes are the signals received from undesired directions in a radio telescope. In the radiation pattern of a radio telescope, while the main lobe contains the maximum power some of the power go into these side lobes. The lesser the side lobe level, the better is the performance as it reduces interference due to unwanted signals from contaminating the observation. Note that the side lobes can never be completely eliminated. The contamination can either be

- *near-side lobes* that are generally minimised by using corrugated feed horns and tapering the main beam. The ABS telescope uses corrugated feed horns and the incoming signal is apodized by a cold aperture stop above the HWP. The near-side lobes of the ABS telescope is well characterised and will be reported in [12].
- *far-side lobes* that are sometimes difficult to detect. Many CMB experiments have reported a significant contamination due to ground pick up, and other bright sources aligned with their far-side lobes [59, 60, 61]. The spurious signals from far-side lobes are commonly reduced by using ground screens around the telescope. For ABS, we except a very low far-side lobe contamination as a ground screen was deployed during the initial stages of observations. The blue metal surrounding the cryostat in the right panel FIG. 2.2 is the ground screen.

To model the far-side lobes of ABS, we performed eight long duration scans of the brightest source available, *the Sun*, and called them the *Sun side lobe scans (SSL)*. The telescope was pointed to zenith, and scanned the entire permitted (by limit switches) azimuth range ($0^\circ \lesssim \phi \lesssim 360^\circ$) for close to four hours as the Sun was rising in elevation. Using this scan strategy, the main beam (detectors) of the telescope will never look directly at the Sun but the contamination due to the alignment of any of the far-side lobes with the Sun will show up as a prominent signal in the detector TODs. The location of the far-side lobe (ϕ_{fsl}, θ_{fsl}) will be the coordinates of the Sun at the respective time of hit. A detailed analysis of the SSL scans is currently ongoing, and I discuss the necessary frame work here.

The SSL scans are mapped in a coordinate system relative to the position of the Sun. Let us denote the azimuthal, and the elevation angles of this coordinate system using capital greek letters as Φ, Θ respectively. In this coordinate system, the Sun is always located at $(\Phi_\odot, \Theta_\odot) = (0, 0)$ degrees. Given the position of Sun $(\phi_\odot, \theta_\odot)$ and the detector (ϕ_d, θ_d) at any given time [59, 62, 63]

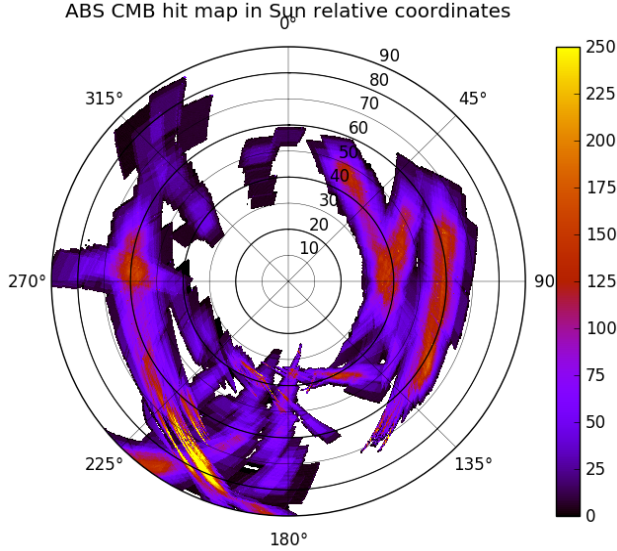


Figura 4.15: The total observation time in minutes of the ABS scans in the Sun relative coordinate system. Only the CESes when the Sun was above the horizon have been used here.

$$\begin{aligned}\vec{\odot} &= \cos\phi_{\odot} \cos\theta_{\odot} \hat{x} + \sin\phi_{\odot} \cos\theta_{\odot} \hat{y} + \sin\theta_{\odot} \hat{z} \\ \vec{d} &= \cos\phi_d \cos\theta_d \hat{x} + \sin\phi_d \cos\theta_d \hat{y} + \sin\theta_d \hat{z}\end{aligned}\quad (4.6)$$

the position of the detector Φ_d, Θ_d in the Sun relative coordinate system is defined as the following. The elevation angle Θ_d is the arc cosine of the dot product of the Sun, and the detector vectors. To obtain the other angle Φ_d , a reference vector $\vec{r} = \vec{d}^\perp$ in the plane perpendicular to \vec{d} must be defined. The azimuthal angle Φ_d will be measured eastwardly from this reference orientation. Of course, there are infinite ways of defining this reference d^\perp vector \vec{r} but since we want the distance of Sun from the detector we define it as

$$\vec{d}^\perp = \vec{r} = \cos\phi_d \cos(90 - \theta_d) \hat{x} + \sin\phi_d \cos(90 - \theta_d) \hat{y} + \sin(90 - \theta_d) \hat{z}$$

From the above definitions, and $\vec{s} = \vec{d} \times \vec{r}$,

$$\Phi_d = \tan^{-1} \frac{(\vec{\odot} \cdot \vec{s})}{(\vec{\odot} \cdot \vec{r})} = \tan2 (\vec{\odot} \cdot \vec{s}, \vec{\odot} \cdot \vec{r}) \quad (4.7)$$

$$\Theta_d = \cos^{-1} (\vec{\odot} \cdot \vec{d}) \quad (4.8)$$

If a significant contamination from the far-side lobes (Φ_{fs1}, Θ_{fs1}) is detected for the SSL scans, then an additional data cut must be employed for the CMB scans. For this, the CMB maps will be made in this Sun relative coordinate system, and the data at the location of the far side lobes (Φ_{fs1}, Θ_{fs1}) will be cut. FIG. 4.15 shows the hit map of the ABS scans from all the four fields in the Sun relative coordinate system. Only the CESes where $\theta_{\odot} \geq 0^\circ$ have been used here. The colour scale indicates the total observation time in minutes. The hit maps for each of the fields is also shown separately in FIG. 4.16. We have not noticed any such contamination on the CMB maps as expected because of the presence of the ground screen but a thorough study will nevertheless be performed using the SSL scans.

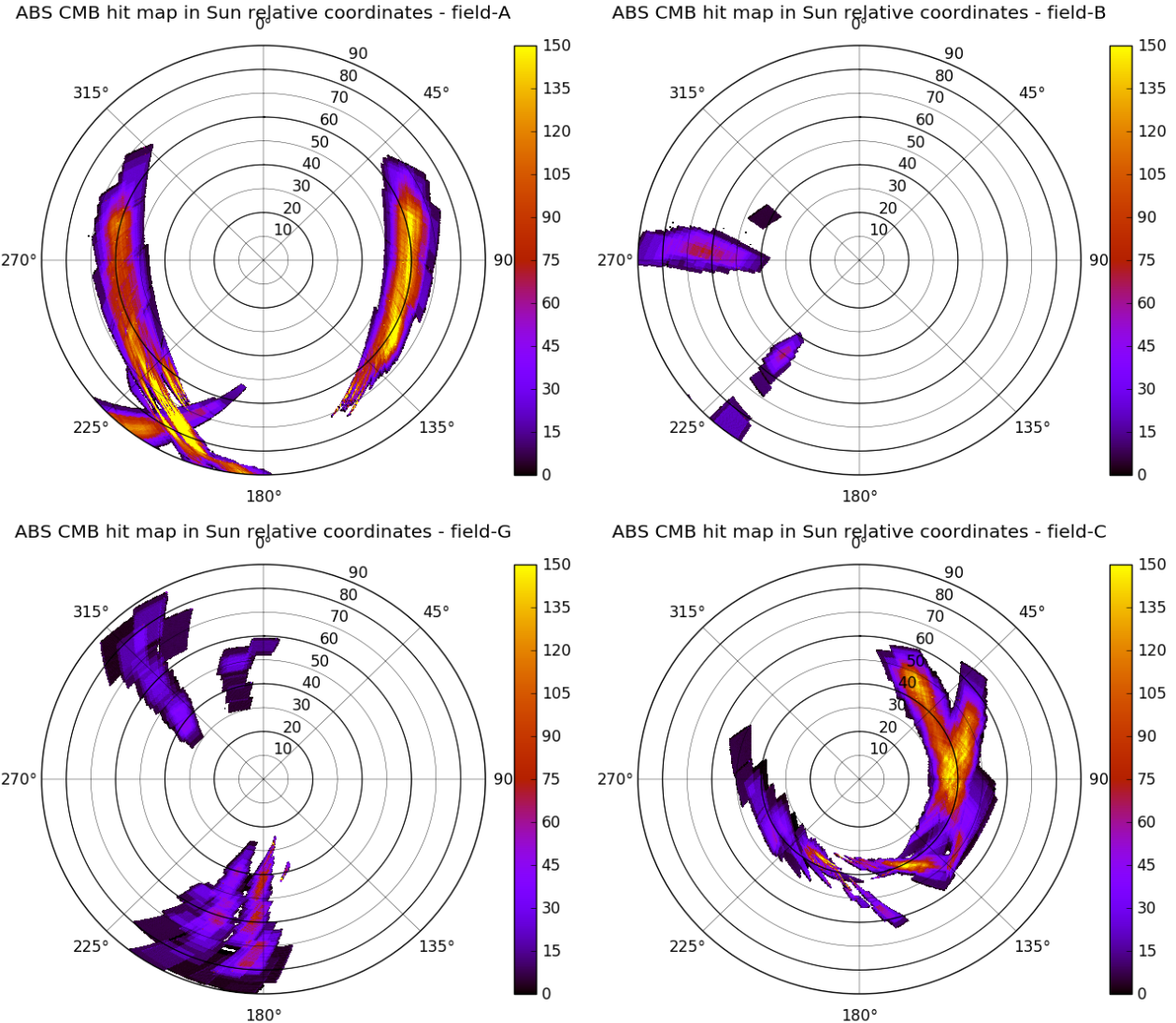


Figura 4.16: The total observation time in minutes of the ABS scans from the each field individually in the Sun relative coordinate system. Only the CESes when the Sun was above the horizon have been used here.

Capítulo 5

CMB MAP MAKING

Overview, and goals:

This chapter deals about the maps of the Stokes parameters for ABS after picking the good data sets using the techniques mentioned in the previous chapter. The maps are inverse noise variance maps and generated by Akito Kusaka. My work focussed primarily on the generating masks of bright point sources that can potentially bias the power spectrum measurement. The point source catalogues generated by Planck, and WMAP satellites have been used for this work.

5.1. CMB maps

Using the data cuts and selection criteria discussed in the previous section the TODs can be converted into sky maps using the information from the encoders. The optimal equation to obtain the sky map \mathbf{m} from a detector TOD \mathbf{d}

$$\mathbf{d}_t = \mathbf{P}_{ts} \mathbf{m}_s + \mathbf{n}_t \quad (5.1)$$

where \mathbf{P} is the pointing matrix and contains information about the sky pixel at which a particular TOD sample is pointed, and \mathbf{n} is the Gaussian random “uncorrelated” noise in the measurement with zero mean and noise covariance $\mathbf{N} = \langle \mathbf{n} \mathbf{n}^T \rangle$. The dimensions are: $\mathbf{d} - > (t \times 1)$, $\mathbf{P} - > (t \times s)$, $\mathbf{m} - > (s \times 1)$, $\mathbf{n} - > t \times 1$. Assuming that the sky map is convolved with the experiment’s beam, a given time sample only (first row of \mathbf{P}) will have a one in the column corresponding to the particular sky pixel observed. Using matrix notations, EQ. 5.1 can be reduced to obtain the optimal solution for \mathbf{m} as

$$\mathbf{P}^T \mathbf{N}^{-1} \mathbf{P} \mathbf{m} = \mathbf{P}^T \mathbf{N}^{-1} \mathbf{d} \quad (5.2)$$

Obtaining \mathbf{m} from EQ. 5.2 is a very slow process because of matrix inversion that has dimensions governed by the large number of data samples and sky pixels involved $\mathcal{O}(10^7)$. While some algebraic techniques can be used to obtain \mathbf{m} [29, 57], the process is still slow particularly as we will see in section 6.2 where we will make large number of maps for validating

the analysis and systematic checks. Instead, we will make naïve maps and weigh each time sample using the detector white noise level. Not surprisingly, these maps are called *inverse noise variance maps*.

Before going into the explanation of *inverse noise variance* maps, I will explain a simple *inverse variance mapper*. Using HEALPix pixelization¹ with a resolution 0.22° characterised by the parameter $n_{\text{side}} = 256$ the value of a particular map pixel m_j where $j \in (1, 12 \times n_{\text{side}}^2)$ in a CES is given by

$$m_j^{\text{CES}} = \sum_{i=1}^n d_i \delta_{p_{ij}} \quad (5.3)$$

where the *Kronecker delta* will be $\delta_{p_{ij}} = 1$ when a particular time sample was pointed p_i was pointed at the sky (HEALPix) pixel j and zero otherwise. The final value of a particular sky pixel m_j is just the sum of the contribution from different CES weighted by the standard deviation of them as given by EQ. 5.4

$$m_j^{\text{final}} = \frac{\sum_{i=1}^{N_{\text{CES}}} \frac{m_j^i}{\sigma_j^2}}{\sum_{i=1}^{N_{\text{CES}}} \frac{1}{\sigma_j^2}} \quad (5.4)$$

The only issue with this concept is that all the detectors get an equal weight (i.e.) some detectors perform marginally to pass the data selection and should receive a lesser weight than the detectors that behave well. Moreover, since the detectors are white noise dominated (Gaussian random distribution) the performance of a particular detector will not be constant in all the CES. This requires for a dynamical weighting mechanism based on the level of the white noise of a detector in a particular CES and it is called the *inverse noise variance* technique. So the EQ. 5.3, 5.4 are now modified to make the inverse variance maps as given below:

$$\begin{aligned} m_j^{\text{det,CES}} &= \sum_{i=1}^n \frac{d_i}{\sigma_{\text{det}}^2} \delta_{p_{ij}} \\ m_m_j^{\text{det,CES}} &= \sum_{i=1}^n \frac{1}{\sigma_{\text{det}}^2} \delta_{p_{ij}} \end{aligned} \quad (5.5)$$

where n is the number of time samples in the CES, m is the map, and mm is the covariance. Since the weighting factor is dynamic now, EQ. 5.5 can be used to make maps of multiple detectors from multiple CES individually and so EQ.5.5 can be simplified further as

$$m_j^{\text{final}} = \sum_{a,b,c} \frac{\frac{d_j^{a,b,c}}{\sigma_{a,b}^2}}{\frac{1}{\sigma_{a,b}^2}} \delta_{p_{a,b,c,j}} \quad (5.6)$$

¹HEALPix map pixels are normally vectors and there is an one-one mapping between the vector elements and the sky map.

where a, b indices run over number of detectors, and CES respectively (i.e.) $d_j^{a,b,c}$ is the c^{th} time sample of detector a in the CES b observing the j^{th} pixel. In all the above equations d represents the temperature measured by the detector.

To make polarisation maps, we must include the information about the parallactic angles, and the maps of Q, U in EQ. 5.6 will include the $\cos(2\gamma_{a,b,c}), \sin(2\gamma_{a,b,c})$ terms respectively. The covariances QQ, UU will include the square of these two terms. The angle $\gamma_{a,b,c}$ is the parallactic angle of detector a in the CES b at the c^{th} time sample.

5.2. Masking point sources

As explained in section 2.3.1, the ABS scan fields are located in the region of minimal foreground emission from our Galaxy. But a potential source of contamination to the CMB data are the point sources that are present in the ABS scan regions. These sources can be extragalactic radio compact objects, the Galactic Cold Clumps, and the synchrotron emitting diffuse sources. A particularly bright radio source is called the *Pictor A* which is a radio galaxy and is located at the edges of the ABS main CMB field-A.

To ensure that the point sources do not affect our results, we performed a systematic study by computing the polarisation power spectrum with, and without masking the point sources. While many of the point sources are weakly polarised, and can only be detected in the intensity maps, it is necessary to carry out this approach because of the following reasons.

- Any temperature to polarisation leakage in the ABS detectors would lead to an excess in the polarisation maps near the point source locations. This could indeed be the case for the weaker polarisation signal observed by Planck along the Galactic plane as compared to QUIET, and WMAP (see Fig. 7 of [68] for more details).
- And, finally the source could be highly polarised like Pictor A (see section 5.2.2).

5.2.1. External point source catalogues

We initially used several catalogues of point sources detected both in temperature, and polarisation experiments published by *viz.* Australian Telescope 20 GHz (AT20G) survey [69], ACBAR [70], ACT [71], Planck [72], SPT [73], and WMAP [74]. Of all the above experiments, only Planck and WMAP being the whole sky surveys, have homogeneous common sky coverage with ABS. Obtaining point source masks using other experiments could bias our results by masking some regions severely compared to others. The vast frequency coverage of Planck, and WMAP experiments is also complementary to this study. Thus after detailed considerations, we chose to derive point source masks only from the WMAP, and Planck source catalogues.

The *WMAP Five-Band Nine-Year point source catalogue*² contain fluxes, and the spectral

²[hdp://lambda.gsfc.nasa.gov/product/map/dr5/ptsrc_catalog_get.cfm](http://lambda.gsfc.nasa.gov/product/map/dr5/ptsrc_catalog_get.cfm)

indices of ~ 272 sources measured in 5 frequency bands in the range 23 to 93 GHz. We used the W-band (94 GHz) sources for this current work with the source amplitudes scaled to ABS' central frequency of 145 GHz by

$$A_{\nu_1} = C A_{\nu_2} \quad (5.7)$$

$$C = \left(\frac{\nu_2}{\nu_1} \right)^{\beta} \quad (5.8)$$

where β is the spectral index of the source.

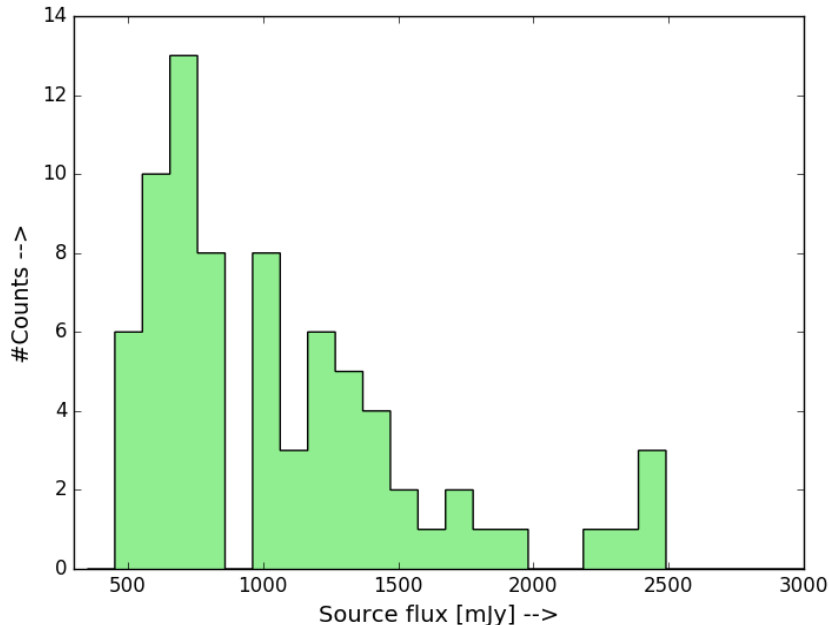


Figura 5.1: The flux distribution of sources from Planck P₁₄₃, P₃₅₃, P_{GCC}, and WMAP point sources catalogues that lie on the ABS field-A. A flux threshold of 500 mJy has been applied. There are 208 sources in total.

For Planck, we used the source catalogues³ in the frequency bands 143 GHz P₁₄₃, 353 GHz P₃₅₃, and the Cold cores catalogue P_{GCC}. Together, P₃₅₃, and P_{GCC} have 330 sources on the ABS field. Unlike WMAP, no spectral index information was available for the sources in P₃₅₃, and P_{GCC} to scale their amplitudes from 353 GHz 143 GHz. Hence, I ignore these sources for the current work. The P₁₄₃ contains 290 sources on the ABS field. However, owing to the poor SNR of majority of the Planck sources for this work only pick the sources that are above a threshold of 500 mJy are picked. After applying this flux cut, and picking unique sources, we were left with 80 sources with 66 unique map pixels (on a HEALPix map with nside = 256) to be masked. The flux distribution of the 80 sources are shown in FIG. 5.1. This work is currently ongoing, and the flux threshold used can slightly vary based on a more careful inspection of the SNR of Planck sources.

³http://irsa.ipac.caltech.edu/data/Planck/release_2/ancillary-data/

5.2.2. PicA galaxy

Pictor A (PicA) located at ($\alpha, \delta = 79.95, -45.77$ degrees) is a bright jet radio galaxy and has been observed and studied by several experiments both in temperature, and polarisation [75, 69, 76] and reference within. It is quite bright in temperature with a flux density of $\sim 6320 \pm 100$ mJy as measured by the Australia Telescope 20 GHz (AT20G) survey [69]. In polarisation, it has been detected by both AT20G, and QUIET [76]. The source has been resolved into the central nucleus and two lobes (eastern, and western). While the nucleus is the brightest in temperature, the western lobe is the brightest in polarisation with $\sim 423, 205, 89$ mJy at 20 [69], 41 and 94 [76] GHz respectively. Because of its brightness, it is a prominent source of contamination for many CMB experiments in the southern hemisphere. Further from combining measurements from several experiments, the thermal spectrum of the PicA can be fit by power law with a slope $\beta = 0.85$ in the radio frequency range $0.4 \leq v \leq 5$ GHz [75]. I have used this spectral index value to estimate the brightness of PicA in the ABS frequency $v_{\text{ABS}} = 145$ GHz as shown above in EQ. 5.7. We do not see the PicA galaxy on our maps as the temperature of PicA at 145 GHz is $\sim 1 \mu\text{K}$, and comparable to the noise in our map. FIG. 5.2 shows the region (in equatorial coordinates) around PicA from the ABS Q, U maps in the top panel. The same region from Planck 143 GHz channel is shown (in galactic coordinates) at the bottom panel for comparison. Both maps have been smoothed to an FWHM of 32.4 arcmins. The presence of PicA is not obvious in the Planck 143 GHz maps.

The calculations to convert the source brightness S [Jy/Sr] to temperature units T [K] is also shown below in EQ. 5.11.

$$S \left[\frac{\text{Jy}}{\text{sr}} \right] = \frac{2kT}{A_e} \left[\frac{\text{m}^2 \text{ kg s}^{-2} \text{ K}^{-1}}{\text{m}^2 \text{ sr}} \right] \quad (5.9)$$

$$S \left[\frac{1}{\text{sr}} 10^{-26} \text{ W m}^{-2} \text{ Hz}^{-1} \right] = \frac{2kT}{A_e} \left[\frac{\text{K kg s}^{-2}}{\text{sr}} \right] \quad (5.10)$$

$$S \left[\frac{1}{\text{sr}} 10^{-26} \text{ kg m}^2 \text{ s}^{-3} \text{ m}^{-2} \text{ Hz}^{-1} \right] = \frac{2kT}{A_e} \left[\frac{\text{K kg s}^{-2}}{\text{sr}} \right] \quad (5.11)$$

Thus, $\frac{T}{S} = 15.39 \left[\frac{\mu\text{K}}{\text{Jy}} \right]$ where the effective area of the antenna is

$$A_e = \frac{c^2}{v_{\text{ABS}}^2 \Omega_{\text{ABS}}} = 4.25 \times 10^{-2} \frac{\text{m}^2}{\text{sr}}$$

$$\Omega_{\text{ABS}} = 2\pi \sigma_{\text{ABS}}^2 \sim 100.5 \mu\text{Sr}.$$

where k is the Boltzmann's constant ($1.38 \times 10^{-23} \text{ m}^2 \text{ Kg s}^{-2} \text{ K}^{-1}$), $\sigma_{\text{ABS}} = \frac{32.4}{\sqrt{8\ln 2}}$ arcmins, and 32.4 arcmins⁴ is the FWHM of the ABS beam. The above temperature is called the *Antenna temperature* T_A or *Rayleigh-Jeans temperature* T_{RJ} , and EQ. 5.12⁵ gives the conversion factor C to convert T_{RJ} to the thermodynamic temperature

$$C = \frac{(e^x - 1)^2}{x^2 e^x} \quad (5.12)$$

⁴QUIET experiments beam size is 27.3 arcmins and has been used for the same calculations.

⁵Refer to <https://irssasupport.ipac.caltech.edu/index.php?/Knowledgebase/Article/View/181>.

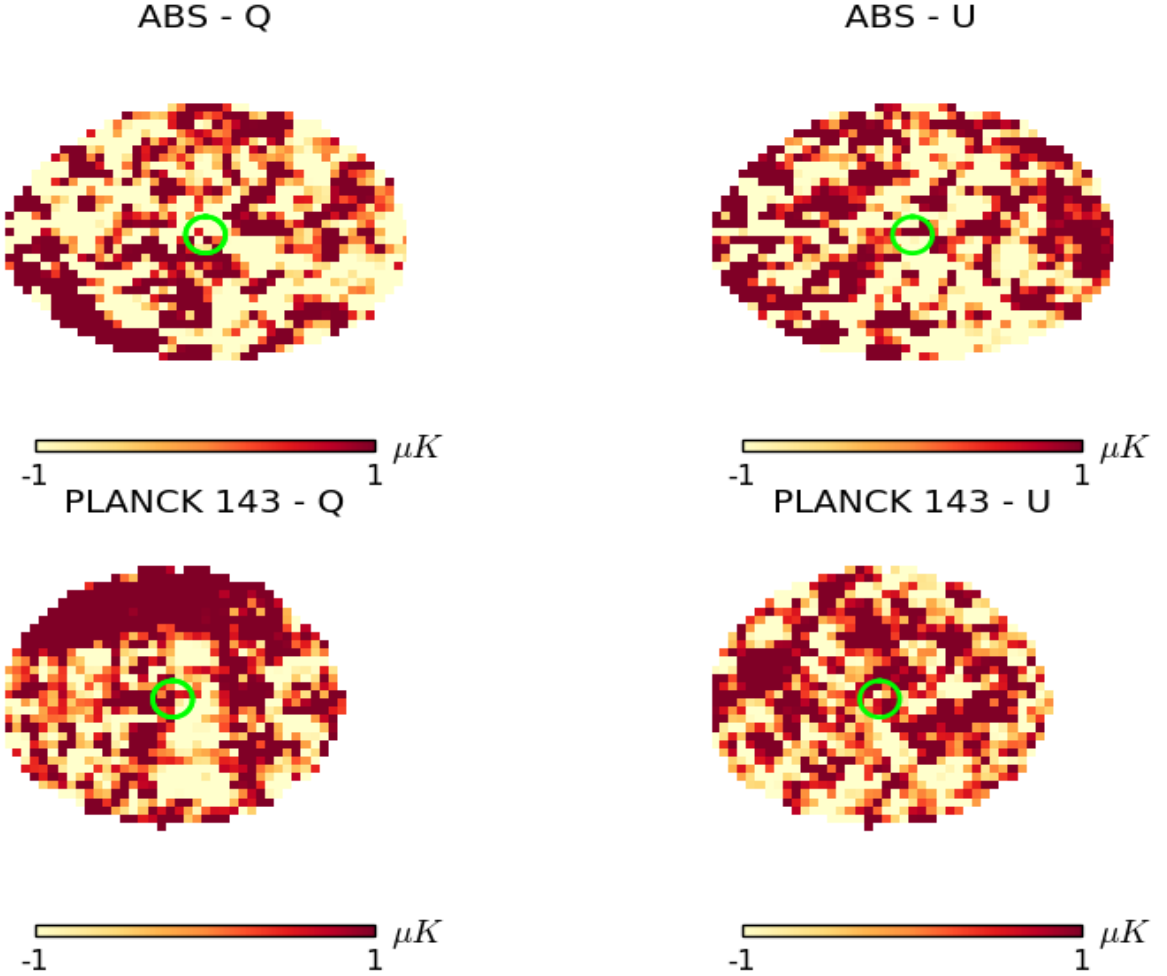


Figura 5.2: The region (50 sq.deg) around PicA galaxy from ABS Q, U maps (in equatorial coordinates) in the top panel. The bottom panel shows the region (in galactic coordinates) from the Planck 143 GHz channel. The presence of PicA in the maps is not obvious. The temperature of PicA should be $\sim 1.2 \mu\text{K}$ (EQ. 5.11,5.12).

where $x = \frac{hv}{kT}$ $v = 2.552$ for ABS yielding $C = 1.67^6$. The temperature of the PicA source for ABS, and QUIET are shown in TAB. 5.2.2.

5.2.3. Apodization algorithm, and the source mask

The apodization algorithm uses a 2d-Hanning kernel given by EQ. 5.13.

$$H(x) = \frac{1}{2} \left[1 - \cos \left(\frac{2\pi x}{N-1} \right) \right] \quad (5.13)$$

The first step in creating a source mask is to create a dummy mask populated with all ones having the same dimensions of the original map. Then value of this dummy mask was set to

⁶For QUIET-W band with $v=91$ GHz, the conversion factor is 1.23. This is used in TAB. 5.2.2.

Quantity	AT20G	QUIET-Q	QUIET-W	ABS
	20 [GHz]	41 [GHz]	94 [GHz]	145 [GHz]
S_Q [mJy]	-	153 ± 26	68.91 ± 31 75.57	47.66
S_U [mJy]	-	-143 ± 26	-66.20 ± 31 -70.63	-45.79
S_P [mJy]	423	205^{+31}_{-21} 229.79	89 ± 33 101.26	61.57

Tabla 5.1: The brightness of PicA galaxy measured at different frequencies by different experiments. The numbers in red correspond to the extrapolated values from the previous frequency on the table (i.e.:) QUIET-Q's extrapolated value is using AT20G, QUIET-W from QUIET-Q, and ABS from QUIET-W. The subscripts Q, U, P correspond to Stokes parameters, and the polarisation intensity $\sqrt{Q^2 + U^2}$. The extrapolation was done using $\beta = 0.85$ and matches very well to the actual observed value. The PicA galaxy is not seen by ABS as its temperature level at 145 GHz $\sim 1\mu\text{K}$ is comparable to the rms of our maps.

Quantity	QUIET-Q	QUIET-W	ABS
	41 [GHz]	94 [GHz]	145 [GHz]
T_Q^A [μK]	40.00	3.42	0.73
T_U^A [μK]	-37.38	-3.29	-0.70
T_Q^{thermo} [μK]	49.32	4.21	1.22
T_U^{thermo} [μK]	-46.08	-4.05	-1.17

Tabla 5.2: The antenna T_A , and thermodynamic T_{thermo} temperatures of PicA for QUIET, and ABS calculated using EQ. 5.11, 5.12. Red colour for ABS indicates that the flux value used for calculation is the extrapolated value using $\beta = 0.85$ from QUIET-W band.

zero at the location of the 66 unique source positions. Since, the point sources may not span just one pixel on the map, the region with in one degree from the sources were set to zero. Now, we have dummy masks with circular disks of radius of 1 degree centered on the source positions. This dummy mask is convolved with the 2d-Hanning kernel to produce the final mask.

The kernel ensures that the flux of the point sources decay to zero smoothly as a cosine function. This final point source mask is convolved with the original ABS map to remove the contaminations due to bright point sources which can affect the final power spectrum estimation. The ABS point source mask convolved with the weight map in equatorial coordinates from the v63 of the null test is shown in FIG. 5.3.

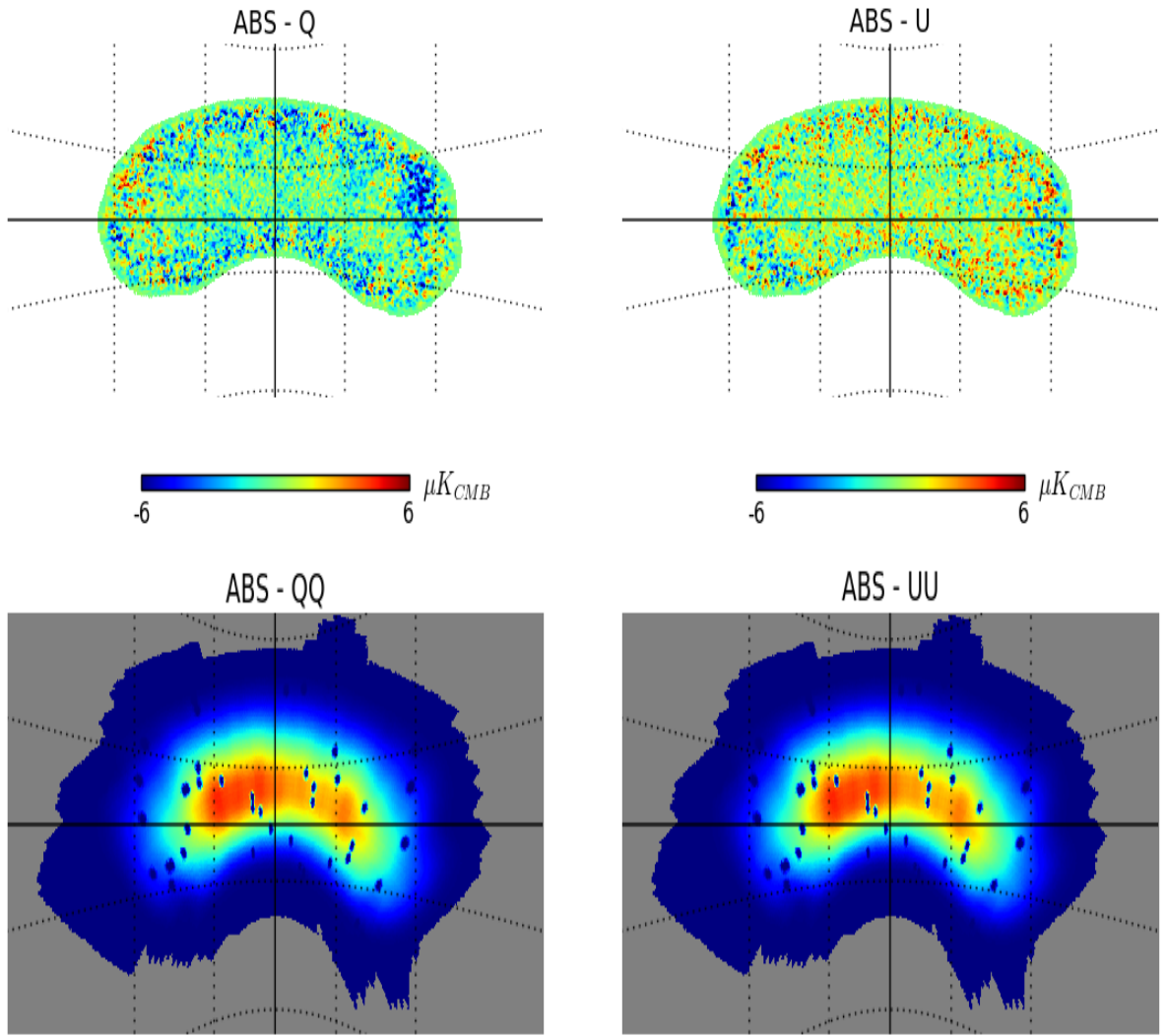


Figura 5.3: The ABS maps of Stokes parameters Q (left), U (right) is shown in the top panel in μK_{CMB} . The corresponding covariance (weights) QQ, UU are in the bottom panel. The maps have been convolved with the point source mask using the sources from Planck, and WMAP catalogues. A flux threshold of 500 mJy has been applied to select the sources. All the maps, originally in equatorial coordinates have been projected to cartesian basis.

Capítulo 6

RESULTS

Overview, and goals:

Here I discuss about the estimation of power spectrum using Pseudo- C_ℓ techniques from the inverse noise variance polarisation maps of the ABS field-A. The final power spectrum is not shown as we are yet to have the final set of data selection methods. The analysis validation through exhaustive suite of null tests is shown and I worked on the quantitative assesment of the null tests using the χ^2 statistics.

6.1. Power spectrum using Pseudo- C_ℓ estimator

The power spectrum C_ℓ estimation is the most important step to extract the cosmological information from the maps and encompasses all of the information about the experiment. The C_ℓ s obtained using the SH equations mentioned in section 1.2, 1.5 are unbiased estimators of the temperature and polarisation power spectrum only if defined on a whole sphere (i.e:) for a complete sky coverage. Hence care must be taken in interpreting the C_ℓ s extracted from the fractional sky maps.

Two methods are commonly followed for the power spectrum estimation from a CMB map which does not have a full sky coverage *viz.* the Maximum Likelihood (ML), and the Pseudo- C_ℓ estimators [64, 65]. The ML method is computationally expensive for the current CMB experiments which have high angular resolution and hence many pixels $\mathcal{O}(10^6)$. The computation time for ML technique scales roughly as $\sim N_{\text{pix}}^3$ because of the need for the inversion of the noise matrix. This is a great downside for the current and future CMB high angular resolution experiments as it involves enormous amount of computation time in analysing the data sets. Moreover, implementing the ML technique to perform systematic checks *via null tests* using a vast null suite and a large set of simulations is highly impossible. Hence we use the other technique, the Pseudo- C_ℓ estimators that are related to the true C_ℓ by the function that accounts for the characteristics of the experiment *viz.* sky coverage, filtering applied to the data sets, beam window function, noise in the data. Accordingly, the pseudo power spectrum for a quantity X (which is either temperature or polarisation) is given

by

$$\widetilde{C}_\ell^{XX} = \frac{1}{2\ell+1} \sum_{m=-\ell}^{\ell} |\tilde{a}_{X,lm}|^2 \quad (6.1)$$

where the coefficients $\tilde{a}_{X,lm}$

$$\tilde{a}_{X,lm} = \int d\Omega X(\hat{n}) W(\hat{n}) Y_{lm}(\hat{n}) \quad (6.2)$$

The weight function $W(\hat{n})$ for a particular pixel takes care of all the partial sky coverage [65].

Earlier we mentioned that the a_{lm} for a given multipole ℓ is completely uncorrelated with another multipole ℓ' . This, however, is only true if the SH decomposition is performed on the whole sphere. The Pseudo- C_ℓ technique performs the SH on a partial sky map and hence a quantity that describes the coupling between two multipole ℓ bins must be accounted for to get the true C_ℓ s from the pseudo \widetilde{C}_ℓ . This is called the *mode-mode* coupling matrix $M_{ll'}$ and can be computed numerically using the EQ. A31 from the Appendix in Hivon et al. [65]. Finally by including the effect of beam window function $B_{l'}^2$, (EQ. 3.25), the transfer function $T_{l'}$ (see section 6.2), and the average noise $N_{l'}$, the relation between pseudo \widetilde{C}_ℓ and true C_ℓ can be written as [65]

$$\widetilde{C}_\ell = \sum_{l'} M_{ll'} T_{l'} B_{l'}^2 \langle C_{l'} \rangle + N_{l'} \quad (6.3)$$

For ABS, we used a slight modification of the Monte Carlo Apodized Spherical Transform Estimator (MASTER) [65] Pseudo- C_ℓ estimator written by Kendrick Smith [66, 67] originally for the QUIET experiment. The ABS own version of the Pseudo- C_ℓ estimator is written by Steve Choi. With all the above machinery set, we estimated the power spectrum (EQ. 1.34, 1.36) from the maps of the Stokes parameters Q and U using the inverse noise variance mapper presented in section 5.1 after applying the point source masks (section 5.2). Our multipole ℓ bins range from $45 \leq \ell \leq 400$ with a bin-width $\Delta\ell \sim 30$.

We estimate the auto correlations C_ℓ^{EE} , C_ℓ^{BB} , and the cross correlation between temperature and the scalar E-modes C_ℓ^{TE} . To get the cross correlation, EQ. 6.4 must be modified as

$$\widetilde{C}_\ell^{TE} = \frac{1}{2\ell+1} \sum_{m=-\ell}^{\ell} |\tilde{a}_{T,lm} \tilde{a}_{E,lm}^*| \quad (6.4)$$

Using the C_ℓ^{EE} , C_ℓ^{BB} power spectra we validated our results by performing null tests with an exhaustive ABS null site explained in next section 6.2. Persuaded by the statistics presented by QUIET experiment [41] we estimated both the auto-correlation and cross correlation spectra between two maps. The null tests were performed only with the cross spectra with a valid assumption that the noise is uncorrelated between the two maps (different data sets for null tests).

6.2. Validation of the power spectrum

6.2.1. Null test fundamentals

The null tests play vital role in capturing the systematic errors that were either missed or introduced as artefacts during any of the processing stages. In a null test, the raw data is split into two subsets (that differ in the level of contamination due to a particular source of systematic error), passed through the entire pipeline process, and the CMB maps are made from both the subsets. The type of data splitting is key and the different data splits in the ABS null suite are shown in Table 6.2.1. The maps made out of the two subsets are then differenced. If the data is free from systematics, then the differenced map should be a “null map” and the resulting power spectrum $C_{\ell_{\text{null}}}^{\text{data}}$ must be consistent with white noise power spectrum. The calculation of $C_{\ell_{\text{null}}}$ is shown in EQ. 6.5. A deviation from the white noise power spectrum indicates the presence of a systematic error from the contaminant that was expected to be captured using the respective type of data split.

Tabla 6.1: The systematic biases probed by the 21 null tests in the ABS null test suite.

	Instrument performance	Observing conditions	Data quality	Pointing	Temporal
ambient_temperature		X			X
batchA_vs_batchB_tes	X				
center_vs_peripheral	X			X	
det_angle_split	X				
east_vs_west				X	
fp_left_vs_right	X				
fknee_large_vs_small			X		
humidity_high_vs_low		X			
HWP_fom	X				
moon_above_below_horizon				X	
moon_near_vs_far					X
n_glitches			X		
pwv_high_vs_low		X			
season_halves		X			X
squid_polarity	X				
sss_large_vs_small			X		
stationarity			X		
sun_near_vs_far					X
sun_above_below_horizon				X	X
wind_high_vs_low		X			
wn_large_vs_small	X		X		

Note that the pipeline could act differently on both the subsets based on the filter transfer function (see below), and there will be a difference between the $C_{\ell_{\text{null}}}^{\text{data}}$ from the ideal “null” power spectrum. This is expected. For this reason, the $C_{\ell_{\text{null}}}^{\text{data},s}$ for a particular null

test s is compared against the power spectrum of the differenced map made out of simulations ($C_{\ell_{\text{null}}}^{\text{sims},s}$) for the null test. We performed 80 fiducial Monte-Carlo (MC) simulations to estimate the systematics.

The null power $C_{\ell_{\text{null}}}$ was calculated for all the null tests from the differenced maps (for both data and the simulations) using EQ. 6.5.

$$C_{\ell_{\text{null}}} = \frac{C_{\ell}(d1)}{T_{\ell}^{11}} + \frac{C_{\ell}(d2)}{T_{\ell}^{22}} - 2 \frac{C_{\ell}(d1, d2)}{T_{\ell}^{12}} \quad (6.5)$$

and

$$\begin{aligned} C_{\ell} &= \langle |\alpha_{\ell m}|^2 \rangle \\ C_{\ell}(d1) &= \langle |\alpha_{\ell m}(d1)|^2 \rangle; \quad C_{\ell}(d2) = \langle |\alpha_{\ell m}(d2)|^2 \rangle \\ C_{\ell}(d1, d2) &= \langle \text{Re}|\alpha_{\ell m}(d1) \alpha_{\ell m}^*(d2)|^2 \rangle \\ C_{\ell_{\text{null}}} &= \langle |\alpha_{\ell m}(d1) - \alpha_{\ell m}(d2)|^2 \rangle \\ &= \langle |\alpha_{\ell m}(d1)|^2 \rangle + \langle |\alpha_{\ell m}(d2)|^2 \rangle - 2 \langle \text{Re}|\alpha_{\ell m}(d1) \alpha_{\ell m}^*(d2)|^2 \rangle \end{aligned}$$

where $d1, d2$ represent the two data subsets, and T represents the filter transfer function. To get the filter transfer function, we generate fiducial cosmological signal-only CMB simulations. The simulated CMB maps are converted into TODs using the pointing information of each detector to generate signal-only TODs. The analysis pipeline works on this simulated TOD, and the output power spectrum $C_{\ell}^{\text{out,sims}}$ is computed. The ratio of $C_{\ell}^{\text{out,sims}}$ to the input power spectrum used to simulate the signal-only CMB simulations will give the filter transfer function T . Note that T could be different for the two subsets of data. This is the reason we compare $C_{\ell_{\text{null}}}^{\text{data}}$ to $C_{\ell_{\text{null}}}^{\text{sims}}$ instead of the “real null (zero) power spectrum”. For every null test we obtain the EE, and BB power spectra in 13 ℓ bins in the multipole range $45 \leq \ell < 400$. FIG. 6.1 shows an example BB, and EE $C_{\ell_{\text{null}}}$ spectra for four null tests from the ABS null suite.

The quantitative assessment of the null tests was performed using the χ^2 , χ statistics. For the EE and BB power spectra, we calculated the $\chi_{\text{null}_i} = \left(\frac{C_{\ell_{\text{null}_i}}}{\sigma_i} \right)$, and $\chi_{\text{null}_i}^2$ individually in each bin i for all the 13 power spectral bins. The bin width $\Delta\ell \sim 30$ was chosen heuristically to reduce the coupling (correlation that arises primarily due to the incomplete sky coverage) between adjacent ℓ bins. The weighting factor σ_i is the standard deviation of the $C_{\ell_{\text{null}_i}}^{\text{sims}}$ value of the 80 MC simulations in the respective bin. The total degree of freedom (dof) for the χ^2 will be

$$\text{dof} = 21 \text{ tests} \times 13 \ell \text{ bins} \times 2 (\text{EE/BB}) = 546$$

Given a χ^2 value with particular dof, one can calculate the probabilities to exceed (PTE) the observed χ^2 value. The PTE values are normally calculated from the cumulative distribution function of the χ^2 distribution. We slightly modified the standard definition of the PTE to be the percentage of MC simulations that have a χ^2 value greater than the data. The success (or) the failure of a null test was decided using the PTE values. A null test was declared to be a failure if the PTE value falls below 0.025 (poor χ^2 value implying a non null power spectrum)

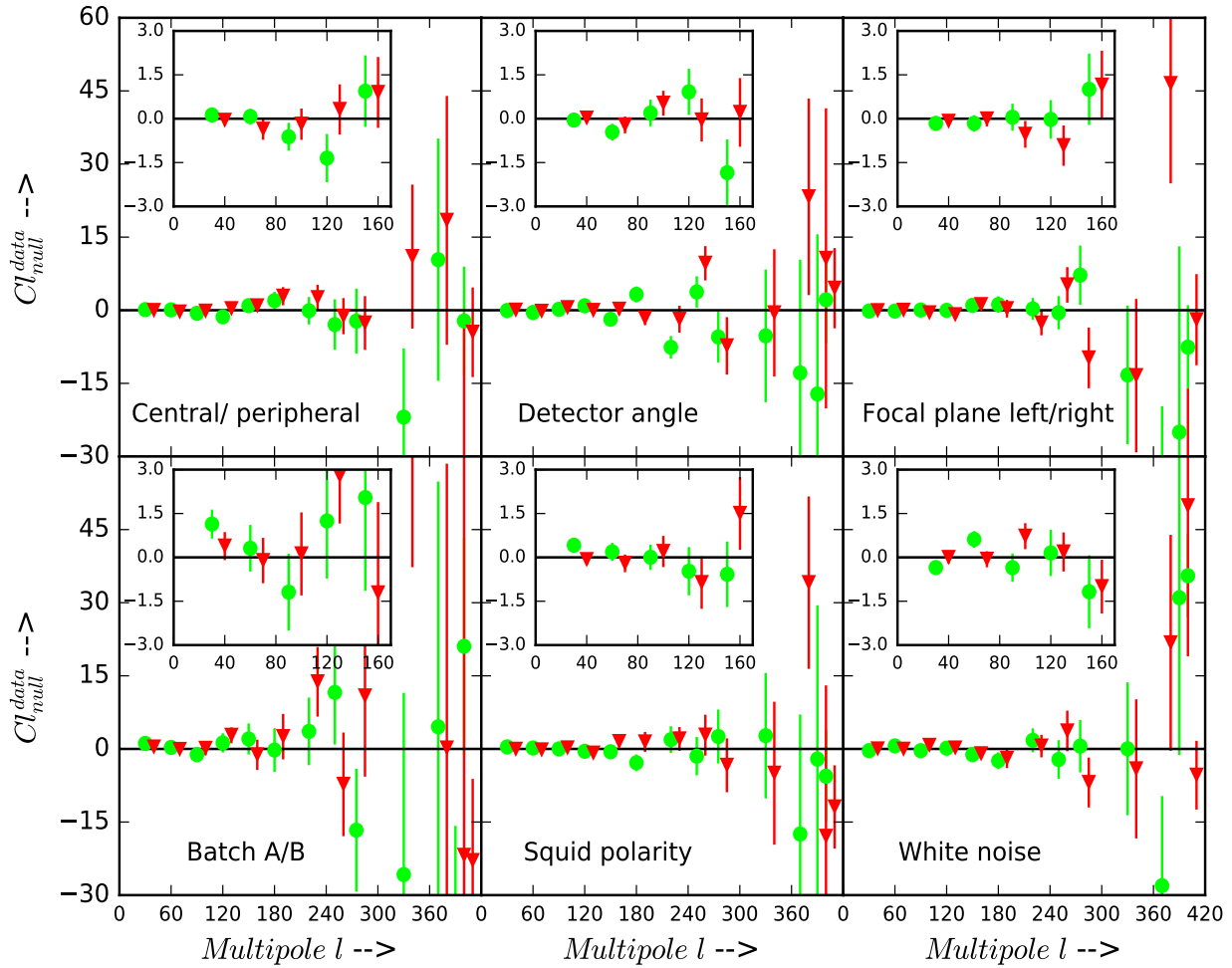


Figura 6.1: The $C_{\ell_{\text{null}}}$ EE (green), and BB (red) spectra for six null tests based on the instrument performance (detector locations on the focal-plane, detector angles, batch A and B, squid polarity, and the white noise level) from the ABS null suite.

or above 0.975 (extremely good χ^2 implying that the errors are poorly estimated). An uniform distribution of the individual PTEs (between 0 and 1) indicates that the differenced maps are consistent with the null result and the absence of systematic errors.

6.2.2. ABS null suite

The ABS null test suite consists of 21 types of null tests designed to probe the systematics due to *viz.* performance of the instrument, observing conditions, pointing, data quality, and temporal variations. Table 6.2.1 lists the ABS null suite along with the major systematic error they are expected to probe. The criteria used to obtain to above the above subsets are shown below. The CESes, and the detectors in each CES below were selected using the data selection techniques mentioned in section 4.1.1.

1. ambient_temperature: To test the systematic mainly due to *observing conditions*. It will

also help to probe the seasonal variations as summer would be hotter than winter.

```
(a) select CONCAT(sched_id,"",sched_subid,"",col,"",row)
from abs_housekeeping natural join abs_timestream where
hk_dewar_outside_t_mean <274 K;
(b)select CONCAT(sched_id,"",sched_subid,"",col,"",row)
from abs_housekeeping natural join abs_timestream where
hk_dewar_outside_t_mean >274 K;
```

2. batchA_vs_batchB_tes: To test the systematic due to *detector performance*. Batch A detectors are from the columns 0, 1, 2, 3, 16, 17, 18, 19, 20, 21, 22, 23, and batch B detectors are from columns 4, 5, 6, 7, 8, 9, 10, 11, 12, 13, 14, 15.

```
(a) select distinct CONCAT(sched_id,"",sched_subid,"",col,"",row) from
abs_timestream where col in batch_A;
(b) select distinct CONCAT(sched_id,"",sched_subid,"",col,"",row) from
abs_timestream where col in batch_B;
```

3. center_vs_peripheral: To test the systematic due to *detector performance, and focal-plane pointing model* using the maps obtained from the detectors close to the centre of the focal-plane, and those away from the centre. In the following queries, focal_plane_x,focal_plane_y correspond to location of the detectors (ν, ω in EQ. 3.14) on the focal-plane.

```
central_teses=select CONCAT(col,"", row) from abs_tes where
focal_plane_x2+focal_plane_y2<16°;
(a) select distinct CONCAT(sched_id,"",sched_subid,"",col,"",row) from
abs_timestream where CONCAT(col,"", row) in central_teses;

edge_teses=select CONCAT(col,"", row) from abs_tes where
focal_plane_x2+focal_plane_y2≥16°;
(b) select distinct CONCAT(sched_id,"",sched_subid,"",col,"",row) from
abs_timestream where CONCAT(col,"", row) in edge_teses;
```

4. det_angle_split: This is also a split based on the TES detectors to test the *polarisation angle calibration, and detector performance*.

```
detangle_neg=select CONCAT(col,"", row) from abs_tes where
polzn_angle<0°;
(a)select distinct CONCAT(sched_id,"",sched_subid,"",col,"",row) from
abs_timestream where CONCAT(col,"", row) in detangle_neg;

detangle_pos=select CONCAT(col,"", row) from abs_tes where
polzn_angle≥0°;
(b)select distinct CONCAT(sched_id,"",sched_subid,"",col,"",row) from
abs_timestream where CONCAT(col,"", row) in detangle_pos;
```

5. east_vs_west: This is a data split based on the azimuth of the observation to test the *pointing*. Note that we observe CMB field-A twice everyday when the patch rises in the east, and sets in the west.

```
(a) select CONCAT(sched_id,"",sched_subid,"",col,"",row) from abs_scan
natural join abs_timestream where azimuth≤180°;
(b)select CONCAT(sched_id,"",sched_subid,"",col,"",row) from abs_scan
natural join abs_timestream where azimuth>180°;
```

6. fp_left_vs_right: This is to test the *detector performance* by performing the null tests based on the observations from the detectors located towards the left, and right of the focal-plane.

```
fp_left_teses=select CONCAT(col,"", row) from abs_tes where
focal_plane_x≤0°;
(a)select distinct CONCAT(sched_id,"",sched_subid,"",col,"",row) from
abs_timestream where CONCAT(col,"", row) in fp_left_teses;

fp_right_teses=select CONCAT(col,"", row) from abs_tes where
focal_plane_x≤0°;
(b)select distinct CONCAT(sched_id,"",sched_subid,"",col,"",row) from
abs_timestream where CONCAT(col,"", row) in fp_right_teses;
```

7. fknee_large_vs_small: To test the systematic due to *data quality, noise model* by splitting the data based on the 1/f noise using the f_{knee} of the demodulated Q,U power spectrum. This can also test the *observing conditions* as bad weather can increase the f_{knee} .

```
(a) select distinct CONCAT(sched_id,"",sched_subid,"",col,"",row)
from abs_timestream where demod1_knee_frequency<0.0011 mHz and
demod2_knee_frequency<0.0011 mHz;
(b) select distinct CONCAT(sched_id,"",sched_subid,"",col,"",row)
from abs_timestream where demod1_knee_frequency≥0.0011 mHz and
demod2_knee_frequency≥0.0011 mHz;
```

8. humidity_high_vs_low: This test is to estimate the systematics due to *observing conditions* based on the humidity value obtained from the APEX radiometer data.

```
(a) select CONCAT(sched_id,"",sched_subid,"",col,"",row)
from abs_housekeeping natural join abs_timestream where
apex_humidity_mean<20 %;
(b) select CONCAT(sched_id,"",sched_subid,"",col,"",row)
from abs_housekeeping natural join abs_timestream where
apex_humidity_mean≥20 %;
```

9. HWP_fom: This is to check the performance of the HWP rotation based on the figure of

merit (fom) defined as the power in the side bands around the HWP 1f peak to the power in the HWP 1f peak. A sharper peak (low fom) represents a good HWP rotation behaviour.

```
(a) select CONCAT(sched_id,"",sched_subid","",col","",row) from
abs_scan natural join abs_hwp_perf where hwprot_fom≥0.00130406; (b)
select CONCAT(sched_id,"",sched_subid","",col","",row) from abs_scan
natural join abs_hwp_perf where hwprot_fom>0.00130406;
```

10. moon_above_below_horizon: This is to test the systematics in the *pointing* model. The pointing characterisation was performed using many Moon, and other point source observations. We did not see any significant effect because of the saturation of Moon, and also the lunar phases. This data split can check such assumptions.

```
(a) select CONCAT(sched_id,"",sched_subid","",col","",row) from
abs_scan natural join abs_timestream where moon_el<0°;
(b) select CONCAT(sched_id,"",sched_subid","",col","",row) from abs_scan
natural join abs_timestream where moon_el≥0°;
```

11. moon_near_vs_far: This test is also to test the *pointing* by splitting the data based on the distance to the Moon.

```
(a) select CONCAT(sched_id,"",sched_subid","",col","",row) from
abs_scan natural join abs_timestream where moon_theta<95°;
(b) select CONCAT(sched_id,"",sched_subid","",col","",row) from abs_scan
natural join abs_timestream where moon_theta≥95°;
```

12. n_glitches: This is to check the *data quality* based on the glitch statistics *viz.* number of two (detector readout issues), and ten sample (cosmic ray type) glitches. We only use the two sample glitches for the data splits to avoid redundancy (correlation between two and ten sample null tests).

```
(a) select CONCAT(sched_id,"",sched_subid","",col","",row) from
abs_timestream where n_2sample_glitch_5sigma<10;
(b) select CONCAT(sched_id,"",sched_subid","",col","",row) from
abs_timestream where n_2sample_glitch_5sigma≥10;
```

13. pwv_high_vs_low: This is for the *observing conditions* based on the PWV data from APEX radiometer. This can also be useful to test the *data quality* as high PWV will increase the $f_{k\text{nee}}$, and *temporal effects* as poor weather is normally expected during winter.

```
(a) select CONCAT(sched_id,"",sched_subid","",col","",row) from
abs_housekeeping natural join abs_timestream where apex_pwv_mean<0.7
mm;
(b) select CONCAT(sched_id,"",sched_subid","",col","",row) from
```

```
abs_housekeeping natural join abs_timestream where apex_pvv_mean≥0.7
mm;
```

14. season_halves: This is to check *temporal variations* in detector performance, and instrument pointing. This can also test the *observing conditions* as the ambient temperature will increase during summer.

```
(a) select CONCAT(sched_id,"",sched_subid,"",col,"",row) from
abs_scan natural join abs_timestream where day_number<298 ;
(b) select CONCAT(sched_id,"",sched_subid,"",col,"",row) from abs_scan
natural join abs_timestream where day_number≥298 ;
```

15. squid_polarity: This probes the effects based on the *instrument performance* by splitting the data from detectors with positive, and negative SQUID polarity.

```
squid_pos=select distinct col from abs_tes where polarity=1;
select distinct CONCAT(sched_id,"",sched_subid,"",col,"",row) from
abs_timestream where col in squid_pos;

squid_neg=select distinct col from abs_tes where polarity=-1;
select distinct CONCAT(sched_id,"",sched_subid,"",col,"",row) from
abs_timestream where col in squid_neg;
```

16. sss_large_vs_small: This data split is to check the *data quality* based on the χ^2 value obtained by fitting Legendre polynomial fitting to the scan synchronous structure in the demodulated timestreams.

```
(a) select distinct CONCAT(sched_id,"",sched_subid,"",col,"",row)
from abs_timestream where demod_scan_synchronous_chi2_real +
demod_scan_synchronous_chi2_imag<2.5 ;
(b) select distinct CONCAT(sched_id,"",sched_subid,"",col,"",row)
from abs_timestream where demod_scan_synchronous_chi2_real +
demod_scan_synchronous_chi2_imag≥2.5 ;
```

17. stationarity: This test will help to check the *data quality* using the deviations of the data from a random Gaussian distribution. The data split are based on the stationarity values of the detector timestreams.

```
(a) select CONCAT(sched_id,"",sched_subid,"",col,"",row) from
abs_timestream where raw_stationarity<0.035;
(b) select CONCAT(sched_id,"",sched_subid,"",col,"",row) from
abs_timestream where raw_stationarity≥0.035;
```

18. sun_near_vs_far: This is primarily to estimate systematics due to *observing conditions*

as the ambient temperature increases. It can also check the *temporal* variations in the data.

```
(a) select CONCAT(sched_id,"",sched_subid,"",col,"",row) from  
abs_scan natural join abs_timestream where sun_theta<95°;  
(b) select CONCAT(sched_id,"",sched_subid,"",col,"",row) from abs_scan  
natural join abs_timestream where sun_theta≥95°;
```

19. sun_above_below_horizon: This is primarily to estimate systematics due to *observing conditions* as the observations in the morning were performed with a higher ambient temperature. A very close proximity to Sun can also affect the HWP performance but all our field-A scans were performed far way from the Sun.

```
(a) select CONCAT(sched_id,"",sched_subid,"",col,"",row) from  
abs_scan natural join abs_timestream where sun_el<0°;  
(b) select CONCAT(sched_id,"",sched_subid,"",col,"",row) from abs_scan  
natural join abs_timestream where sun_el≥0°;
```

20. wind_high_vs_low: The data split based on wind speed is also to check the data contamination due to *observing conditions*.

```
(a) select CONCAT(sched_id,"",sched_subid,"",col,"",row) from  
abs_housekeeping natural join abs_timestream where apex_wind_speed_mean<5  
km/hr;  
(b) select CONCAT(sched_id,"",sched_subid,"",col,"",row)  
from abs_housekeeping natural join abs_timestream where  
apex_wind_speed_mean≥5 km/hr;
```

21. wn_large_vs_small: The data split based on the white noise level of detectors will probe the *detector performance*, and *data quality*.

```
(a) select distinct CONCAT(sched_id,"",sched_subid,"",col,"",row)  
from abs_timestream where demod1_white_noise_ampl<29 aW√sec and  
demod1_white_noise_ampl<29 aW√sec;  
(b) select distinct CONCAT(sched_id,"",sched_subid,"",col,"",row)  
from abs_timestream where demod1_white_noise_ampl≥29 aW√sec and  
demod1_white_noise_ampl≥29 aW√sec;
```

6.2.3. Correlations between data points

Since the χ^2 statistics are only valid if the observations are independent of each other it is important that the data points are not correlated. There could be two sources for the correlation between data points *viz.*

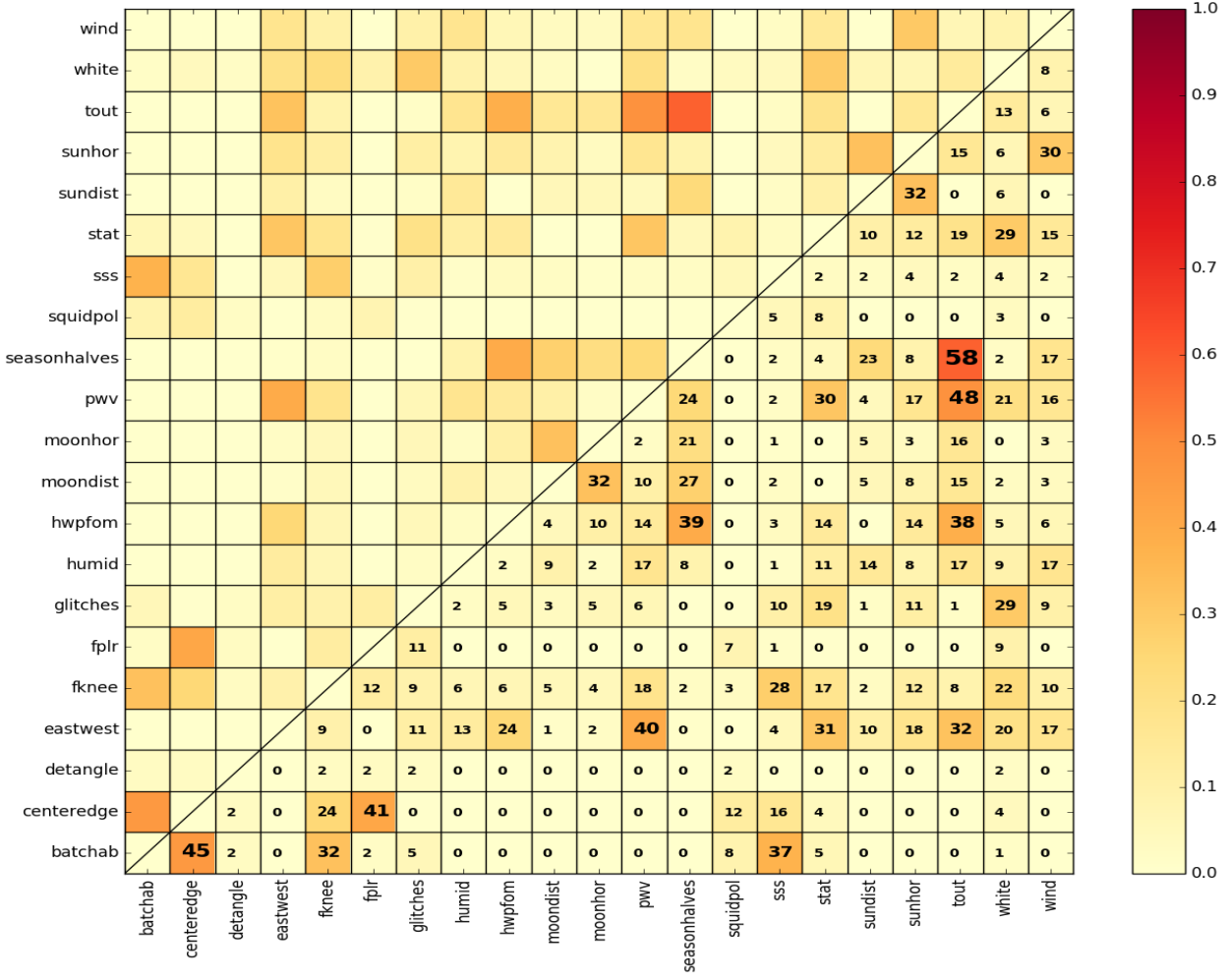


Figura 6.2: The absolute value of the correlation coefficient calculated using (Eq. 6.6) between different null tests in the ABS null suite. Only the off diagonal elements are shown for clarity. The correlation values are explicitly mentioned in the lower triangle of the matrix.

- Correlation between different null tests: This arises based on the conditions used for data splitting.
- Correlation between adjacent power spectral ℓ bins: This arises because of the artefacts in the spherical harmonic transformation of the partial sky coverage [65] of ground-based experiments. The multipole ℓ bins were carefully chosen so that this “mode-mode” coupling can be effectively removed during the power spectrum estimation step (see section 6.1).

Correlation between different null tests

This arises because of the similarity in the conditions used to split the data between different tests. The correlation $C(A, B)$ between two null tests A, and B can be calculated as

shown in EQ. 6.7 [77].

$$C(A, B) = \sqrt{N(A_1)N(A_2)N(B_1)N(B_2)} \\ \times (T1 - T2 - T3 + T4) \quad (6.6)$$

where A_1, B_2, A_2, B_2 are the first and the second data subsets of the two null tests, and

$$T1 = \frac{N(A_1 \cap B_1)}{N(A_1)N(B_1)}; \quad T2 = \frac{N(A_1 \cap B_2)}{N(A_1)N(B_2)} \\ T3 = \frac{N(A_2 \cap B_1)}{N(A_2)N(B_1)}; \quad T4 = \frac{N(A_2 \cap B_2)}{N(A_2)N(B_2)}$$

The initial ABS null test suite consisted of 26 null tests. Five of them were removed because of the strong correlation with other null tests. After careful iteration the suite was reduced to 21 null tests to reduce statistical redundancies. FIG. 6.2 shows the correlation values between the 21 null tests in the final ABS null suite calculated using EQ. 6.6. The existence of the small correlations is the reason why the final χ^2_{null} distribution would not resemble a real χ^2_{null} distribution.

6.2.4. Null test results

Table 6.2.4 summarises the χ^2 , and the PTE values evaluated over all the 13 power spectral bins for the version 63 of the ABS null suite performed over the data from the CMB field-A observations obtained during the first two seasons. The left (right) plots in the bottom panel of FIG. 6.3 shows the distribution of the χ^2 values for EE (BB) null power spectra. The top panel is just a combination of the bottom panels. The three orange shades represent the (1σ , 2σ , and 3σ) errors obtained from the 80 MC simulations discussed earlier. The inset plot in the panels shows the “uniform” distribution of the PTE values indicating that the null tests are normal. The overall PTE value of 0.26 (0.38) for EE (BB) is also completely normal. The combined global PTE value of 0.26 is also good. The results of the individual null tests are shown for reference in the TAB. 6.2.4. Except two EE tests marked in red (ambient outside temperature, and the distance to Sun), all the other null tests were successful. Two failed tests in a total of 40¹ is allowable and we do not investigate them further.

Null power at the first power spectral bin

Despite the success of the null tests when including information from all the 13 power spectral bins, we separately investigated the null test performance in the first bin in the multipole range $45 \leq \ell < 70$ as the tensor-scalar ratio r is highly sensitive to large-scale noise present in the first bin. Two EE null tests *viz.* the split based on season halves, and squid polarity have χ^2 of 6.66, and 8.01 respectively at the first bin. For BB, the null test

¹Note that there are only 20 tests as the test based on the HWP rotation will be added in the next version of the null test run.

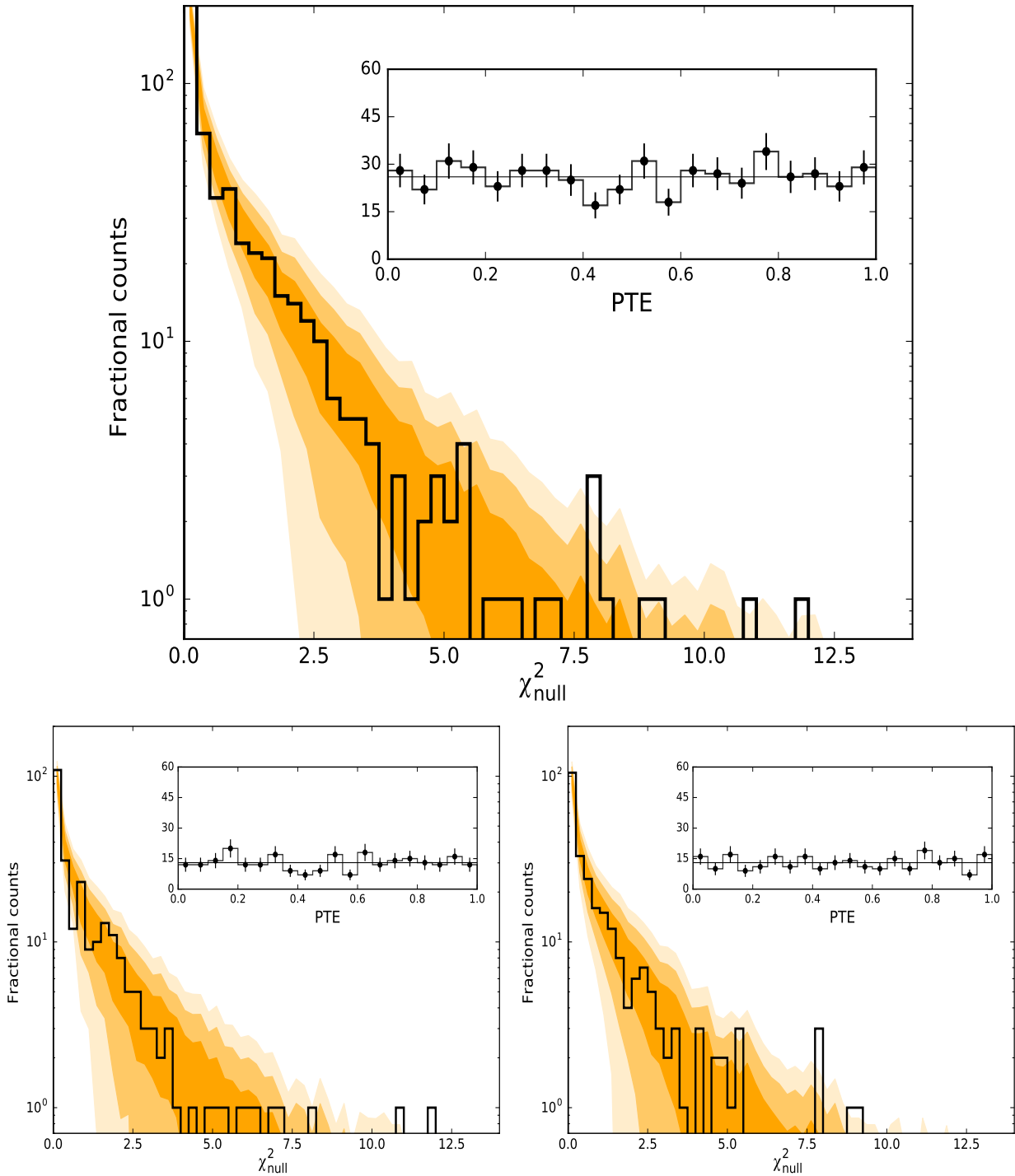


Figura 6.3: The distribution of $\chi^2_{\text{null,data}}$ values of the 13 power spectral bins from the ABS null suite are shown as the black histogram. The top panel shows the combined χ^2 values for EE, and BB power spectra. The bottom left (right) panel show the EE (BB) χ^2 values separately. The counts lie well between the $(1\sigma, 2\sigma, \text{ and } 3\sigma)$ errors obtained from MC simulations which are shown as different shades of orange around the black histogram. The inset plot shows the “uniform” distribution of the PTE values declaring the success of the null tests. The overall χ^2 , and PTE values are also listed for each panel and look normal.

Tabla 6.2: ABS null test results for the version v63 run. The χ^2 , and the PTE values are shown for each null test using information from all the 13 ℓ bins. The two bad results for the test based on the ambient outside temperature, and sun distance are marked in red. All other tests look normal along with the overall PTE values listed at the bottom of the table. The global PTE value of 0.263 is shown in the top panel of FIG. 6.3.

Null suite type	EE (dof=13)			BB (dof=13)		
	χ^2	PTE	Success	χ^2	PTE	Success
ambient_t_high_vs_low	26.544	0.013	0	11.894	0.588	1
center_vs_peripheral	9.073	0.825	1	12.826	0.475	1
det_angle_split	18.450	0.138	1	14.054	0.388	1
east_vs_west	21.453	0.062	1	8.587	0.812	1
fknee_large_vs_small	16.164	0.163	1	14.802	0.312	1
fp_left_vs_right	9.292	0.775	1	21.848	0.062	1
good_vs_bad_tes	12.057	0.550	1	13.777	0.375	1
humidity_high_vs_low	10.096	0.650	1	13.912	0.425	1
moon_above_below_horizon	9.968	0.637	1	7.991	0.825	1
moon_near_vs_far	6.730	0.900	1	22.658	0.075	1
n_glitches	12.155	0.550	1	19.435	0.075	1
pwv_high_vs_low	12.735	0.500	1	9.136	0.800	1
season_halves	14.671	0.412	1	10.056	0.750	1
squid_polarity	16.452	0.237	1	13.323	0.425	1
sss_large_vs_small	16.448	0.237	1	13.858	0.425	1
stationarity	19.504	0.075	1	13.047	0.512	1
sun_above_below_horizon	11.137	0.613	1	15.362	0.338	1
sun_near_vs_far	5.661	0.975	0	12.191	0.525	1
wind_high_vs_low	5.334	0.950	1	10.774	0.725	1
wn_large_vs_small	23.994	0.037	1	10.995	0.675	1
Total	277.917	0.263	1	270.524	0.388	1
Global	$\chi^2 = 548.442$; PTE = 0.263; dof = 520; Success = 1					

based on $f_{k_{\text{nee}}}$ has a $\chi^2 = 5.04$, and the test based on the distance to Moon has extremely low $\chi^2 = 0.001$. The black histogram in FIG. 6.4 shows the worst χ^2 value of each of the 80 simulations for the first power spectral bin for EE (panel) and BB (right). The green (red) vertical line represents the χ^2 of the data in the same bin for the passed (failed) null tests. The χ^2 distribution for all null tests (same as FIG. 6.3) for the first bin is shown in FIG. 6.5.

Despite the above four tests, we obtain a global $\chi^2_{\text{null,data}} = 51.23$ in the first bin ($\text{dof} = 40$). The percentage of MC simulation with $\chi^2_{\text{null,sims}} \geq 51.23$ is 15 per cent (PTE value of 0.15). The PTE values for EE and BB separately are 0.10, 0.46 respectively (also shown in FIG. 6.5). These results suggest that our null tests are successful.

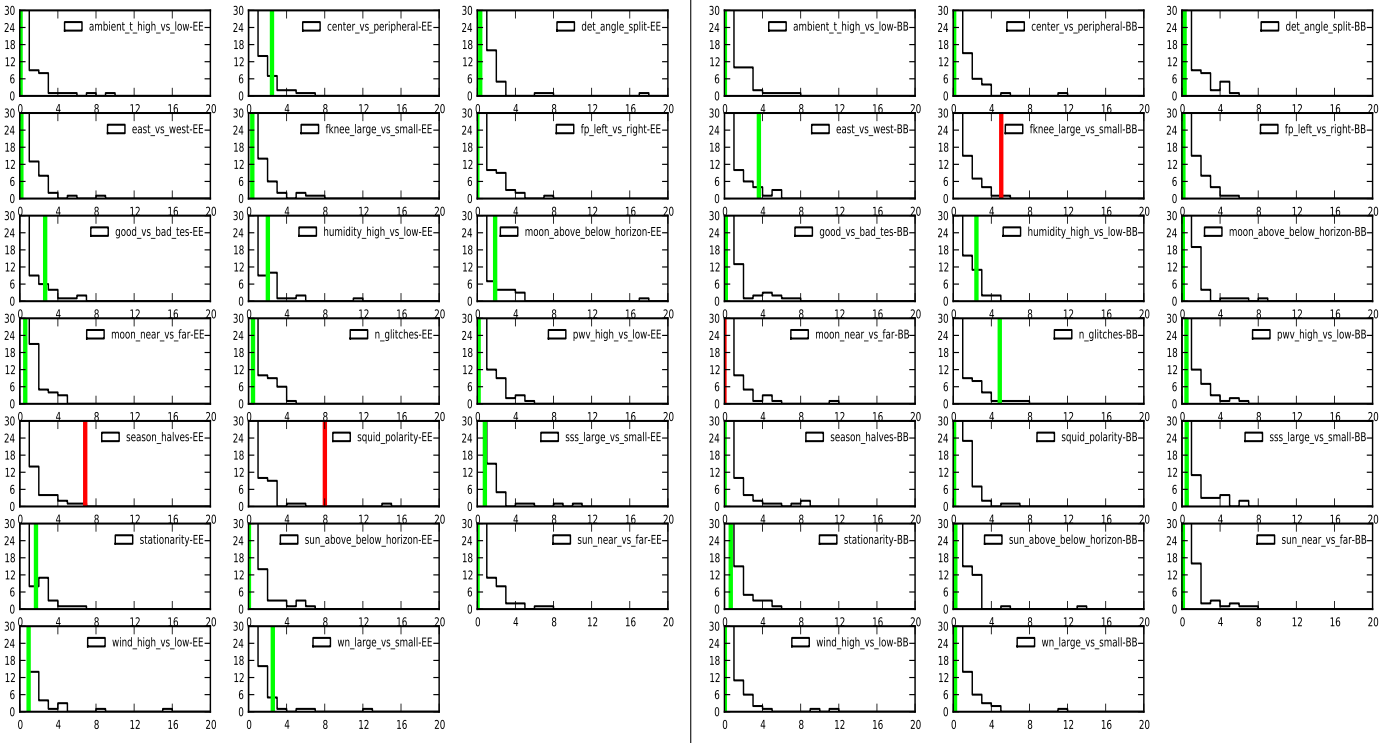


Figura 6.4: Worst χ^2 values in each of the 80 simulations for all null tests in the first power spectral bin is shown as the black histogram. The green (red) vertical represents the χ^2 of the data in the same bin for the passed (failed) null tests.

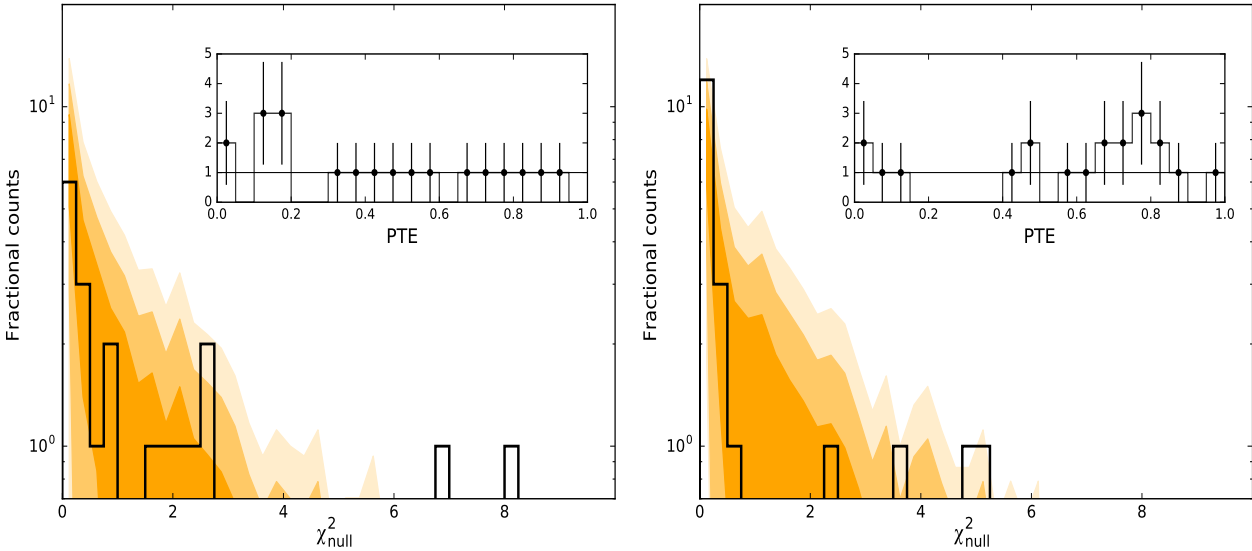


Figura 6.5: Same as FIG. 6.3 but only for the first power spectral bin. Left panel is for EE, and right panel is for BB spectra.

Distribution of χ_{null}

Finally motivated by QUIET experiment [41] we checked the distribution χ_{null} of the null tests. The $\chi_{\text{null}}^{\text{data}}$ distribution is extremely efficient in detecting bias in the experiment.

The QUIET experiment discovered a positive bias as high as 21 per cent in χ_{null} when the (cross) correlations between different datasets were ignored. The use of cross correlation will remove spurious signals (but not the CMB which will be highly correlated) that are not correlated between the two datasets. The reason for the positive bias was suspected to be due to different ground pickup signals in the datasets divided based on telescope pointing. FIG. 6.6 shows the distribution of the $\chi_{\text{null}}^{\text{data}}$ after including the cross correlations between different datasets for ABS. The black histogram is the 80 simulations, and the red data points are from the EE, BB null spectra from ABS null suite. The error bars in each bin is the one sigma (standard deviation) of the data points in the respective bin. There is no bias (skewness) observed and the data points follow the simulations with zero mean within error bars $\overline{\chi_{\text{null}}^{\text{data}}}$ is 0.036 ± 0.045 .

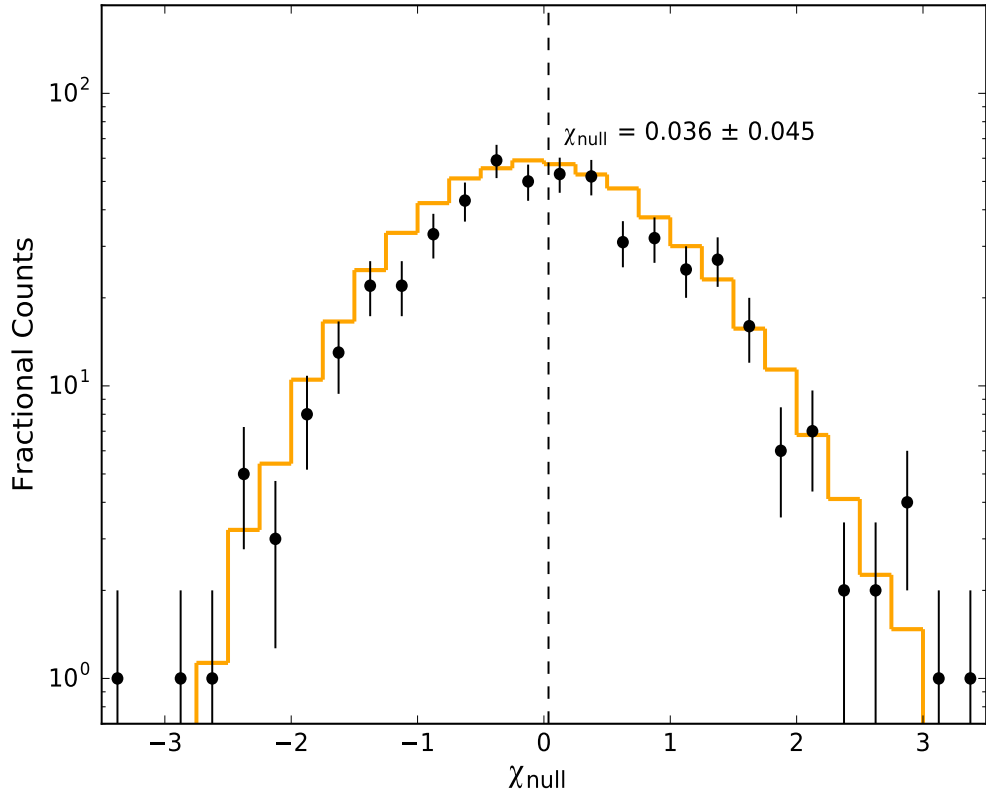


Figura 6.6: Distribution of the χ_{null} of the data (red) and the MC simulations (black histogram) of the ABS null suite. We have used the cross correlation between different datasets while calculating the null spectra. The error bars correspond to the standard deviation of the data points in the respective bin. The data nicely follows the simulations and does not show any bias (with a zero mean) in our results. The mean $\chi_{\text{null}}^{\text{data}}$ value is mentioned in the figure.

6.3. Current status of ABS

The ABS HWP has performed exceptionally well in reducing the contamination from the unpolarised atmosphere. This is one of the major results of the ABS and it has inspired other

major CMB experiments like ACTPol, and POLARBEAR to consider the rapid polarisation modulation using the HWP.

On the other hand, the final result of the ABS experiment, *the C_l^{BB} power spectrum*, is not shown here as we are currently in the process of finalising the data selection techniques, and the calibration models. The ABS null suite will be run again with a larger set of MC simulations (~ 400 as opposed to 80 MC simulations currently) and this final configuration. The current results of the null tests reveal no significant systematics affecting our power spectrum estimation. The other most important piece of information is the characterisation of the foreground from the Milky-Way. Steve Choi is currently performing this task by using the data from all the WMAP frequency channels for *synchrotron* [30], and the Planck HFI 353 GHz channel for the *dust* [44] modelling respectively. The final results of ABS is expected to be released before March 2016.

Bibliografía

- [1] Ryden, B., S., “Introduction to cosmology”, Addison Wesley (2003).
- [2] Dodelson, S., “Modern cosmology”, Amsterdam, Netherlands: Academic Press (2003).
- [3] Penzias, A., A., & Wilson, R., W., “A Measurement of Excess Antenna Temperature at 4080 Mc/s.”, ApJ, 142, 419 (1965).
- [4] Smoot, G., F. *et al.* [COBE Collaboration], “Structure in the COBE differential microwave radiometer first-year maps”, ApJ, 396, 1 (1992).
- [5] Torbet, E. *et al.* [MAT Collaboration], “A Measurement of the Angular Power Spectrum of the Microwave Background Made from the High Chilean Andes”, ApJ, 521, L79-L82 (1999).
- [6] Miller, A. *et al.* [MAT Collaboration], “The QMAP and MAT/TOCO Experiments for Measuring Anisotropy in the Cosmic Microwave Background”, ApJs, 140, 115-141 (2002).
- [7] de Bernardis, P., et al. [BOOMERanG Collaboration], “First results from the BOOMERanG experiment”, arXiv: astro-ph/0011469 (2000).
- [8] Hanany, P., et al. [MAXIMA Collaboration], “MAXIMA-1: A Measurement of the Cosmic Microwave Background Anisotropy on angular scales of 10 arcminutes to 5 degrees”, arXiv: astro-ph/0005123 (2000).
- [9] Komatsu, E. *et al.* [WMAP Collaboration], “Seven-Year Wilkinson Microwave Anisotropy Probe (WMAP) Observations: Cosmological Interpretation”, ApJs, 192, 18 (2011).
- [10] Planck Collaboration, “Planck 2013 results. XV. CMB power spectra and likelihood”, AAP, 571, A15 (2014).
- [11] Lewis, A., Challinor, A., & Lasenby, A., “Efficient Computation of CMB anisotropies in closed FRW models”, AJ, 538, 473 (2000).
- [12] ABS Collaboration, “ABS science results”, *in preparation*.
- [13] Lyth, D., H. & Riotto, A., “Particle physics models of inflation and the cosmological density perturbation”, Phys. Rept. 314, 1 (1999).

- [14] Baumann, D., “TASI Lectures on Inflation”, arXiv: 0907.5424 (2009).
- [15] Guth, A., H., “Inflationary universe: A possible solution to the horizon and flatness problems”, Physical Review D, 23, 347 (1981).
- [16] Linde, A., D., “A new inflationary universe scenario: A possible solution of the horizon, flatness, homogeneity, isotropy and primordial monopole problems”, Physics Letters B, 108, 389 (1982).
- [17] Albrecht, A., & Steinhardt, P. J., “Cosmology for grand unified theories with radiatively induced symmetry breaking”, PRL, 48, 1220 (1982).
- [18] Martin, J. *et al.*, “The Best Inflationary Models After Planck”, arXiv: 1312.3529 (2013).
- [19] Planck Collaboration, “Planck 2015 results. XIII. Cosmological parameters”, arXiv: 1502.01589 (2015).
- [20] Planck Collaboration, “Planck 2015 results. XVII. Constraints on primordial non-Gaussianity”, arXiv: 1502.01592 (2015).
- [21] Planck Collaboration, “Planck 2015 results. XX. Constraints on inflation”, arXiv: 1502.02114 (2015).
- [22] Hu, W., & White, M., “A CMB Polarization Primer”, arXiv: astro-ph/9706147 (1997).
- [23] Kovac, J. M, et al., “Detection of polarization in the cosmic microwave background using DASI”, arXiv: astro-ph/0209478 (2002).
- [24] Hanson, D., et al. [The SPTPol Collaboration], “Detection of B-mode Polarization in the Cosmic Microwave Background with Data from the South Pole Telescope”, arXiv: 1307.5830 (2013).
- [25] POLARBEAR Collaboration, “A Measurement of the Cosmic Microwave Background B-Mode Polarization Power Spectrum at Sub-Degree Scales with POLARBEAR”, arXiv: 1403.2369 (2014).
- [26] BICEP2 Collaboration, “Detection of B-Mode Polarization at Degree Angular Scales by BICEP2”, PRL, 112, 23 (2014).
- [27] BICEP2/Keck, Planck Collaborations, “A Joint Analysis of BICEP2/Keck Array and Planck Data”, arXiv: 1502.00612 (2015).
- [28] Knox, L., “Determination of Inflationary Observables by Cosmic Microwave Background Anisotropy Experiments”, arXiv: astro-ph/9504054 (1995).
- [29] Tegmark, M., “CMB mapping experiments: a designer’s guide”, arXiv: astro-ph/9705188 (1997).
- [30] Bennett, C. L., et al. [WMAP Collaboration], “Nine-Year Wilkinson Microwave Anisotropy Probe (WMAP) Observations: Final Maps and Results”, arXiv: 1212.5225 (2013).

- [31] Keck Array, BICEP2 Collaborations, "BICEP2 / Keck Array VI: Improved Constraints On Cosmology and Foregrounds When Adding 95 GHz Data From Keck Array", arXiv:1510.09217 (2015).
- [32] Chiang C., et al. [BICEP Collaboration], "Measurement of cosmic microwave background polarization power spectra from two years of BICEP data", arXiv: 0906.1181 (2010)
- [33] Dodelson, S., et al., "The Origin of the Universe as Revealed Through the Polarization of the Cosmic Microwave Background", arXiv: 0902.3796 (2009).
- [34] Simon, S.M., Raghunathan, S. et al. [ABS Collaboration], "Characterization of the Atacama B-mode Search", Society of Photo-Optical Instrumentation Engineers (SPIE) Conference Series, 9153, 0 (2014).
- [35] Appel, J., W., "Detectors for the Atacama B-Mode Search Experiment", Doctoral dissertation, PRINCETON UNIVERSITY (2012).
- [36] Essinger-Hileman, T, "Probing Inflationary Cosmology: The Atacama B-Mode Search (ABS)", Doctoral dissertation, PRINCETON UNIVERSITY (2011).
- [37] Visnjic, C, "Data Characteristics and Preliminary Results from the Atacama B-Mode Search (ABS)", Doctoral dissertation, PRINCETON UNIVERSITY (2013).
- [38] Pardo, J.R., Cernicharo, J.,& Serabyn, E., "Atmospheric transmission at microwaves (atm): an improved model for millimeter/submillimeter applications", IEEE, 49, 1683 (2011).
- [39] Finkbeiner, D. P., Davis, M., & Schlegel, D, J., "Extrapolation of Galactic Dust Emission at 100 Microns to CMBR Frequencies Using FIRAS", arXiv: 9905128 (1999).
- [40] Jones, W. C., et al. [B2K Collaboration], "A Measurement of the Angular Power Spectrum of the CMB Temperature Anisotropy from the 2003 Flight of Boomerang", arXiv: astro-ph/0507494 (2006).
- [41] QUIET Collaboration, "First Season QUIET Observations: Measurements of CMB Polarization Power Spectra at 43 GHz in the Multipole Range $25 \leq \ell \leq 475$ ", ApJ, 741, 111 (2011).
- [42] Rahlin, A. S. et al. [SPIDER Collaboration], "Pre-flight integration and characterization of the SPIDER balloon-borne telescope", Society of Photo-Optical Instrumentation Engineers (SPIE) Conference Series, 9153, 13 (2014).
- [43] Planck Collaboration, "Planck 2015 results. VI. LFI mapmaking", arXiv: 1502.01585 (2015).
- [44] Planck Collaboration, "Planck 2015 results. VIII. High Frequency Instrument data processing: Calibration and maps", arXiv: 1502.01587 (2015).
- [45] Loken et al., 2010, "SciNet: Lessons Learned from Building a Power-efficient Top-20

- System and Data Centre”, Journal of Physics: Conference Series, 256, 1 (2010).
- [46] Parker, L.P., “The Atacama B-Mode Search: Instrumentation and Observations”, Doctoral dissertation, PRINCETON UNIVERSITY (2015).
- [47] MAXIPOL Collaboration, “MAXIPOL: Cosmic Microwave Background Polarimetry Using a Rotating Half-Wave Plate”, arXiv: 0611394 (2006).
- [48] Kusaka, A., Essinger-Hileman, T. et al. [ABS Collaboration], “Modulation of cosmic microwave background polarization with a warm rapidly rotating half-wave plate on the Atacama B-Mode Search instrument”, Review of Scientific Instruments, 85, 3 (2014).
- [49] Essinger-Hileman, T., Kusaka, A., et al. [ABS Collaboration], “Systematics of an ambient-temperature, rapidly-rotating half-wave plate”, *in preparation*.
- [50] Imbriale, W. A., & Hodges, R. E., “The Linear-Phase Triangular Facet Approximation in Physical Optics Analysis of Reflector Antennas”, Applied Computing and Electromagnetics Soc. J., 6, 74 (1991).
- [51] Gorski, K. M. et al., “HEALPix: A Framework for High-Resolution Discretization and Fast Analysis of Data Distributed on the Sphere”, ApJ, 622, 759 (2005).
- [52] Weisstein, E. W., “Euler Angles From MathWorld—A Wolfram Web Resource.”
- [53] Page, L., et al. [WMAP Collaboration], “First-Year Wilkinson Microwave Anisotropy Probe (WMAP) Observations: Beam Profiles and Window Functions”, ApJS., 148, 39 (2003).
- [54] Aumont, J., Conversi, L., Thum, C. et al., “Measurement of the Crab nebula polarization at 90 GHz as a calibrator for CMB experiments”, arXiv: 0912.1751 (2009).
- [55] Weiland, J. L., et al. [WMAP Collaboration], “Seven-year Wilkinson Microwave Anisotropy Probe (WMAP) Observations: Planets and Celestial Calibration Sources”, ApJS., 192, 19 (2011).
- [56] Griffin, M. J., et al., “Submillimeter and millimeter observations of Jupiter”, Icarus, 65, 244 (1986).
- [57] Dunner, R., et al. [ACT Collaboration], “The Atacama Cosmology Telescope: Data Characterization and Map Making”, arXiv: 1208.0050 (2012).
- [58] Dunner, R., “From Data to Maps with the Atacama Cosmology Telescope”, Doctoral dissertation, Pontificia Universidad Católica de Chile (2009).
- [59] QUIET Collaboration, “The QUIET Instrument”, arXiv: 1207.5562 (2012).
- [60] George, E. M. et al. [SPTPol Collaboration], “Performance and on-sky optical characterization of the SPTpol instrument”, arXiv: 1210.4971 (2012).
- [61] WMAP Collaboration, “First Year Wilkinson Microwave Anisotropy Probe (WMAP)

Observations: Galactic Signal Contamination from Sidelobe Pickup”, arXiv: astro-ph/0302215 (2003).

- [62] Chinone, Y., “Measurement of Cosmic Microwave Background Polarization Power Spectra at 43 GHz with Q/U Imaging ExperimenT”, Doctoral dissertation, TOHOKU UNIVERSITY (2010).
- [63] Næss, S., “Maximum likelihood analysis with the Q/U Imaging ExperimenT”, Doctoral dissertation, UNIVERSITY OF OSLO (2012).
- [64] Bond J. R., et al., “Estimating the Power Spectrum of the Cosmic Microwave Background”, arXiv: astro-ph/9708203v3 (1997).
- [65] Hivon, E. et al., “MASTER of the CMB Anisotropy Power Spectrum: A Fast Method for Statistical Analysis of Large and Complex CMB Data Sets”, arXiv: astro-ph/0105302 (2001).
- [66] Smith K. M., “Pure pseudo- C_ℓ estimators for CMB B-modes”, arXiv: astro-ph/0608662v1 (2006).
- [67] Smith K. M., Zaldarriaga M., “A general solution to the E-B mixing problem”, arXiv: astro-ph/0610059 (2006).
- [68] QUIET Collaboration, “The Q/U Imaging ExperimenT: Polarization Measurements of the Galactic Plane at 43 and 95 GHz”, arXiv: 1508.02778 (2015).
- [69] Murphy, T. et al., “The Australia Telescope 20 GHz Survey: The Source Catalogue”, arXiv: 0911.0002 (2009).
- [70] Reichardt, C. L., et al. [ACBAR Collaboration], “High resolution CMB power spectrum from the complete ACBAR data set”, arXiv: 0801.1491 (2008).
- [71] Marriage, T., A., et al. [ACT Collaboration], “Atacama Cosmology Telescope: Extragalactic Sources at 148 GHz in the 2008 Survey”, arXiv: 1007.5256 (2010).
- [72] Ade, P.A.R *et al.* [Planck Collaboration], “Planck 2015 results. XXVI. The Second Planck Catalogue of Compact Sources”, arXiv: 1507.02058 (2015).
- [73] Mocanu, L., M., et al. [SPT Collaboration], “Extragalactic millimeter-wave point source catalog, number counts and statistics from 771 square degrees of the SPT-SZ Survey”, arXiv: 1306.3470 (2013).
- [74] Chen, X., Wright, E.L. et al. [WMAP Collaboration], “Extragalactic Point Source Search in Five-Year WMAP 41, 61, and 94 Ghz Maps”, arXiv: 0809.4025 (2009).
- [75] Perley, R. et al., “The radio galaxy PictorA - A study with the VLA”, A&A, 328, 12 (1997).
- [76] Huffenberger, K., M.. et al. [QUIET Collaboration], “The Q/U Imaging Experiment:

Polarization Measurements of Radio Sources at 43 and 95 GHz”, arXiv: 1412.1111 (2014).

- [77] Bischoff, C., “Observing the Cosmic Microwave Background polarization anisotropy at 40 GHz with QUIET”, Doctoral dissertation, THE UNIVERSITY OF CHICAGO (2010).

Apéndice A

Saran wrap to prevent dust over the HWP

The main components of the ABS telescope are described in section 2.1. Other than those, during the initial stages of observations we decided to use a *saran (plastic) wrap* to wrap the telescope baffle preventing any dust granules that might otherwise accumulate over the HWP. This is primarily to prevent the dust accumulation from degrading the performance of the HWP over time, and secondly the CMB B-modes experiments are highly sensitive to the additional loading introduced by dust granules. We performed several tests to evaluate the behaviour of the data after the introduction of the saran wrap by using the wrap at different locations. The tests were made also to ensure that the wrap itself does not introduce any spurious signal.

No ground screen - Wrap at the top of baffle

The initial set of tests were performed by covering the top of the telescope baffle. The ABS ground screen was not deployed during this time. The results of this is shown in FIG. A. The figure shows the power spectrum of eight randomly picked detectors. The red (green) line shows the power spectrum with (without) the wrap. The labels F1 through F4 represent the different data files used, and are also mentioned on top of each plot. We did not find any significant improvement in the data quality after using the wrap. In fact, the data with the saran wrap looks consistently bad. However, this could also be due to the effect of wind during the observations as we did not have the ground shield. Hence we could not come to a final conclusion about the performance of the saran wrap. The absence of the ground shield could introduce a lot more uncertainties affecting the saran wrap test as well.

With ground screen - Wrap at the top/bottom of baffle

We repeated the test again on 16 April, 2012 after the deployment of the ground screen by wrapping the top of the baffle. On the next day, the wrap was placed between the baffle, and the HWP. The results are shown on FIG. A.2. The green and red lines are with and without the wrap for the data files mentioned on the plot. No significant improvements were seen again but this time the data with the wrap did not look bad. So we concluded that the saran

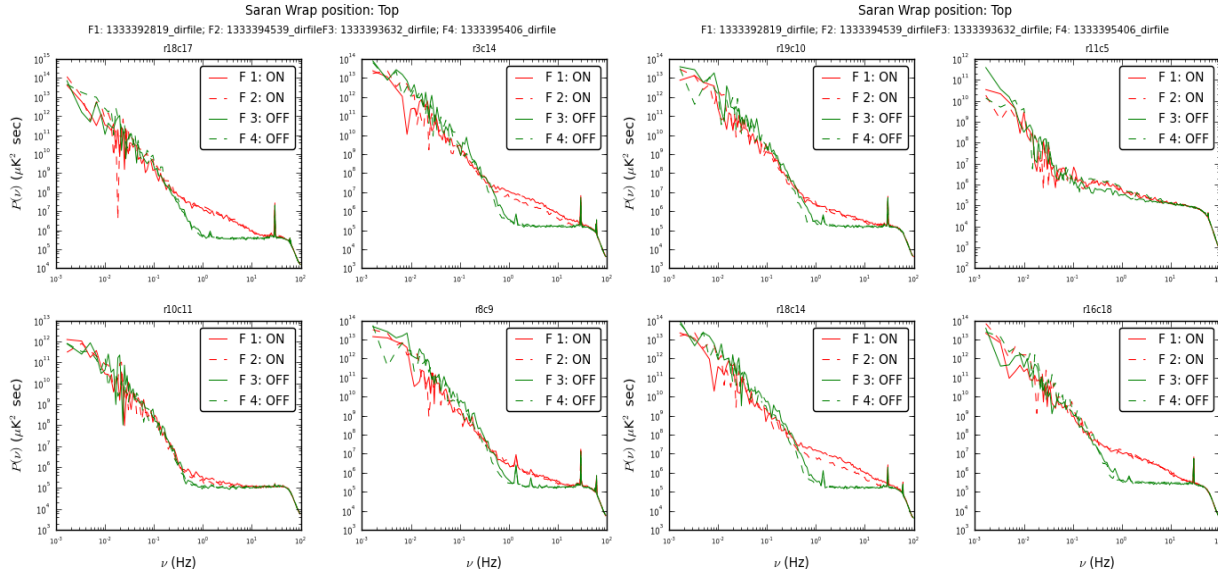


Figura A.1: Power spectrum of the detectors from randomly picked detectors with the wrap on (red) top of the baffle compared to the test without the wrap (green). The test was performed on wrap test performed on April 2, 2012. The data using the wrap seems to be bad. The tests were performed before the introduction of the ground scree. The data files used are mentioned on top of the plot and are labeled as F1 through F4.

wrap did not introduce additional noise in to the data and the earlier bad results were likely due to wind affecting the data quality without the presence of ground screen. Similarly, no significant changes were observed when the wrap was moved from the top to the bottom of the between the baffle. From these results, *we decided to wrap the bottom of the baffle using the saran wrap as it will prevent the dust accumulation over the HWP*. As the wrap would not sustain for long, it changed twice ever week during the He recycling without obstructing the observations.

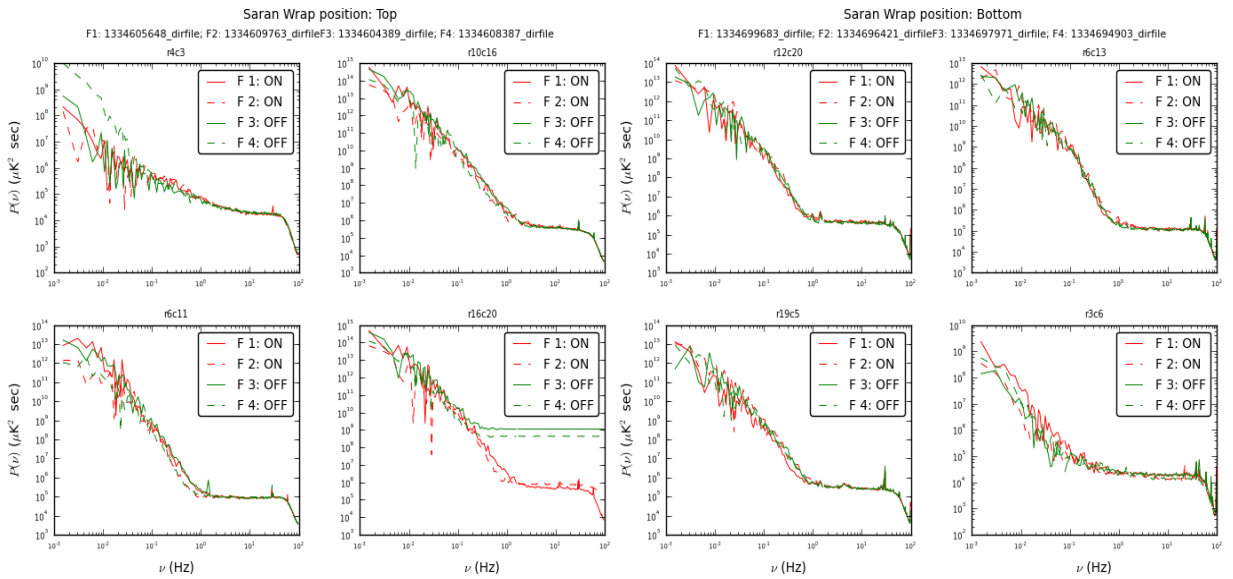


Figura A.2: Saran wrap test performed after the deployment of the ground screen. The left (right) shows the data taken when the wrap was at the top (bottom) of the baffle. No significant improvements can be seen between green (no wrap), and red (wrap) lines. But the usage of the wrap did not introduce additional noise unlike in FIG. A where the additional noise was likely due to the absence of ground shield. Also, no significant changes between the left and the right panel.

Apéndice B

Correlated noise detection

In section 4.4.1, 4.4.2 we discussed the basics of Eigen decomposition for getting the dominant noise modes, and the affected ABS data due to these noise modes. We did not use mode removal techniques as the number of affected CES was less than 10 per cent. Here, I will describe the technique of mode removal, and the automatic detection method used to get the affected CES.

B.1. Mode removal

The mode removal can delete the dominant noise mode to recover the underlying cosmological signal. For a particular mode \mathbf{m}_i , the Eigenvector \mathbf{U}_i gives the contribution of each detector to \mathbf{m}_i and hence acts as the weight to reconstruct the mode from linear combination of N detector TOD matrix $D_{N \times N}$. The modes are given by $\mathbf{m}_i = D_{N \times N} \times \mathbf{U}_i$. This is similar to EQ. 4.3 but we include all modes here and ignored the Heaviside function H . Subsequently, the cleaned TOD matrix for a particular mode \mathbf{m}_i is given by $\tilde{D} = D(I - \mathbf{m}'_i \mathbf{m}'_i^T)$ where \mathbf{m}'_i term handles the contribution due to each detector. To remove more than one mode, use the cleaned \tilde{D} from the previous step, and repeat the process. FIG.B.1 shows the knee frequency distribution of the Q (top), and U (bottom) for different detectors from the CES 2148.2 before and after the first three dominant mode removal. Dashed lines represent the median f_{knee} before (red) and after (green) the mode removal. The shift in the f_{knee} towards lower frequencies for the cleaned data represent the removal of dominant correlated $1/f$ noise modes.

B.2. Automatic detection algorithm

As mentioned before, we performed visual inspections to find the CES affected by correlated noise using a subset of 156 CES. But visual inspection of the entire 468 CES from the first season is difficult and an automatic detection algorithm was developed for this purpose.

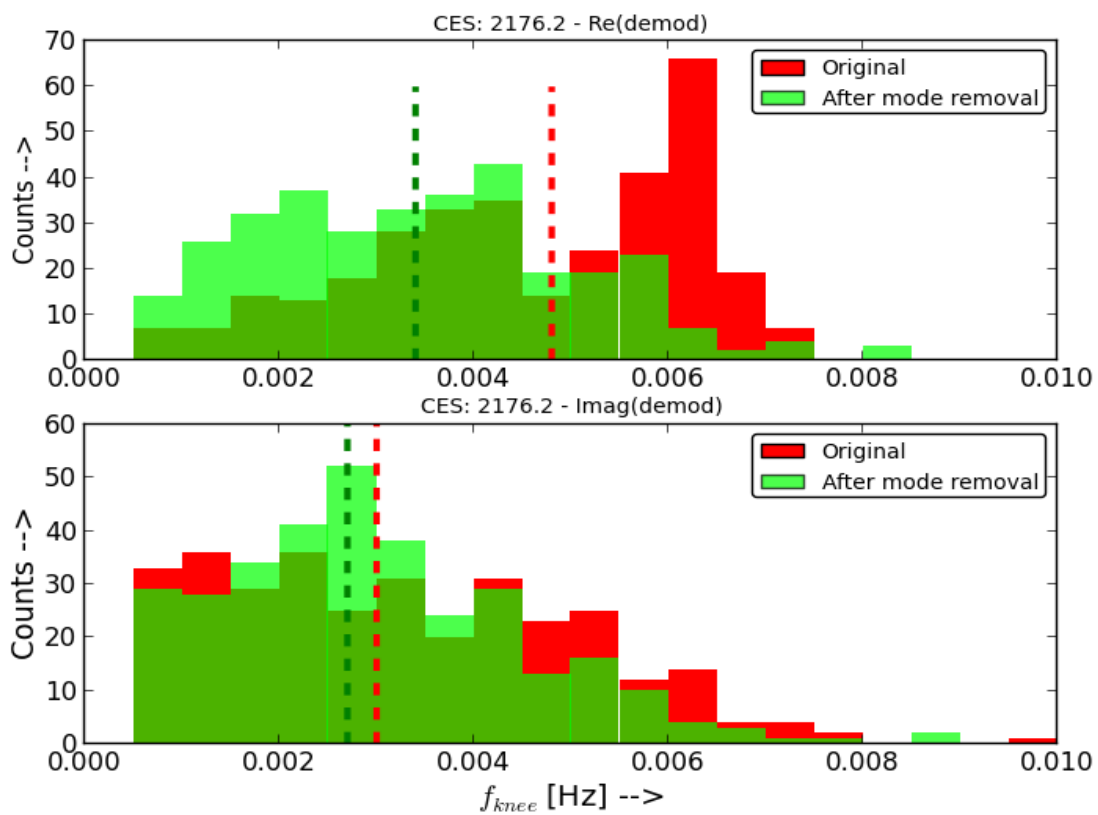


Figura B.1: Distribution of knee frequencies before (red) and after (green) mode removal for the affected CES 2176.2. Top (bottom) panel shows the distribution of f_{knee} of the Q (U) Stokes parameter. Dashed lines show the median f_{knee} .

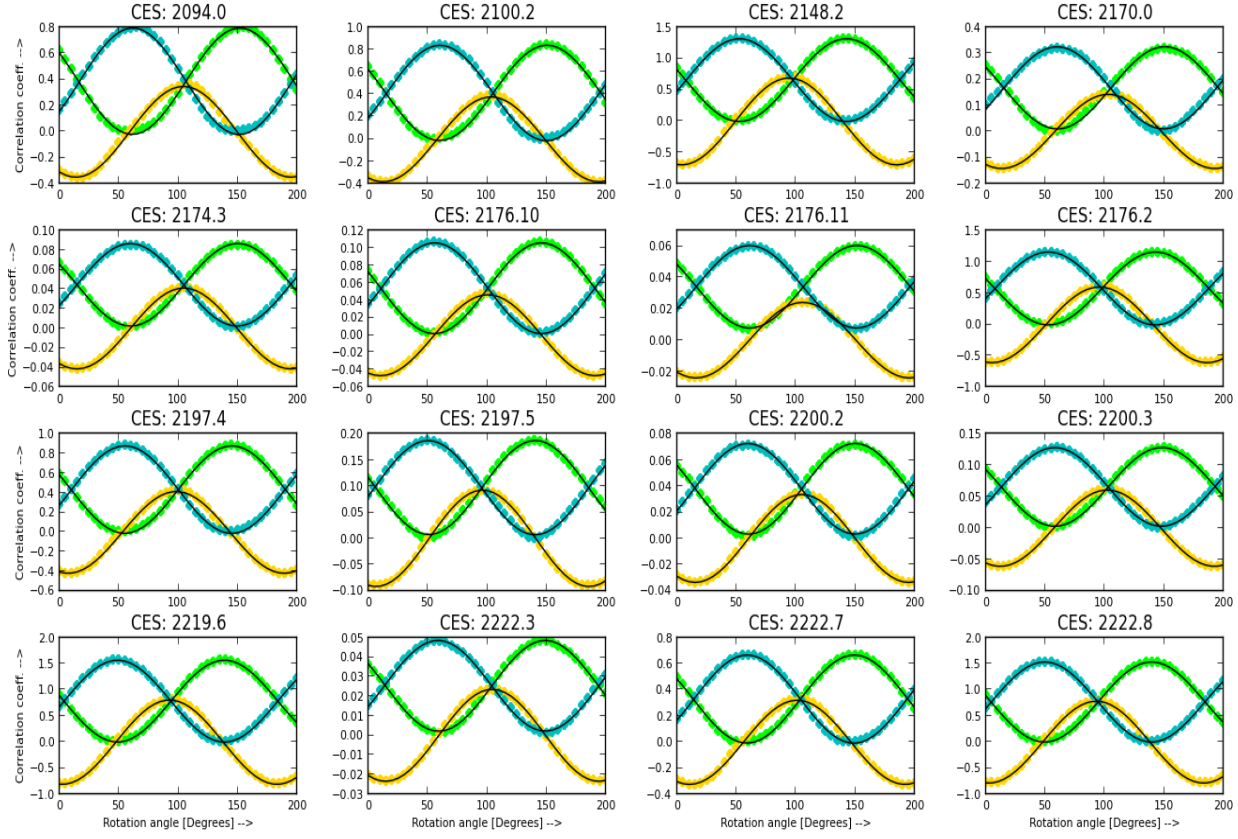


Figura B.2: The median values (vertical axis) of the correlation coefficients for QQ (yellow), QU (green), and UU (cyan) after rotating the correlation matrix by various rotation angles (horizontal axis) of all detectors for 16 randomly picked CES. The black solid curve is the best fit sine curve. At a phase angle of $\sim 49.7^\circ$, the median values of QQ, QU tend towards zero for most of the CES. We picked the respective angle for CES and rotated the UU correlation matrix to use it for the automatic detection algorithm.

This algorithm uses the correlation matrices and bypasses the steps of mode finding, and the visual inspection. The idea is simple. If the CES does not contain the atmospheric 1/f noise then the corresponding correlation matrix showing the correlation between Q, and U Stokes parameters will follow a random Gaussian distribution with zero mean. Hence, we first fit a 1d Gaussian to the distribution of the correlation coefficients between several detectors. The CES is flagged for the 1/f noise if more than 15 per cent of the detectors fall outside the 3σ of the mean value (zero actually) of the Gaussian. Note that we have three correlation values to work with *viz.* QQ, QU, and UU.

However, there must exist a particular rotation which will force all of these distinct information into just one. In other words, there must exist a rotation angle which will bring the correlations of QQ, and QU to zero and we can work with only UU. So we randomly picked 16 CES and performed arbitrary rotations to the QQ, QU, and UU correlation values. The rotated correlation values are shown in FIG. B.2. The yellow, green, and cyan points represents the median correlation coefficients (vertical axis) of the rotated QQ, QU, and UU for various rotation angles θ (horizontal axis). The black solid is the best fit sine curve with

a phase angle of $\sim 49.7^\circ$ (i.e.) When $\theta=49.7^\circ$, the correlation values of QQ , and QU tend to zero. Thus, we now only work with the UU matrix rotated by this special rotation angle and find the CES with more than 15 per cent of the detectors fall outside the 3σ of the mean value (non zero because of the rotation).

The automatic detection algorithm was tested with the same initial subset containing 156 CES. The algorithm picked three additional CES, and missed 1 CES. Upon careful inspection, the three additional CES were indeed affected by $1/f$ noise but were missed by the visual inspection. The CES that was missed by the automatic detection was erroneously flagged earlier visually. We used this algorithm and checked the 453 field-A CES from the first season. Only 33 in 435 CES were affected by the correlated $1/f$ noise. Since this is less than 10 per cent of the observations, we decided to ignore these CES from further analysis instead of removing the noise modes from the affected CES. The f_{knee} distribution of the affected (unaffected) CES are shown in the top (bottom) panel of Fig. 4.13.

B.3. Source of the noise

Finally we looked into the source of this noise in the affected CES by correlating the width of the correlation matrix (one sigma from the Gaussian fitting above) with observation conditions *viz.* PWV, wind, ambient temperature, time of observation, number of passed detectors (to see if the CES only has few passed detectors which could affect the automatic detection algorithm). This is shown in FIG. B.3. There is small correlation with PWV but nothing strong exists with any of the housekeeping information. The solid black line is a first order polynomial with slope m , and intercept n .

We also checked the effect of the scan frequency bump $f_{scan} \sim 0.004$ Hz on the noise. A Lorentzian curve was fit to the f_{scan} bump, and the FIG. B.4 shows the excellent correlation between the width of the Lorentzian and the dominant eigenvalue of the affected (unaffected) CES in red (green) points. The most likely explanation for this correlation is the faster scan speed $v_{scan} \sim 1$ degs $^{-1}$ during the initial observing phase. A nominal speed of 0.75 degs $^{-1}$ was adopted around the middle of the first season. We did not investigate this further as the amount of data lost was extremely small.

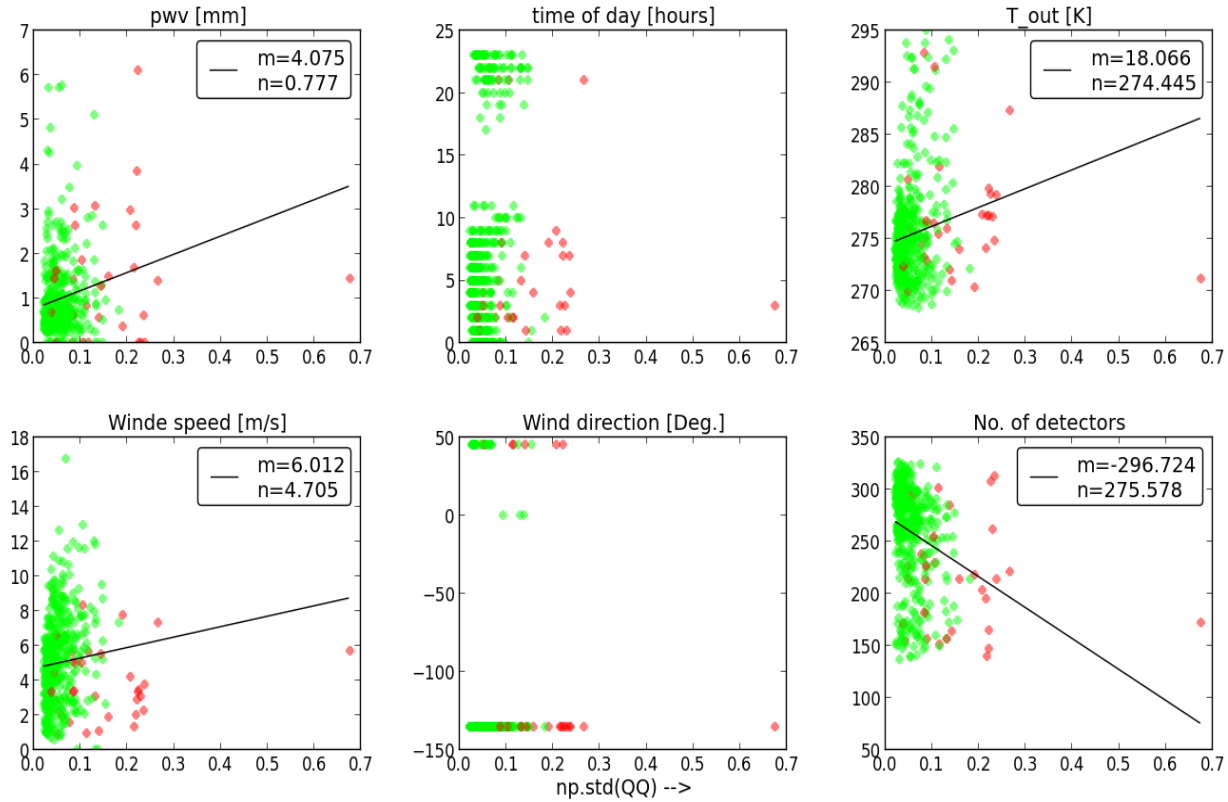


Figura B.3: Correlation between the observing condition (from housekeeping data) and the width of the distribution of the correlation matrices. The red points are bad CES, and green are normal. No unique strong correlation can be seen between the affected CES (red points) and any of the housekeeping data.

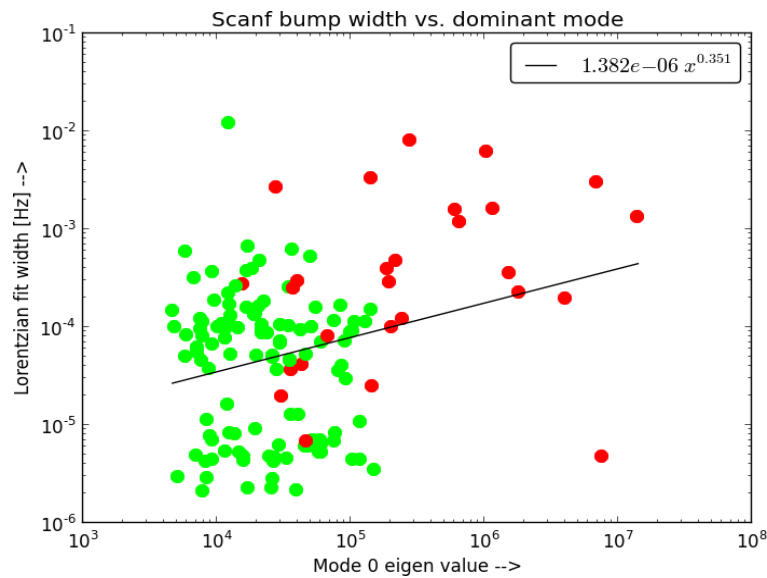


Figura B.4: Correlation between the observing condition (from housekeeping data) and the width of the distribution of the correlation matrices. The red points are bad CES, and green are normal. No unique strong correlation can be seen between the affected CES (red points) and any of the housekeeping data.